



Università degli Studi di Napoli *Federico II*



Università di Camerino



Consiglio Nazionale
delle Ricerche

DOTTORATO DI RICERCA IN QUANTUM TECHNOLOGIES

Ciclo XXXV

Coordinatore: prof. Francesco Tafuri

Molecular Quantum Emitters for Quantum Key Distribution

Settore Scientifico Disciplinare FIS/03

PhD student
Ghulam Murtaza

Tutor
Dr. Costanza Toninelli

Co-Supervisors
Dr. Pietro Lombardi
Dr. Maja Colautti

Anni 2020/2023

I humbly dedicate this thesis to the cherished memory of my late father, *Ghulam Sabir*, a retired teacher, and my beloved mother. Unfortunately, my father passed away just three days before the final submission of this thesis. He played a significant role in shaping my life, not only as a father but also as a teacher. His guidance and wisdom will forever inspire me.....

Acknowledgements

I would like to express my deepest gratitude and appreciation to all those who have supported and contributed to the completion of this PhD thesis. First and foremost, I am immensely grateful to my supervisor Dr. Costanza Toninelli, for their guidance, encouragement, and invaluable insights throughout the entire PhD journey at LENS, Florence. I extend my sincere thanks to my co-supervisors Dr. Pietro Lombardi and Dr. Maja Colautti for their exceptional guidance, mentorship, and unwavering support throughout my PhD journey. I am especially grateful to all of them for their invaluable assistance in understanding the complexities of the experimental set-up. Their expertise in quantum technologies and their patient explanations have been instrumental in bridging the gap between my initial lack of knowledge and my current understanding. I would like to express my sincere gratitude to Prof. Francesco S. Cataliotti, Prof. Alessandro Zavatta, Prof. Michael Hilke, and Dr. David Bacco for their invaluable assistance, particularly during the QKD experiment.

I am thankful to all the other members of the Quantum Nanophotonics group, including Ramin Emadi, Victoria Carrizo, Rocco Duquennoy, Simon, and Juergen. I would also like to thank Ricardo Tani, the LENS Receptionist, as well as Roberto Concas and the other individuals from the Electronics and Mechanical workshops.

I am immensely grateful to my brothers and sisters for their unwavering support throughout my academic journey. Their encouragement and guidance have played a crucial role in my success. Additionally, I would like to extend my gratitude to all of my friends, seniors, and other individuals, such as Tassadaq Nawaz, Rana Babar, Atif Khattak, Asif Ali, Shamaila Manzoor, Maria Maqsood, Fahad Imran, Adnan Rashid, Ali Umair, Rizwan Zahoor, Tariq Khan, Javed Korai, Saqib, Usman Shah, and all of my other Pakistani friends, with whom I had the pleasure of spending quality time during my time in Italy. Furthermore, I would like to thank my Indian friends, Manan Jain, Gunjan Verma, Nihar Ranjan, Depti, Prosenjit and Sathvika.

At the end, I would like to express my gratitude to the University of Naples Federico II and CNR-INO for granting me this valuable opportunity to pursue my Ph.D. I am particularly thankful to the coordinator, Prof. Francesco Tafuri, as well as Guido Celentano, for assisting me with the administrative procedures related to my Ph.D.

Table of contents

List of figures	xi
Nomenclature	xv
Introduction	1
1 Single Photon Sources and quantum emitters	5
1.1 Introduction	5
1.2 The Quantum Nature of Light	6
1.3 Photon Statistics and Key Properties	6
1.4 Single photon generation by isolated quantum emitters	9
1.5 Figures of Merit for Single Photon Sources	11
1.5.1 Purity	11
1.5.2 Quantum Efficiency	13
1.5.3 Brightness	14
1.5.4 Indistinguishability	14
1.6 Quantum emitters in the solid state	15
1.6.1 Color Centres in Diamond	17
1.6.2 Quantum Dots	17
1.6.3 Molecular Emitters	18
1.7 Applications of SPSs	21
2 Quantum Key Distribution	23
2.1 Classical vs Quantum Cryptography	23
2.2 General Concepts	26
2.3 QKD Protocols	27
2.3.1 Discrete Variable QKD (DV-QKD)	27
2.3.2 Continuous Variable QKD(CV-QKD)	27
2.4 BB84	28

2.5	Quantum Hacking	30
2.5.1	PNS Attack on WCP	31
2.6	Decoy State Protocol	32
2.7	Motivations for the Thesis	32
2.8	Formulae Compendium	33
3	Experimental Characterization of Organic Molecule Based SPS	37
3.1	Introduction	37
3.2	Crystal Growth	38
3.2.1	The Fabrication of Anthracene Doped with Controlled Concentration of DBT	38
3.2.2	Sample Preparation and Protection of NC's	39
3.3	Experimental Setup	41
3.4	Optical Characterization at Cryogenic Temperature	43
3.4.1	Hanbury Brown-Twiss (HBT) Configuration	44
3.4.2	Hong-Ou-Mandel experiment	45
3.4.3	Life-time and TPI Visibility Evaluation	48
3.4.4	Temporal and Spatial stability of TPI	50
3.5	Conclusion	52
4	Room Temperature Quantum Key Distribution with molecular emitters	53
4.1	Introduction	53
4.2	Optimization of Sample Fabrication	55
4.3	Test-bed Setup for Room-Temperature QKD	58
4.4	Characterization of Single-Photon Emission at Room Temperature	59
4.5	Result and Analysis	61
4.5.1	Discussion	65
4.5.2	Evaluation of Optimal Molecular Mean Photon Number	66
4.6	Conclusion	69
5	Progress towards Real-time Encoding with room temperature sources	71
5.1	The Polarization Modulator	71
5.2	PM for Real-time State Encoding	73
5.2.1	Different States Encoding using an Arbitrary Waveform Generator (AWG)	74
5.3	Temperature Stabilization for PM	76
5.4	Real-time QKD Experiment	77

5.4.1	Polarization Mode Dispersion	78
5.4.2	QKD with Molecular SPS at cryogenic temperature	79
5.4.3	Probing frequency dispersion in the modulator: different bases for different wavelengths	81
5.4.4	Polarization Mode Dispersion Compensation	81
5.5	Conclusion and Future Challenges	86
6	Conclusions and Future Perspectives	89
	References	91

List of figures

1.1	Photon Statistic	7
1.2	The comparison of antibunched, coherent and bunched light	9
1.3	Two and Three Level System	11
1.4	Fundamental Optical Properties of Photons	12
1.5	Hanbury- Brown-Twiss setup	13
1.6	Hong-Ou-Mandel (HOM)	16
1.7	Quantum Light Sources	16
1.8	Frank Condon Principal and Inhomogeneous broadening	19
2.1	Example of a Public-Key Cryptography	24
2.2	BB84	29
3.1	DBT:AC NCx Preparation by reprecipitation: Complete Process	40
3.2	Sample Preparation	40
3.3	Experimental Setup for DBT:Ac	42
3.4	Purity of DBT under CW Excitation	44
3.5	Pulsed Excitation of DBT	45
3.6	Hong-ou-Mandel experiment under CW Operation	47
3.7	HOM under Pulsed Operation and Excitation Spectroscopy	49
3.8	Experimental investigation of temporal and spatial stability of TPI	51
4.1	Optimization of Sample Fabrication	57
4.2	Optimization of Sample Fabrication	57
4.3	Experimental test-bed for room temperature QKD	60
4.4	Characterization of single-photon emission at RT	62
4.5	Manual States Encoding	63
4.6	Outcome distribution of input states	64
4.7	QKD Channel Characterization	65
4.8	Three Level Model and $g^{(2)}$ at long times	68

4.9	Photon Flux as a Function of the Objective NA	69
5.1	EOSPACE Polarization Modulator	72
5.2	Two Orthogonal States Encoding	74
5.3	Three States Encoding	76
5.4	Setup for real-time polarization encoding	77
5.5	QBER under Pulsed Operation	78
5.6	Polarization Mode Dispersion(PMD) in EOSPACE Modulator	79
5.7	Real-time QKD Experiment with SPS at 3K	80
5.8	DBT Molecule Characterization for Real-time QKD	80
5.9	QBER vs Wavelength	82
5.10	FRM-based PMD Compensation	84
5.11	Sagnac Ring based PMD Compensation	85
5.12	Real-time QKD Experiment with WCP	85
5.13	QBER for Different Sources	86

List of Publications

- Ghulam Murtaza, Maja Colautti, Michael Hilke, Pietro Lombardi, Francesco Cataliotti, Alessandro Zavatta, Davide Bacco, and Costanza Toninelli, "Efficient room-temperature molecular single-photon sources for quantum key distribution", *Optics Express*, 12 2022
- Pietro Lombardi, Maja Colautti, Rocco Duquennoy, Ghulam Murtaza, Prosenjit Majumder, and Costanza Toninelli, "Triggered emission of indistinguishable photons from an organic dye molecule", *Applied Physics Letters* 118, 204002 (2021)
- Colautti, M., Murtaza, G., Hilke, M., Lombardi, P., Cataliotti, F. S., Zavatta, A., ... & Toninelli, C. (2022, July). *Organic Molecules for Quantum Communication*. In *Signal Processing in Photonic Communications* (pp. SpW2J-1). Optica Publishing Group.
- M. Colautti, D. Bacco, Rocco Duquennoy, R. Emadi, P. Majumder, P. Lombardi, G. Murtaza, M. Hilke, F. S. Cataliotti, A. Zavatta, and C. Toninelli. Hong-Ou-Mandel interference from distinct molecules on the same chip. In Philip R. Hemmer and Alan L. Migdall, editors, *Quantum Computing, Communication, and Simulation III*, volume 12446, page 1244611. International Society for Optics and Photonics, SPIE, 2023.
- P. Lombardi, R. Emadi, R. Duquennoy, G. Murtaza, M. Colautti, and C. Toninelli, "Organic Dye Molecules as Single Photon Sources for Optical Quantum Technologies," in *Quantum Information and Measurement VI 2021*, F. Sciarrino, N. Treps, M. Giustina, and C. Silberhorn, eds., OSA Technical Digest (Optica Publishing Group, 2021), paper Tu2B.3.
- Lombardi, Pietro, Maja Colautti, Rocco Duquennoy, Ghulam Murtaza, Prosenjit Majumder, and Costanza Toninelli. 2021. *Indistinguishable Photons from a Single Molecule Under Pulsed Excitation*. Vol. 255. Les Ulis: EDP Sciences. doi:<http://dx.doi.org/10.1051/epjconf/202125506002>.

Nomenclature

Acronyms / Abbreviations

AOM Acousto-optic Modulator

BB84 Bennett and Brassard 1984

BS Beam Splitter

CHSH Clauser-Horne-Shimony-Holt

CV – QKD Continuous Variable Quantum Key Distribution

CW Continuous Wave

DBT Anthracene

DBT Dbenzoterrylene

DOF Degree of Freedom

DV – QKD Discrete Variable Quantum Key Distribution

EMCCD Electron Multiplying Charge-Coupled Device

EOM Electro-Optic Modulator

FPC Fiber Polarization Controller

FRM Faraday Rotator Mirror

FWHM Full Width Half Maximum

hBN Hexagonal Boron Nitride

HBT Hanbury Brown and Twiss

<i>HOM</i>	Hong-Ou-Mandel
<i>HWP</i>	Half Wave Plate
<i>LiNbO₃</i>	Lithium Niobate
<i>MUBs</i>	Mutually Unbiased Bases
<i>MZI</i>	Mach-Zehnder interferometer
<i>NCx</i>	NanoCrystals
<i>PAH</i>	Polyaromatic hydrocarbons
<i>PDL</i>	Polarization Dependent Loss
<i>PID – SA</i>	Proportional Integral Derivative -Servo Amplifier
<i>PM</i>	Polarization Modulator
<i>PMS</i>	Polarization Mode Dispersion
<i>PNS</i>	Photon Number Splitting
<i>PSB</i>	Phonon Sideband
<i>PVA</i>	Polyvinyl Alcohol
<i>QBER</i>	Quantum Bit Error Rate
<i>QDs</i>	Quantum Dots
<i>QKD</i>	Quantum Key Distribution
<i>QWP</i>	Quarter Wave Plate
<i>QY</i>	Quantum Yield
<i>RSA</i>	Rivest–Shamir–Adleman
<i>SKR</i>	Secret Key Rate
<i>SKR</i>	Secret Key Rate
<i>SPAD</i>	Single-Photon Avalanche Diode
<i>SPCM</i>	Single Photon Counting Modules

SPS Single Photon Source

TCSPC Time- Correlated Single Photon Counting

TPI Two-Photon Interference

WCP Weak Coherent Pulse

ZPL Zero-Phonon Line

Introduction

Cryptography, which comes from the Greek words *kryptós* (hidden) and *graphein* (to write), has been used for as long as writing has existed. Cryptography is the practice and study of techniques to achieve secure communication in the presence of adversarial behavior. The history of cryptography spans over thousands of years and can be traced back to ancient civilizations such as the Old Kingdom of Egypt and Mesopotamia, where they used hieroglyphs and clay tablets to protect sensitive information[1, 2]. However, based on resources and technological advancements, encryption quality likewise increased as civilization advanced. The Greeks and Romans also made significant contributions to the field of cryptography with the invention of polybius table[3] and Caesar Cipher[4], where each letter of the original message was replaced by a different letter by shifting the original letter left or right with a fixed position. In the Caesar Cipher encrypted message was written in Latin using the Greek alphabet, since none of the adversaries knew the Greek alphabets[5, 6]. The Alberti disk, the first polyalphabetic cipher, was created in 1467 by Leon Battista Alberti[6] and his idea offered concept of mechanical ciphering algorithms. In the late 19th century, electricity was introduced which led to the development of electromechanical ciphering systems such as Vernam cipher[7]. In Vernam cipher each character of the plaintext message is combined with the corresponding character of the one-time pad to produce the ciphertext message and the key is never reused. The advancements in the electromechanical system further progressed in the invention of the Enigma rotor machine[8] in the late 1930s, which offered more efficient encryption techniques. This Enigma machine was a combination of mechanical and electrical systems. Keyboard and rotors were linked and different speed of rotors was used to create cipher text. Both rotor machines and digital computers were used to produce electronic encryption[9] after the invention of the digital computer and crypto algorithm were considered as a new cryptographic standard. In 1978, the Rivest–Shamir–Adleman (RSA) protocol[10], an asymmetric method for encryption was introduced, whose security is based on the assumption that factoring large integers is a computationally intractable problem. In fact, no classical computer can perform this task in a polynomial time. However, as conventional security methods still depend on the

computational complexity of certain tasks, they may become vulnerable to unanticipated advancements in hardware and software. This risk is today assuming a gigantic impact, as everyday 2.5 quintillion bytes data are generated and exchanged, a number which is escalating rapidly [11]. In particular, also critical infrastructures can be sabotaged through a cyber warfare.

Quantum computing, envisaged by Richard Feynman in 1979[12, 13] and now showing evidence in the first relatively small prototypes (e.g. Sycamore quantum processor by Google[14, 15] and Eagle quantum processor by IBM[16]), is a disruptive hardware advancement that threatens current security methods, such as those based on the RSA protocols. Indeed quantum computers can theoretically outperform any classical device in specific tasks, such as the Shor's factoring Algorithm[17]. Due to these vulnerabilities, alternative methods for data encryption must be explored rather than relying solely on computational complexity. Quantum cryptography is a field of research that aims to provide security guarantees that cannot be reached by classical means[18], based on the laws of quantum mechanics. It relies on the use of quantum states of light, such as single photons, to encode and transmit information in a way that is immune to eavesdropping or decryption by an adversary with unlimited computational power[19]. It is worth noticing that we are talking about a paradigmatic shift in the way we will communicate in the future in terms of the physics law underpinning security. Nevertheless, the use of light as information carrier is already a reality with a world-wide network of more than 28000 kilometers of optical fibers.

One of the most widely used quantum cryptographic protocols is quantum key distribution (QKD), which allows two parties to establish a secret key by exchanging quantum states over a public channel[20]. The security of QKD relies on the fact that any attempt to measure or copy the quantum states will introduce errors that can be detected by the parties. However, QKD also requires that the source of quantum states emits only one photon per pulse, otherwise an eavesdropper could split the pulse and gain information without being noticed[21]. Therefore, QKD needs a photon turnstile, a device that can produce single photons on demand[22] with high probability and low multi-photon probability[23, 24]. Single-photon sources (SPSs) will hence play a critical role in the advancement of quantum technologies such as quantum computing[25, 26] and communication[27, 28].

The ideal SPS should emit photons in single-photon Fock states, which implies a vanishing multi-photon probability per trigger pulse. Additionally, it should have high brightness, allowing for the collection of a single photon on-demand. For certain QKD protocols, in order to undergo two-photon interference - an exquisitely quantum effect- the emitted photons should be indistinguishable[29]. Finally, the technology of single photon generation

should be ideally scalable and provide many single photons in a well-defined mode of the electromagnetic field for further manipulation.

Most previous quantum key distribution (QKD) experiments have used probabilistic sources based on spontaneous parametric down-conversion [30, 31] or attenuated laser sources [32–34], whereby the compromise between efficiency and multi-photon probability (enabling an eavesdropper to obtain information [23, 24]) is determined by a poissonian statistics. More advanced protocols have been demonstrated taming photon-number splitting attacks [35]. However, probabilistic sources suffer from a limited scalability, as the coincidence probability in experiments with many single photons vanishes rapidly [36]. An alternative approach is to develop deterministic single photon sources based on the radiation of single quantum emitters. They might offer better security, mimicking the ideal single photon turnstile since they can emit a single photon per triggered laser excitation [37, 38]. This theoretical concept is in practice challenged by experimental imperfections in the generation process, as we will discuss thoroughly throughout the manuscript. Interestingly, we are currently close to the turning point of outperforming the secret key length achievable with attenuated laser pulses, using instead a single quantum emitter as the single photon source [39, 40]. Similar findings will potentially facilitate secret key distribution in high channel loss scenarios, such as satellite-based QKD.

Various emitters, such as quantum dots [41–51], excitons in transition metal dichalcogenides (TMDCs) [52], color centers in diamond [53] and hexagonal boron nitride (hBN) [54, 55], have been used for QKD.

The need for specialized equipment and infrastructure to achieve low temperatures is a major hurdle for the widespread deployment of quantum emitters in QKD systems. The development of room temperature approaches hence potentially allows for a technological breakthrough in the field. These advantages are particularly important for quantum satellite communications.

In this thesis we explore single molecules as quantum emitters for QKD applications. In particular, dbenzoterrylene (DBT) molecules, embedded in suitable host matrices, are excellent quantum light sources [56–59, 31], with Fourier-limited linewidth at cryogenic temperature, high photostability and low spectral diffusion also when embedded in a nanocrystalline environment [60]. Moreover, unlike previous example, DBT emits bright single photons also at room temperature with high purity and long-term photo stability [61]. We hence characterize this emitter under pulsed excitation, suitable for QKD applications, in terms of its purity, brightness and indistinguishability. We also present first experiments about room temperature QKD with molecular quantum emitters, all the way from the manual to the real state preparation.

The thesis manuscript is organized as follows:

Chapter 1 presents a theoretical foundation for motivating and understanding the experiments on quantum light sources described in this thesis. An overview of different flavours of light and the figures of merit of the SPSs are also highlighted. The available SPSs with greater emphasis on molecular quantum emitter is also described.

Chapter 2 gives a general introduction to classical and quantum cryptography. The theoretical framework of QKD along with security protocols, hacking strategies, evaluation of SKR and QBER and finally motivations behind this thesis are outlined.

Chapter 3 introduces organic dye molecules as SPSs and their photophysical properties at cryogenic and room temperature. The home-built experimental setup for single molecule microscopy at cryogenic temperature is presented. This was the first experiment I contributed under supervision of my supervisor and co-supervisors. The complete characterization of single DBT molecules in bulk Ac crystals is elaborated which makes this molecular system a reliable source of single photons. This work is published in Applied Physics Letters[58].

Chapter 4 provides insight of the experiment of QKD using molecular quantum emitter at room temperature. This experiment was the goal of my PhD. I performed the experiment under guidance of supervisor and co-supervisors. Prof. A. Zavatta (CNR-INO), Prof. M. Hilke (McGill University) and David Bacco (DTU) also helped in the experiment. In this experiment, the manual strategy for different states encoding and comparison with other state of the art QKD experiments in terms of SKR and QBER using other state of the art SPSs is described. The findings of this work have been published in Optics Express[40].

Chapter 5 reports real-time state preparation using electro-optic modulator for free space quantum communication. Different compensation techniques for PMD, laser power stabilization and temperature control for the modulator are also highlighted. Additionally, the techniques for encoding two and three distinct states using the EOM with an arbitrary waveform generator for both WCP and SPS.

Chapter 1

Single Photon Sources and quantum emitters

This chapter outlines the basic concepts that constitute the theoretical framework around the experiments presented in Chapters 3 and 4. In particular the fundamental quantum nature of light is briefly discussed, as well as the generation of single photon wavepackets by means of quantum emitters. Afterwards, the most prominent figures of merit characterizing single photon sources are presented. In the last part, various types of quantum emitters, including quantum dots, color centres in diamond and molecules are introduced, along with their specific features and some potential applications in quantum technologies.

1.1 Introduction

In the last two decades quantum technologies observed an extraordinary advancement, exploiting exquisitely quantum features of increasing complexity e.g. in quantum information science[62, 38], quantum communication[41, 63, 64], quantum sensing[65–67] and quantum computing[68–70]. The disruptive impact of these technologies in a wide range of disciplines brought the name of a “Second Quantum Revolution”[71, 72]. Whether a specific application falls under the definition of second quantum revolution is sometimes a reason of debate, the generation, the manipulation and detection of single photons is by no doubt a fundamental resource towards the demonstration of a quantum advantage. Photons, often employed as "flying qubits"[64], are indeed the main ingredient of quantum communication technologies. In this chapter, an introduction to quantum emitter-based single-photon sources, their state of the art, the desired properties and their applications are presented.

1.2 The Quantum Nature of Light

Photon is an ancient Greek word meaning light: *phōtós*. It's the fundamental quantum unit of electromagnetic radiations. The quantization of electromagnetic energy was first introduced by Max Planck in 1900 as a mathematical "trick" able to explain the spectral properties of a black body radiation[73]. He observed theoretically that the black body behaviour can be reproduced by a model in which absorption and emission of energy occur in discrete manner, through a set of equal and definite parts. These are called energy elements, and their energy content is proportional to their frequency ν through the Planck constant h (i.e. $E = h\nu$). In 1905, Einstein came up with theory of photoelectric effect[74] leveraging Planck's model and later on he proposed wave-particle duality. In 1922, Arthur Holly Compton observed wavelength shifting of scattered x-rays and lead to discovery of the Compton effect[75] confirming the effectiveness of the representation. The term "photon" was coined by Gilbert Lewis in 1925 [76]. Paul Dirac finally performed the formal quantization of the electromagnetic field in 1927[77].

The quantum nature of light is hence intimately connected to the introduction of the concept of photons.

1.3 Photon Statistics and Key Properties

Just as an operative definition, we will associate photons to detectors' clicks. Technically speaking, in the case of single photons, they can be detected e.g. by single photon avalanche photodiodes operating in Geiger mode. In such devices, the counter-polarizing field at the junction is strong enough to saturate the cascade of electrons even in the case it is generated by the absorption of a single photon, i.e. the formation of a single electron-hole pair.

Indeed, in the Geiger mode, the detector operates in a binary on/off state, where a photon detection results in a strong electrical pulse, while no pulse is observed if no photon is detected, allowing for high detection efficiency and fast counting rates. Each photon produces a single click with very high temporal definition, but with the drawback that amplitude of the signal (photon number) cannot be discriminated. One can then imagine an experiment in which clicks are recorded as a function of time. The number of clicks in a given time bin can then be considered as a statistical ensemble, in order to estimate their average value (proportional to the light field intensity) and also the relative fluctuations. The statistical distribution of photons emitted from different light sources can be classified into three possible cases depending on the variance $(\Delta n)^2$ and average photon number \bar{n} , as shown in

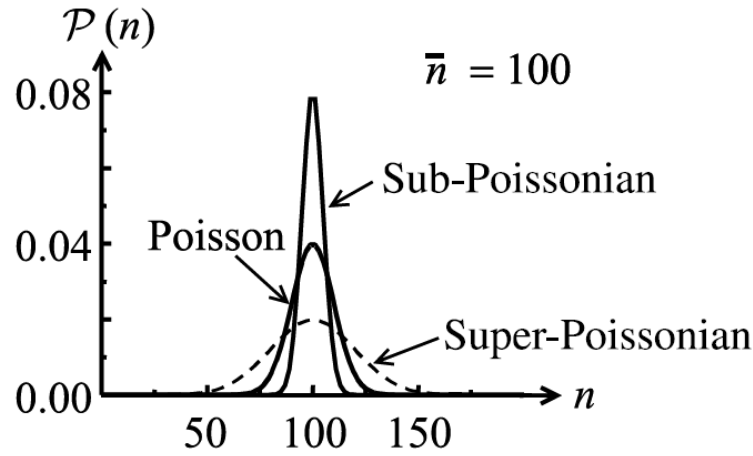


Fig. 1.1 Photon Statistical Distribution: In the Poissonian distribution, photons arrive at random moments in time associated to independent events, resulting in a distribution whose variance is equal to the average number of photons. The super-Poissonian distribution occurs when photons are strongly correlated and arrive in bunches, resulting in a distribution that has a higher variance than the Poisson distribution. In contrast, the sub-Poissonian distribution corresponds effectively to an anti-correlation, resulting in a distribution that has a lower variance than for the Poisson case.

Fig 1.1, where different distributions are compared for the same average photon number $\bar{n} = 100$.

A classic electric field with constant amplitude will result for instance in a **Poissonian distribution**. In this case, the distribution shows a variance $(\Delta n)^2$ equal to the mean value \bar{n} . Considering photon number n in a light pulse, the probability for having n -photon pulse is given by:

$$P(n) = \frac{\bar{n}^n}{n!} e^{-\bar{n}}, \quad n = 1, 2, 3, \dots \quad (1.1)$$

This type of photon statistics generally applies to random processes. This is for instance the case of the coherent state produced by a laser.

Super-Poissonian light sources have large fluctuations in the photon number as compared to coherent light with constant intensity. An example of a Super-Poissonian probability distribution is given by:

$$P(n) = \frac{1}{1 + \bar{n}} \left(\frac{\bar{n}}{\bar{n} + 1} \right)^n \quad (1.2)$$

This corresponds exactly to Boltzmann distribution expressed in terms of the average photon number. It hence represents the characteristic distribution of thermal light sources. These exhibit a varying intensity and $(\Delta n)^2 > \bar{n}$

Sub-Poissonian light sources shows instead smaller intensity fluctuations than the poissonian ones, with $(\Delta n)^2 < \bar{n}$. Sub-Poissonian light sources do not have a classical counterpart and are much more stable than coherent light sources.

Now the question arises about how such different flavours of light can be detected experimentally, giving the typical dead times of our detectors and their not-unitary efficiency. The information on the intensity fluctuations is actually contained in the field second order autocorrelation function $g^{(2)}$ that is defined as follows:

$$g^{(2)}(\tau) = \frac{\langle I(t+\tau)I(t) \rangle}{\langle I(t) \rangle^2} \quad (1.3)$$

The quantum version of the equation for $g^{(2)}$ is used to measure the correlation between the intensity of light at different points in time. It is given by[38]:

$$g^{(2)}(\tau) = \frac{\langle a^\dagger(t)a^\dagger(t+\tau)a(t+\tau)a(t) \rangle}{\langle a^\dagger(t)a(t) \rangle^2} \quad (1.4)$$

where $a(t)$ is the annihilation operator at time t , $a^\dagger(t)$ is the creation operator at time t , and τ represents the time delay between the two measurements. The brackets $\langle \rangle$ indicate an average over time. This equation allows us to quantify the second-order coherence of a quantum system, providing insights into the nature of photon statistics and the presence of photon correlations. The $g^{(2)}$ function is typically measured in the so-called Hanbury-Brown-Twiss configuration [78], whereby the stream of photons is splitted in two arms by means of a 50/50 beam splitter (see Fig. 1.5). Each output port is then terminated by a single photon detector, that allows the collection of clicks $n_3(t)$ and $n_4(t)$ as a function of time. The histogram of coincidences approximates well the second order autocorrelation function for short delays[38]. According to this description, we can rewrite Eq. 1.3 as follows:

$$g^{(2)}(\tau) = \frac{\langle n_3(t)n_4(t+\tau) \rangle}{\langle n_3(t) \rangle \langle n_4(t+\tau) \rangle} \quad (1.5)$$

In terms of the second order auto-correlation function, we can then classify light sources into the following three categories according to the behaviour of this function around zero delay $g^{(2)}(\tau = 0)$. A pictorial representation is shown in the Fig. 1.2.

- **Bunching:** $g^{(2)}(0) > 1$
This corresponds to a higher probability of finding two photons arriving simultaneously and hence to the occurrence of photons in bunches (i.e. super-Poissonian distribution).
- **Coherent Light:** $g^{(2)}(0) = 1$
This corresponds to a flat $g^{(2)}(\tau)$ with same value at each delay and in particular $g^{(2)}(0) = g^{(2)}(\tau) = 1$ (Poissonian distribution).
- **Antibunching:** $g^{(2)}(0) < 1$ characterized by autocorrelations at zero time delay (sub-Poissonian distribution).

Interestingly in the case of photon number states, it turns out that:

$$g^{(2)}(0) = 1 - \frac{1}{\langle n \rangle} \quad (1.6)$$

and hence in particular that $g^{(2)}(0) = 0$ for a single photon Fock state.

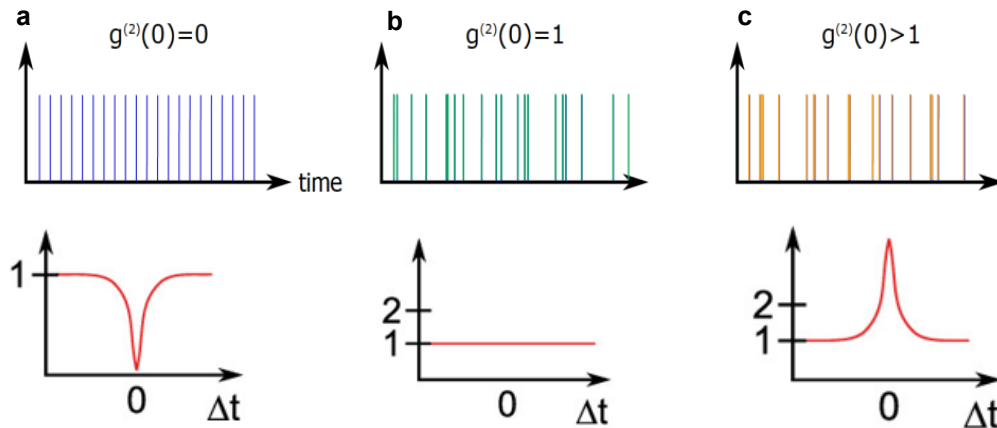


Fig. 1.2 The comparison of antibunched (column a), coherent (column b) and bunched light (column c): **Top row:** Photon detection events resulting in detector spikes of a constant intensity as a function of time. **Bottom row:** Corresponding intensity correlation function yielding $g^{(2)}(0) = 0$, $g^{(2)}(0) = 1$ and $g^{(2)}(0)$ is greater than 1, respectively.

1.4 Single photon generation by isolated quantum emitters

It is clear from the previous section that an ideal single-photon source that contains one and only one photon per pulse cannot be provided by an attenuated laser, as the probability of

having 0 or 1 click are strictly related by poissonian statistics. Although heralded single photon sources from parametric down conversion have been the work horse of quantum optics for long time[79], their probabilistic nature has important limitation. Alternatively, single photons can be obtained in the spontaneous emission of isolated quantum emitters upon trigger laser excitation [80]. The aftermath of a spontaneous emission event from a single atom leaves the light field in a quantum state that can be almost considered one of the potential definitions of a single photon, albeit existing in a superposition of modes[81].

With quantum emitters (QEs) we dub a variety of systems possessing a strong radiative transition that couples two electronic energy levels. In general, QEs in the solid state present complex energy level schemes, including vibrationally excited states and dark states. Moreover, their coupling with the host matrices in the solid state brings about other possible decay channels and dephasing processes further discussed in in Section 1.6.3 and in the Chapter 3.

In most experimental cases, the QE can be described by a two level system (TLS), as it is probed by a monochromatic laser source resonant with the optical transition. Here, any deviation from the isolated two-level system is considered detrimental.

Quantum dots [82][83], single atoms[84], color centres in diamond [85][86] and single molecules [87][88][58] are all system which can be modelled by the TLS model. The relevant light-matter interaction processes for a TLS are sketched in Fig. 1.3a): an external laser resonant with the TLS transition is employed to excite the system in the first step. A single photon is emitted upon system relaxation to the ground state. This process is called spontaneous emission and the energy of the emitted photons will be given by:

$$E = h\nu = \frac{h}{2\pi} \omega_0 \quad (1.7)$$

where h is Planck's constant ($6.626 \times 10^{-34} Js$) and $\hbar\omega_0$ is the energy difference between the ground $|1\rangle$ and the excited state $|2\rangle$. In panel b) the likely presence of a third dark state is shown, with K_{ij} indicating the coupling rates. The effect of such dark states on the efficiency of quantum-emitter based SPSs is discussed in more details for the case of the investigated molecular emitter in Chapter 4.

Finally, in the case of "off-resonant" pumping we can effectively use another intermediate level that decays so rapidly to the second one that it is never effectively populated. This configuration is used extensively in this thesis work, as it allows for an efficient pumping of the excited state.

This simple picture neglects the effects of the induced coherence and is hence valid only when their decay is much faster than the other decay rates. This is typically the case for

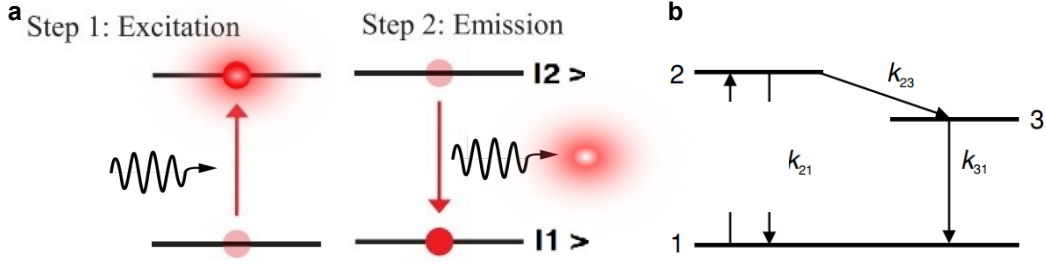


Fig. 1.3 Two and Three Level System: **a)** The two energy levels of a TLS, separated by energy $\hbar\omega_0$ are coupled by the resonant electromagnetic field. Two processes are highlighted. In the first picture, the system, initially in its ground state, is excited to a higher energy state. After a certain aleatory time, driven by the emission probability k_{21} , the system emits a photon and returns to its ground state. Equivalently the emitted photon wavepacket has a characteristic decay time $\tau = k_{21}$. The arrows indicate the transition between the two states. **b)** Transitions to triplet or dark states are accommodated by taking in consideration a third metastable level, i.e. a state with much lower emission probability $k_{31} \ll k_{21}$.

quantum emitters at room temperature. It also captures the steady state situation for resonant pumping well below saturation and for off-resonant pumping. The full system of optical Bloch equations are needed for a more complete treatment, that falls beyond the scope of this thesis where we mostly discuss the manipulation of the emitted photons.

1.5 Figures of Merit for Single Photon Sources

In this section we identify some important parameters that quantify the performance of single photon sources, allowing for benchmarking and comparisons among different platforms. There are several specific requirements that must be met for the light emitted by a source to be useful in quantum information, computation, or cryptography applications[51] and these properties are sketched in the Fig. 1.4. We also discuss the main experimental tools to estimate them.

1.5.1 Purity

The purity of a SPS refers to the probability of emitting only one photon per pulse p_1 , with respect to the probability of having higher photon number states p_n . It hence corresponds to the formula:

$$P = \frac{p_1}{\sum_n p_n} \quad (1.8)$$



Fig. 1.4 Fundamental Optical Properties of Photons: **a)** An optimal source of single, identical photons produces a continuous stream with each excitation laser pulse. **b)** Example of sources having a brightness less than one, as photon emission only occurs during certain laser pulses. **c)** If there are two photons present then this case represents single-photon purity lower than one. **d)** The loss of photon coherence is schematized by broken lines. **e)** Imperfect indistinguishability can arise due to phase variations or spectral wandering, causing changes in the photon wave packet. (Reprinted by permission from Springer Nature: Simone Luca Portalupi and Peter Michler. "Quantum Dots for Quantum Information Technologies"[51])

The purity can be estimated from the second-order autocorrelation function $g^{(2)}(\tau)$, that was already defined in eq. 1.3. Indeed, it can be demonstrated that, when p_n for $n > 2$ is negligible with respect to $p_{1,2}$ and $p_2 \ll p_1$, the purity can be directly linked via Taylor expansion to the second order autocorrelation function through the relation:

$$P = 1 - \frac{1}{2}g^{(2)}(0) \quad (1.9)$$

Therefore, for a pure SPS, $P = 1$ and $g^{(2)}(\tau)$ should be equal to zero at zero time delay ($\tau = 0$), which means that there is no probability of detecting two photons simultaneously. Experimentally, from an HBT setup such as the one sketched in Fig.1.5, a histogram can be built with a Time-Correlated Single Photon Counting (TCSPC) module, that uses the photon arrival times on the two detectors as the start and the stop signal for a time to amplitude converter. This correctly approximates the actual $g^{(2)}$ for times shorter than the inverse of the average detected rate.

For light emitted by an ideal two-level system, the result of the Hanbury-Brown-Twiss experiment outlined above yields a function $g_{HBT}^{(2)}(\Delta t) = 1 - b \times e^{(-|\Delta t|/\tau_{HBT})}$, with $1/\tau_{HBT} = K_{12} + K_{21}$, determined by the pumping and the decay rates K_{12}, K_{21} , respectively, (see also section 3.4.1) and Ref.[80].

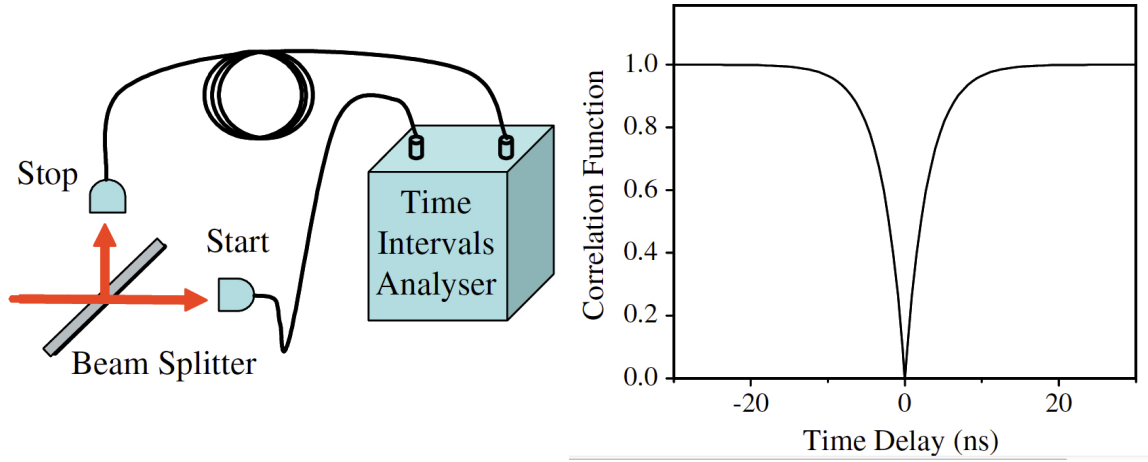


Fig. 1.5 On the left, concept for an autocorrelation function measurement with an Hanbury-Brown-Twiss setup. On the right, the expected result for the $g^{(2)}(\tau)$ for a perfect single-photon source. The figure has been adapted from Ref.[80]

1.5.2 Quantum Efficiency

The quantum efficiency of the TLS transition refers to the probability that the state decays radiatively with respect to all other dissipative mechanisms. It is hence also a measure of how effectively the SPS produces single photons. The quantum efficiency or quantum yield (QY)¹ is given by the ratio between the radiative decay rate (k_r) and the total decay rate.

$$QY = \frac{k_r}{k_r + k_{nr}} \quad (1.10)$$

where k_{nr} is the non radiative decay component of the total rate. The QY of a SPS should ideally be equal to 1, indicating that every excitation results in the emission of a single photon. However, in reality, internal non-radiative transitions occur within the SPS, leading to a temporary loss of fluorescence (see Section 4.5.2), commonly known as blinking. Also internal conversion from excited vibrational levels to the emitting state can dissipate energy

¹In general with QY one indicates the probability of obtaining a photo per excitation so it is a more general concept. However, also based on the discussion in Ref. [89] we here use quantum efficiency and yield equivalently.

[90]. As a result, the QY of the SPS is reduced. In order to estimate the effect of blinking, a possible method is to look for bunches at long times in the $g^{(2)}(\tau)$ function (see Fig. 4.8). This was done for instance in this thesis for the estimation of the molecules' OFF times at room temperature in Chapter 4. Alternatively the QY can be also estimated by monitoring the local density of states effects on the emitter lifetime[91] or by comparing the detected and expected photon rates, after careful and independent calibration of the setup losses.

1.5.3 Brightness

The probability of having one click per trigger pulse is often named brightness. In CW excitation instead, the achievable rate depends on the excited state lifetime τ and on the QY. The emission rate can be expressed by:

$$R(I) = \frac{1}{\tau} \rho_{ee}(I) QY \quad (1.11)$$

where ρ_{ee} is the population of the excited state in the density matrix description and I , the intensity of the pump laser. As an example, one can consider the stationary state solution of the rate equation for the two level system and obtain

$$R(I) = R_{\infty} \left(\frac{1}{1 + I_s/I} \right) \quad (1.12)$$

where I_s is the saturation intensity. As the intensity I increases, the emission rate increases linearly until the population saturates to a stable state in which emission exactly compensates absorption, $\rho_{ee} = \rho_{gg} = 1/2$, and the emitted photon rate reaches a maximum value R_{∞} , given by $R_{\infty} = \frac{1}{2\tau}$. In case of off-resonant excitation, e.g. via the excitation of a vibrational level of the electronic excited state, a complete population inversion is accessible and consequently $R_{\infty} = \frac{1}{\tau}$ [92].

1.5.4 Indistinguishability

The intensity correlation function only gives information about the purity of the photon stream. Another fundamental property required in many protocols is indistinguishability between the emitted photons[93]. This corresponds to the extent of the wave packets' overlap, i.e. emission should occur always in a given and pure quantum state. Based on this property is the ability of photons to undergo a two-photon interference process[62, 94], whose visibility will be connected to the first order coherence of light and in particular to $|g^{(1)}(0)|^2$ (see Chapter 3.4.2)[95]. Two-photon interference has no classical analogue and was first demonstrated

in 1987 by the three scientist Chung Ki Hong, Zheyu Ou, and Leonard Mandel[96], after whom today this experiment is named. The basic setup for a Hong-Ou-Mandel (HOM) experiment is sketched in Fig. 1.6, where two-photon interference is measured from the emission of a single quantum emitter. This scheme has been extensively employed in color centres in diamond[97], quantum dots[62] and organic molecules [98, 56, 57]. It is based on a first beam splitter that allows simulating two independent sources, provided the delay line on one arm is long enough to loose memory of the temporal correlations between the two lines. When the photons are indistinguishable, destructive interference occurs among the probability amplitude of the processes corresponding to both photons being transmitted and reflected. This manifests itself in a reduced probability of coincidence detection at the two output ports. The HOM interference visibility (V_{HOM}) can be calculated by eq. 3.4 , where respective $g_{\perp}^{(2)}(0)$ and $g_{\parallel}(0)$ correspond to the indistinguishable case (parallel polarization) and distinguishable case (orthogonal) coincidence counts obtained by measuring the intensity correlation in the HOM setup.

$$\left|g^{(1)}(0)\right|^2 = \frac{g_{\perp}^{(2)}(0) - g_{\parallel}^{(2)}(0)}{g_{\perp}^{(2)}(0)} \quad (1.13)$$

Moreover the HOM interferometer is a simple tool for entanglement generation: indeed the output of the operation is a path-entangled two-photon state, belonging to the NOON-state family (with $N=2$). Entangled states are main elements in quantum information for long-haul quantum communication and quantum computing.

The main reasons for a non-unitary visibility in the HOM experiments with quantum emitters are the decoherence processes that broadens the emission line, the residual detection of photons in other spectral lines beyond the two levels of the ideal TLS, the presence of spectral diffusion and the residual multiphoton probability. All these factors will be further discussed in Chapter 3, with respect to the molecular source in exam.

1.6 Quantum emitters in the solid state

The most promising systems for achieving single photons on demand are SPSs based on quantum emitters. Among these emitters, color centers in diamond[85, 99], quantum dots[100–102], and molecular sources[37, 103] stand out as highly effective options and are hence presented here (see Fig. 1.7).

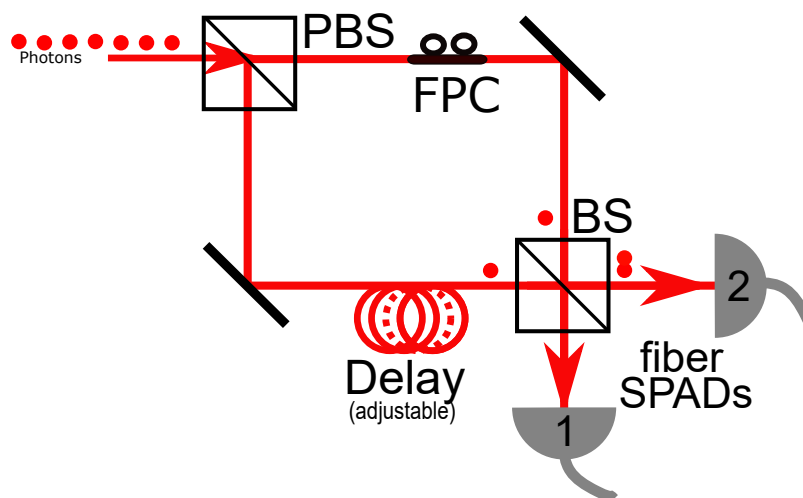


Fig. 1.6 Setup to measure Hong-Ou-Mandel effect: a first beam splitter is used to mimic the presence of two sources; an unbalance delay guarantees the two photon stream are uncorrelated (provided that the difference is longer than the single-photon wavepacket); then two indistinguishable photons are injected at the two input ports of the second beam splitter and their interference is measured at the output ports as a suppression of the coincidences.

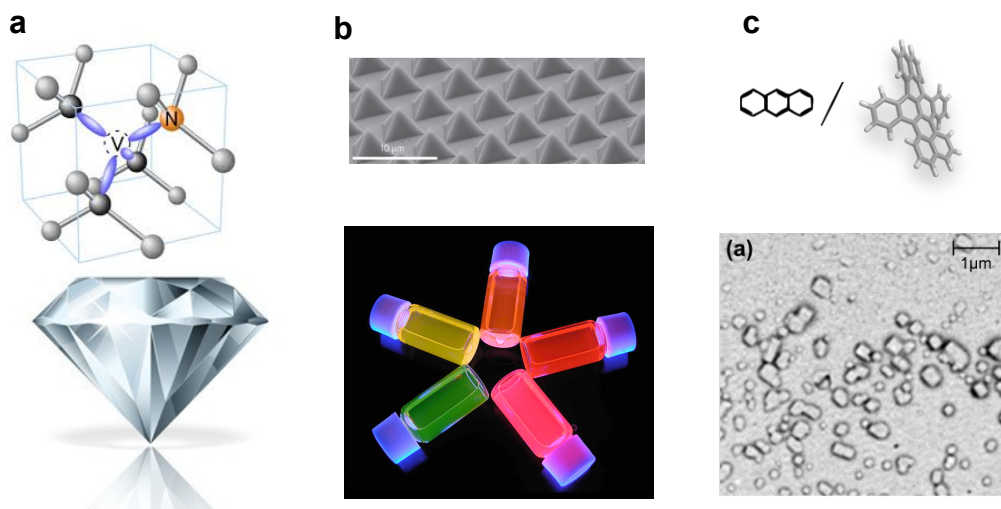


Fig. 1.7 Quantum Light Sources: **a)** Color Centers in Diamond, based for instance on nitrogen or silicon defects, which have been shown to have long spin coherence times and high photon emission rates (adapted from Ref. [104]). **b)** Quantum Dots: on the top is an SEM image of a matrix of InGaAs pyramidal quantum dots (adapted from the Ref. [105]). The bottom image shows the different colors available with colloidal quantum dots (adapted from Ref. [106]) **c)** Molecular Emitters: The molecular structure of dibenzoterrylene molecules and that of its anthracene host (DBT:Ac) is shown at the top. An SEM image is shown at the bottom, showing the possibility to grow this molecular emitters in the form of small-sized crystals (adapted from Ref. [60])

1.6.1 Color Centres in Diamond

Crystallographic defects are common in diamond crystal lattices because of extrinsic impurities or intrinsic anomalies. Color centers are defects in the diamond lattice that emit light when excited[107–109]. The nitrogen-vacancy (NV)[85, 99] center is a well-known example that has been extensively studied for quantum information processing applications. It has long spin coherence times also at room temperature. As for single photon generation, it is limited by a 4% emission in the so-called zero phonon line (ZPL). NV emits fluorescence at 637nm and exhibits strong photon antibunching[86]. Silicon (SiV)[110], Tin (SnV)[111] and Germanium (GeV)[112] vacancies centres are also deeply investigated. NV and SiV have been also employed as SPS for quantum key distribution[53].

1.6.2 Quantum Dots

Quantum dots (QDs) are tiny semiconductor[113, 114] particles of nanometric size that act as artificial atoms[115]. QDs exhibit excellent optical[101, 107] and electronic properties due to quantum confinement effects. The QDs are made up of a smaller band gap material inside a greater band gap material[114] and this band offsets causes the confining potential. This band gap gives rise to a discrete energy structure for holes and electrons. Electrons that are stimulated from the valence band to the conduction band leave holes. These carrier pairs then form quasi-particles, known as excitons, due to their mutual Coulomb attraction and may be trapped by the QD, where they can radiatively recombine through the emission of a photon. There are two primary types of quantum dots: self-assembled (Fig. 1.7 top image) and colloidal (Fig. 1.7 bottom image). The first is made up of II-VI semiconductor nanocrystals that were created using chemical synthesis. Nanocrystals emit by recombining an electron-hole pair produced by photon absorption. Molecular beam epitaxy is used to grow self-assembled QD through a process called Stranski-Krastanov[116]. QDs can be excited both via optical or electrical stimulation. CdSe in ZnS[117], InP in GaInP and InAs in GaAs can be optically excited[37] while InA can be effectively excited via e^- injection[118, 119]. QDs are extensively employed in optical quantum protocol and quantum key distribution[41, 47, 120, 121]. Using self-assembled QDs for the aforementioned applications is challenging because each QD's surroundings affects its features, and cryogenic temperatures are required to separate the QD from the phonon population.

1.6.3 Molecular Emitters

Molecular emitters have many advantages over other SPS because of their superior coherence properties and the flexibility of organic chemistry synthesis. They have distinct transition dipole moments and may be designed, manufactured, and incorporated into hybrid devices for various visible spectrum wavelengths. Organic molecules are appropriate for applications where scalability is desired due to their small size and simplicity of synthesis, holding billions of nominally identical emitters at low cost. At ambient temperature, they also produce very pure single-photons. Back in 1996, single molecules of pentacene hosted in *p*-terphenyl matrix showed photon anti-bunching[122][123] proving the eligibility of the system as a non-classical light source. Different molecules in a suitable solid or liquid [124] host matrix are studied. Recently, single organic molecules have shown remarkable quantum optical properties[60, 57]. In particular, our group has shown that anthracene nanocrystals doped with dibenzoterrylene (DBT:Ac NCs) exhibit photostable and life-time limited emission at 3K[88]. The primary benefit of molecular quantum emitters, which is also the thesis's objective, is that they can emit a single photons at room temperature with high purity. Future long-distance quantum communication networks operating on an intercontinental scale will require installation in isolated and inhospitable regions, such as through quantum satellite communication. This is crucial to ensure practical deployment and compatibility with ambient conditions, as cryogenic temperatures are not feasible in real-world settings. By enabling room-temperature operation[63]. , these networks can be seamlessly integrated into existing communication infrastructures, fostering widespread adoption and facilitating global connectivity. This will also reduce costs and complexity of the infrastructure and hence they are promising candidates as SPSs for quantum optical technologies.

Deviation from a TLS and coupling with the environment

In this section I will refer predominantly to molecules but the discussed phenomenology can be found in all solid state emitters, albeit with different impact. The spectral characteristics of molecules emission are significantly influenced by the solid matrix in which it is embedded. Specifically, Zero-Phonon Lines (ZPLs) are produced by the optical transitions from the excited state to the different vibrational levels of the ground state as shown in the Fig. 1.8. For the purely electronic transition (0-0 ZPL), the line typically has a Lorentzian shape, which corresponds to the Fourier transform of the population's exponential decay given by the following equation[125].

$$I(\nu - \nu_0) = \frac{1}{4\pi^2} \frac{\Delta\nu_{hom}^2}{(\nu - \nu_0)^2 + (\Delta\nu_{hom}/2)^2} \quad (1.14)$$

The center of the peak is denoted as ν_0 and $\Delta\nu_{hom}$ represents the width of the Lorentzian lineshape, which is commonly defined as the full width at half maximum (FWHM). The homogeneous linewidth is related to the pure dephasing time T_2^* and the finite lifetime τ of the excited electronic state. At cryogenic temperatures in a crystalline host matrix, the natural broadening of ZPL is solely determined by the lifetime of the electronic excited state ($\Delta\nu_{nat} = \frac{1}{2\pi\tau}$), which is inversely proportional to the lifetime (τ) of the state. In particular, as the dephasing due to phonons disappears at temperatures below 4 K, the ZPL in the DBT:Ac system becomes lifetime-limited. The natural width of the line is about 40 MHz, corresponding to a lifetime of 4.2 ns. This implies that the ZPL can be well-defined and narrow at cryogenic temperatures. Even below saturation, any measured linewidth of the

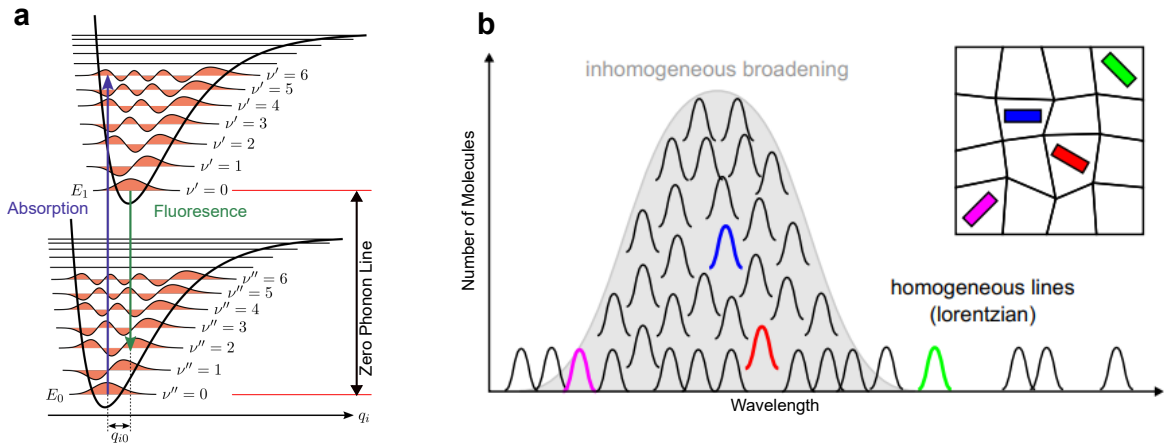


Fig. 1.8 Frank Condon Principle and Inhomogeneous broadening: **a)** The vibronic levels of a single molecule can be represented on a configuration diagram as a function of the nuclear displacement q . The transitions between these levels are depicted as vertical arrows. According to the Frank-Condon principle, these transitions occur on a timescale that is much shorter than the nuclear motion, thus ensuring that the atomic coordinate remains unchanged during the transition process. **b)** Real crystals contain various imperfections such as strain fields or defects which lead to the presence of different nano-environments, as illustrated in the inset. As a result, the Lorentzian ZPL transitions become inhomogeneously distributed in frequency (Adapted from the Ref. [126])

00-ZPL will suffer from power broadening. The true lifetime-limited 00-ZPL could only be measured at an excitation intensity $= 0$, as described by the equation:

$$\Delta\nu(I) = \Delta\nu_{hom} \sqrt{1 + \frac{I}{I_s}} \quad (1.15)$$

Next to each ZPL there is a Phonon Side Band (PSB). The PSB results from the transfer of molecular excitations into lattice vibrations due to electron-phonon coupling. Ideally, the emission spectrum for a specific vibrational mode would consist of discrete lines, each

corresponding to a specific number of phonons. However, in practice, the electronic states can couple to many different phonon modes with a large range of frequencies, each of which is hundreds of GHz broad (due to few picoseconds-long lifetime of the vibrations), resulting in spectra that usually form a continuous band. The PSB can be hence modeled with a Gaussian profile[127] and it is very broad, typically a few nanometers. Therefore, in order to have a strong, narrowband emission of indistinguishable photons, the emission into these broad sidebands should be minimized. The Debye-Waller factor accounts for whether the intensity of a given line goes into the ZPL or into the PSB, and is expressed as:

$$\alpha_{DW} = \frac{I_{ZPL}}{I_{ZPL} + I_{PSB}} \quad (1.16)$$

The Debye-Waller factor strongly depends on temperature[128].

Finally the strength of the 00-ZPL is related also to the branching ratio between the decay rate into the ground state $|S_0, \nu = 0\rangle$ and the rate of decay into all other vibrational sublevels. This branching ratio is determined by the Frank-Condon principle, which states that electronic transitions occur without altering the molecular configuration. In a configuration diagram as shown in Figure 2.2b, transitions are drawn as vertical arrows since they are so fast that the atomic coordinates remain unchanged. The intensity of the purely electronic line is measured in terms of the Frank-Condon factor, which expresses the overlap integral of the ground vibrational wavefunction between the electronic states. If the wavefunction overlap is poor, then the purely electronic line has a lower fluorescence probability in favor of other vibronic red-shifted lines. For DBT:Ac the product of the Debye Waller and the Frank-Condon factor can be as high as 50%[129]. The inhomogeneous broadening plays a crucial role in the detection and measurement of single-molecule emissions in solids and at low temperatures. In an ideal crystalline sample, each molecule would have identical optical absorption[130, 131], resulting in a narrow Lorentzian line at a specific frequency determined by the guest-host match. However, in real samples, each molecule absorbs light at a different frequency, resulting in an overall envelop profile known as inhomogeneous broadening. The width of this profile can vary greatly, from less than 1 GHz to 10 THz, depending on the host material's conditions. This distribution of resonance frequencies is caused by dislocations, point defects, or random internal electric and strain fields in the matrix[132], which are generally present and more prominent in amorphous materials. The overall profile is approximately Gaussian, with a range of center frequencies for the absorbers. This effect makes molecules valuable probes of the nano-environment, given their stable and narrow linewidth and the sensitivity of the absorption frequency to the surroundings. In particular, inhomogeneous broadening enables the spectral selection of individual molecules

for single-molecule spectroscopy. By using a low doping level sample and a narrowband tunable laser, it is possible to selectively pump one molecule at a time. It is also possible to use a lower doping and then employ off-resonant pumping to a higher vibrational level of the excited electronic state.

1.7 Applications of SPSs

Single Photon Sources are becoming increasingly important due to their applications in various fields, such as quantum information processing[63], quantum cryptography[41, 133, 64], and quantum sensing[134, 135, 65, 66]. Quantum communication[136] is the first step towards a quantum internet, and recent QKD (Quantum Key Distribution) experiments have been carried out using quantum emitters. These experiments have shown promising results, indicating the potential for SPSs to be used in the development of a quantum internet. In this thesis, QKD using molecular single photon sources[57] will be investigated. These sources are particularly interesting due to their high efficiency and ease of integration into existing technologies. The research will focus on improving the efficiency and reliability of these sources for practical applications in quantum communication at room temperature[40].

Chapter 2

Quantum Key Distribution

This chapter provides an overview of the historical context and evolution of QKD. This chapter delves into the different QKD security protocols and explains the principles behind each protocol. Additionally, the chapter explores various hacking strategies employed by malicious actors attempting to breach QKD systems. The security challenges of implementing QKD in practical scenarios are discussed, including the difficulties in scaling the technology and the impact of different factors on QKD security. Finally, the goal behind this thesis is outlined, which is to explore the potential application of molecular single photon sources for quantum communications at room temperature.

2.1 Classical vs Quantum Cryptography

The field of communication systems is continually evolving, keeping up with advancements in science and technology. Researchers and engineers are always looking for new discoveries and innovations to develop novel means and protocols that offer higher levels of communication security. Nowadays, billions of people are communicating and exchanging data simultaneously and cryptosystems have become a compelling need to guarantee that only intended recipients have access to information. Specifically, a cryptographic system provides the encryption of a plain message in a ciphertext by using an encryption algorithm. This, can only be decrypted by the receiver, who possesses the decryption key, to retrieve the original plain message. In classical cryptography, the cryptographic key is generated using a mathematical algorithm (e.g. based on the factoring problem) and security is based on what is called computational complexity, i.e. on the assumption that the solution of the mathematical problem is resolvable without the decryption key only by means of an extremely high computing capacity (practically being an improbable situation). In particular, there are two types of encryption techniques: symmetric and asymmetric. In symmetric

encryption the same private key is used to encrypt and decrypt messages, whereas asymmetric encryption is based on the use of two keys, a public and a private one. In this latter case, the sender (usually called Alice) uses the public key, which is accessible to everyone, to encrypt and send the ciphertext to the receiver (usually called Bob), who employs instead his private key to decrypt the ciphertext. The working principle of asymmetric encryption was firstly proposed in the pioneering work by the researchers Ron Rivest, Adi Shamir, and Leonard Adleman, who invented in 1978 the well-known RSA (Rivest–Shamir–Adleman) algorithm [10], summarized in the conceptual illustration in Fig. 2.1. Specifically, the

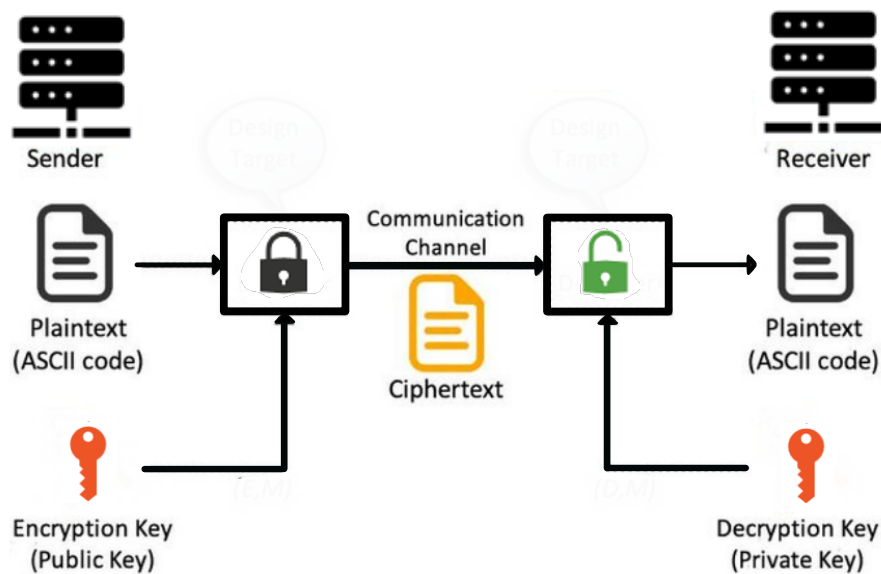


Fig. 2.1 Example of asymmetric cryptographic algorithm: The sender converts a plain text into a ciphertext using a public key, and the receiver uses his own private key to decrypt the ciphertext and retrieve the original message.

mathematical model behind RSA is based on the fact that the product of two large prime numbers into their constituent primes is computationally infeasible to factorize. Overall, RSA provides a secure method for encryption and decryption of messages, as long as the private key remains secret and the prime factors of the public key cannot be computed efficiently. It hence relies on the assumption that an eavesdropper has not the resources to resolve the factoring problem. Indeed, even for the most powerful classical supercomputer, factorizing a hundreds digits-long number would take hundreds of thousands of years. However, this concept of computational security was firstly threatened when Shor's Algorithm[17] was published, showing theoretically that a quantum computer can efficiently factorize prime numbers and resolves the previously mentioned problem in few seconds. Nowadays, this threat is made more tangible by the development of several available prototypes of quantum

computers, which already give proof of being orders of magnitude faster than supercomputers in the resolution of specific tasks[16, 137, 138]. In this context, classical cryptosystems can not be considered anymore secure, especially in a potential future when fully fledged quantum computers will be within reach and more efficient algorithms will be established. In particular, the advantage of quantum computers over their classical analogous lays in the principle of superposition of quantum states. While classical computation is based on binary digits which can assume the two alternative values "0" and "1", known as "bits" [139, 140], quantum technologies employ quantum bits as their logic units, called "qubits", which can exist in a superposition of quantum states, i.e. in a superposition of "0" and "1" at once. For the last decades scientists have been putting their efforts into building a large-scale quantum computer, and today the biggest available prototype of quantum computer - Osprey processor by IBM¹ - can account for 433 qubits².

In quantum cryptography, the security of communication leverages the fundamental laws of quantum mechanics such as the Heisenberg principle[141] and the no-cloning theorem[18, 142]. The best known quantum cryptography method is quantum key distribution (QKD), which offers an information-theoretically secure solution to the key exchange problem. Specifically, QKD employs single quantum systems (e.g. single photons - the 'flying qubits') to encode information in different possible degree of freedom (DOF), i.e. in different possible quantum states of the system: time-bin, wavelength, polarization, spatial mode, etc. The resulting qubits are hence used to generate the quantum key, which allows to encrypt and decrypt the message, while the message is delivered via a classical channel. The actors in this scenario are two users who want to exchange information privately at a certain distance, traditionally known as Alice (the sender) and Bob (the receiver), and Eve, the eavesdropper, who is trying to steal the information. In order to encode the information while guaranteeing minimum error and interception of secret keys, several communication protocols have been proposed and optimized. In particular, the first and most well known QKD protocol was introduced by Bennett and Brassard (BB84) in 1984[20], and its first experimental implementation was demonstrated in 1992[143]. Before continuing with a brief description of the most widely employed QKD protocols and encoding methods, focusing on the ones used in this thesis, we provide a deeper insight in the basics of the no-cloning theorem, which is at the core of information-theoretic security. In general, from now on, we will refer specifically on photonic qubits, since they will be the object of this thesis and they are in general the most widely used for encoding information in QKD protocols, owing to

¹<http://www.research.ibm.com/ibm-q>

²<https://newsroom.ibm.com/2022-11-09-IBM-Unveils-400-Qubit-Plus-Quantum-Processor-and-Next-Generation-IBM-Quantum-System-Two>

their unique advantages of low losses, efficient propagation at long distances, and easiness of manipulation.

2.2 General Concepts

The no-cloning theorem prohibits eavesdroppers from simply intercepting the communication channel and copying the transmitted quantum states for later decryption of the message[144, 145]. According to the theory, if information is encoded on non-orthogonal quantum states data security is assured by the impossibility of duplicating them. This can be shown through a simple mathematical demonstration.

We let H_a and H_b be two Hilbert spaces, and suppose that a cloning is possible by introducing U , a unitary operator, which can act on $H_a \otimes H_b$ such that for every state $|\psi\rangle_a$ and $|\phi\rangle_b$,

$$U(|\psi\rangle_a|\phi\rangle_b) = |\psi\rangle_a|\psi\rangle_b. \quad (2.1)$$

Consequently,

$$U|0\rangle_a|\phi\rangle_b = |0\rangle_a|0\rangle_b, \quad (2.2)$$

$$U|1\rangle_a|\phi\rangle_b = |1\rangle_a|1\rangle_b. \quad (2.3)$$

Now consider an arbitrary state $\alpha|0\rangle_a + \beta|1\rangle_a$ with $\alpha, \beta \in \mathbb{C}$. Then,

$$\begin{aligned} U(\alpha|0\rangle_a + \beta|1\rangle_a)|\phi\rangle_b &= \alpha U|0\rangle_a|\phi\rangle_b + \beta U|1\rangle_a|\phi\rangle_b \\ &= \alpha|0\rangle_a|0\rangle_b + \beta|1\rangle_a|1\rangle_b. \end{aligned} \quad (2.4)$$

From the definition of U , we also have

$$\begin{aligned} U(\alpha|0\rangle_a + \beta|1\rangle_a)|\phi\rangle_b &= (\alpha|0\rangle_a + \beta|1\rangle_a)(\alpha|0\rangle_b + \beta|1\rangle_b) \\ &= \alpha^2|0\rangle_a|0\rangle_b + \alpha\beta(|0\rangle_a|1\rangle_b + |1\rangle_a|0\rangle_b) + \beta^2|1\rangle_a|1\rangle_b. \end{aligned} \quad (2.5)$$

The final expressions in 2.4 and 2.5 are different unless $\alpha = 1$ or $\beta = 1$ (with the other parameter equal to zero), and hence such a U is not possible. As the original states must be preserved, no quantum machine can completely duplicate two separate, non-orthogonal quantum states.

2.3 QKD Protocols

Most quantum key distribution (QKD) protocols can be classified as either discrete-variable (DV) protocol or continuous-variable (CV) protocol, based on how information is encoded.

2.3.1 Discrete Variable QKD (DV-QKD)

In DV-QKD, information is encoded using a discrete set of single-photon states in combination with single-photon detectors[146]. It is one of the earliest and most well-developed QKD encoding methods and has been shown to be unconditionally secure. DV-QKD protocols can be implemented using a variety of different quantum states and measurement strategies, such as polarization-encoded qubits and time-bin encoding. The key challenges in DV-QKD research consist in improving the achievable key rates and increasing the maximum transmission distances over which secure key exchange can be achieved.

2.3.2 Continuous Variable QKD(CV-QKD)

In CV-QKD instead, the continuous properties of quantum states are exploited in combination with coherent detection [147, 148]. Unlike DV-QKD, CV-QKD operates on the quadrature of the electromagnetic field, which can be described as continuous amplitude and phase values[149], rather than on the discrete states of individual photons. CV-QKD protocols typically imply homodyne or heterodyne measurements to detect the quadrature values of the transmitted light, and can achieve high key rates over long distances with relatively simple experimental setups. Some of the key challenges in CV-QKD include the effects of channel losses and noise, which can limit the achievable key rates and require the use of advanced error correction techniques. Several experimental demonstrations of CV-QKD have been reported, including demonstrations over fiber-optic links[150, 151] and free-space channels[152–155].

Prepare-and-Measure Protocol

The prepare-and-measure QKD protocol is widely employed for its merits of fast speed, high key generation rate, and easy implementation. In this protocol, the sender (Alice) randomly prepares qubits in one of two possible states of single photon's DOF (especially polarization) and sends them to the receiver (Bob) over a quantum channel. Bob then performs a measurement on each qubit using one of two mutually orthogonal bases. After the measurement, Alice and Bob compare the bases used, and keep only the qubits that were measured in the same basis. These qubits are used to establish a shared secret key. This

protocol has been studied extensively and numerous variations and extensions have been proposed. One example is the BB84 protocol[20] and the E91 protocol[156], which was proposed by Artur Ekert in 1991.

2.4 BB84

The first QKD protol was conceived by Charles H. Bennett and Gilles Brassard in 1984[20], namely the BB84 protocol. Evesdropping events are outlawed by performing the choosing between two mutually unbiased bases (MUBs) at each encoding event, following a series which is only known to Alice and Bob. Specifically, MUBs consist in sets of orthonormal bases in a Hilbert space such that the inner product between any two states from different bases is equal to $1/\sqrt{d}$, where d is the dimension of the associated Hilbert space. In other words, the bases are as "unbiased" as possible with respect to each other, meaning that no basis provides more information than another when measuring a state. The steps involved in BB84 are summarized in the following and shown in Fig. 2.2, where we consider the specific case of polarization encoding of single-photon qubits.

- Two typical examples of MUBs bases are the so-called Z-basis, consisting in the set of horizontal and vertical -polarization states ($|H\rangle$, $|V\rangle$), and the X-basis, consisting in the set of diagonal and anti-diagonal -polarization states ($|D\rangle$, $|A\rangle$). In particular, the qubit polarization encoding is defined as follows:

$$|H\rangle = |0\rangle; \quad (2.6)$$

$$|V\rangle = |1\rangle; \quad (2.7)$$

$$|D\rangle = \frac{1}{\sqrt{2}}|0\rangle + \frac{1}{\sqrt{2}}|1\rangle; \quad (2.8)$$

$$|A\rangle = \frac{1}{\sqrt{2}}|0\rangle - \frac{1}{\sqrt{2}}|1\rangle. \quad (2.9)$$

- Each single photon received by Bob is then analyzed by choosing the basis measurement. If Bob chooses the same basis as Alice, he gets a correct output. If he chooses the wrong basis, the output is random, following from the quantum superposition

principle, i.e. there is usually a 50% probability that Bob chooses the same bases sent by Alice (e.g. in the case of equal probability of the bases).

- Alice and Bob discard all the events for which they did not use the same basis. After that, they will end up having the same identical string of bits called sifted key.
- Information reconciliation process is performed, i.e. error correction and privacy amplification.
- The security of BB84 lies in encoding information in non-orthogonal states. Eve can not clone the state unless she knows the exact sequence of the basis used by Alice because of non-orthogonality.

Alice's bit	0	1	1	0	1	0	0	1
Alice's basis	+	+	X	+	X	X	X	+
Alice's polarization	↑	→	↖	↑	↖	↗	↗	→
Bob's basis	+	X	X	X	+	X	+	+
Bob's measurement	↑	↗	↖	↗	→	↗	→	→
Public discussion								
Shared Secret key	0		1			0		1

Fig. 2.2 BB84 Protocol: Alice prepares a random sequence of qubits encoded either via the Z-basis (denoted by + in the figure) or via the X-basis, and sends them to Bob through a quantum channel. Bob randomly measures each qubit either of the two bases, recording his measurement basis for each analyzed qubit. After the transmission, Alice and Bob publicly announce their respective basis choices and discard the qubits measured in different bases, and perform error correction and privacy amplification on the remaining ones.

Any discrepancy between the expected and the observed results can indicate the presence of an eavesdropper who is attempting to gain information about the transmitted bits. Alice and Bob can determine the Quantum Bit Error Rate (QBER) (see Chapter 2.8) by performing a parameter estimation session, in which they reveal a random subset of their data and compare these bits which are later discarded. The QBER can then be quantified and compared against a certain security threshold of the protocol. If the QBER is higher than the threshold, it

implies that Eve has gained too much information. Conversely, if the QBER is lower than the threshold, it indicates that the parties have more shared information than Eve. Alice and Bob can then utilize classical procedures of Error Correction (EC) and Privacy Amplification (PA) to derive a secret key (see Chapter 2.8). To extract information, Eve can use the Intercept-Resend strategy, where she randomly chooses either the Z or the X basis. By doing so, she uses the correct basis with a 50% probability, in which case she can eavesdrop on all the input information without introducing any noise. However, with a 50% probability she uses the wrong basis: in this case the bit eventually received by Bob will be correct only 50% of the times, substantially increasing the QBER with respect to the case of no eavesdropper at work. To ensure security in BB84, the QBER must not exceed the threshold of 11%.

2.5 Quantum Hacking

While theoretically QKD offers unconditional security, in practice, the security of the quantum communication protocol dependent on the effectiveness of the implemented security measures. The presence of errors in the performance of the communication protocol and of imperfections in Alice's and Bob's communication devices can indeed open back doors in the security and allow Eve to intercept and decode the transmitted information[157]. Often, the security of the protocol is based on the assumption that the communication channels are secure and that the devices used by Alice and Bob are trustworthy. However, attacks on both Alice and Bob side should be taken into consideration and can potentially compromise the security of the full communication system[158]. As an example, limited precision in state preparation is a typical experimental circumstance which opens the protocol to side channels attacks. For instance, in the case of weak coherent pulses (WCP) -based protocols, photonic qubits are encoded by using strongly attenuated laser pulses rather than single-photon Fock states. The consequent non-zero probability of having multi-photon events per pulse, set the ground for Eve to launch photon number splitting (PNS) attacks [21](see Section 2.5.1). Another example comprises Trojan horse attacks[159, 160], where an attacker modifies the internal components of one or both of the trusted parties' devices to inject quantum systems into in order to gain information e.g. about Alice's choice of basis and about Bob's choice of measurement basis. In general, Bob's side is considered to be more susceptible to hacking attacks than the source. This is due to the fact that the transmission channel can be easily controlled by Eve, who can send any type of signal to Bob compromising the security of the system. Indeed, Bob has no way of knowing whether the signals he receives are legitimate or have been tampered. Eve can take this advantage for instance to perform time, shift attacks[161] and fake state attacks[162, 163]. Among the wide variety of different types of

attacks that have been reported, we provide in the following a deeper description of the PNS attacks, which more closely relate to the work presented in this thesis.

2.5.1 PNS Attack on WCP

Considering DV-QKD algorithms, the photon number splitting attack[21, 164–166] is one of the most relevant hacking strategies. Imperfect single photon sources with pulses containing more than one photon are prone to the possibility of splitting off the signal and extrapolating the extra photon to allow for the measurement of the state without affecting the original message. As a matter of fact, the most widely used source for QKD for its high degree of reproducibility and control is an attenuated laser providing weak coherent pulses WCP[167–170]. Inherently, WCP exhibit non-zero probability of containing more than one photon per pulse because the emission statistics follows the Poissonian distribution (see Section 1.3) typical of coherent sources. Mathematically, the probability distribution of finding n photons in a time interval Δt is given by P_n :

$$P_\mu(n) = \frac{\mu^{-n} e^{-\mu}}{n!} \quad (2.10)$$

where μ denotes the average photon number per pulse. Hence, in the case of a multi-photon pulse, Eve, for whom unlimited resources are assumed, can retain one photon in her quantum memory and send the rest to Bob after measuring the quantum state. Finally, by listening to Alice and Bob's communication in the classical channel she can successfully measure the photons stored in her memory by using the basis announced by Alice and Bob.

In this context, characterizing the source employed in the QKD scheme is a crucial step to assess the probability of obtaining a multi-photon pulse, denoted as P_m . Indeed, in order to evaluate the maximum achievable secret key rate, Alice and Bob must take into account the worst-case scenario where Eve obtains complete information about each multi-photon pulse sent by Alice. Another fundamental parameter to determine is the detection probability, i.e., in practice, the probability to have a click in the single-photon detector, defined as P_{click} , which can be retrieved by characterizing the source efficiency as well as the channel conditions at Bob side. By characterizing their devices, Alice and Bob can evaluate the maximum achievable secret key rate by introducing a correction factor ascribing for possible multi-photon events ($A = (P_{click} - P_m)/P_{click}$ - see Section 2.8). While in the case of WCP multi-photon events can be reduced only at the expense of the achievable emission rate, making key exchange at longer distance difficult, an effective strategy to otherwise reduce PNS attacks consists in employing decoy state protocols[35].

2.6 Decoy State Protocol

The decoy-state method is a very efficient resource for QKD systems lacking of truly single-photon sources, since it enables to detect the photon number splitting attacks from some additional parameters to be estimated during the protocol. As a result, Eve has to put a limit on her beam splitting attacks if she does not want the protocol to be aborted. The implementation of a decoy state protocol in WCP-based QKD schemes involves generating attenuated light pulses which are totally identical to each other, except for their mean photon number μ , which is randomly chosen, for each quantum state to be prepared, among different values ($\mu = \mu_1, \mu_2, \mu_3, \dots$)[171–174]. The additional values of μ to be included in the protocol are referred as decoy states, while the pulses belonging to the μ_1 distribution are called signal states. According to this protocol, after the N rounds of quantum communication, Alice announces, on the classical channel, the value of μ that was chosen for each round. Hence, if only the detection events coming from the signal intensity μ_1 are used to collect the secure key bits, even if Eve measures the actual photon number of each pulse she can not know which distribution ($P_{\mu_1}(n); P_{\mu_2}(n); P_{\mu_3}(n); \dots$) is the one related to the useful signal. Therefore, if she acts differently based only on the value of n , she ends up introducing alterations on the experienced distributions at Bob's side, since Bob will observe different channel loss for the different μ intensities. As a result, Eve has to restrain herself in blocking the useful single-photon pulses, from which she can acquire information only at the expense of introducing errors. The decoy state protocol has been experimentally demonstrated in various QKD systems and has been shown to significantly increase the maximum communication distance[175].

2.7 Motivations for the Thesis

From the previously depicted context of practical QKD implementations, it clearly emerges that real physical communication devices have to deal with performance errors and imperfections, and with the consequent opening to communication channel attacks despite the information-theoretic security of QKD. While WCP-based sources are the most commonly employed ones to date for QKD applications owing to the easiness of implementation and cost-effectiveness, they as well can not guarantee full security even upon the use of decoy-state protocols owing to the complexity of the implementation and the inherent probability of introducing errors. An alternative strategy to this scenario consists in using truly single-photon states conveyed by deterministic quantum emitters. In this case, the probability of multi-photon events is indeed inherently suppressed. In this thesis, we propose, as

single-photon emitter, single organic molecules embedded in crystalline host matrix, which have given proof of excellent photophysical properties. Furthermore, they offer the unique advantage of operation at room temperature, as opposed of the majority of other quantum emitters in the solid state. In Chapter 3, we present the characterization of molecular emitters at cryogenic temperatures, necessary for suppressing dephasing and achieving coherent emission, a key aspect for the implementation of more complex QKD protocols. In Chapter 4, we present a testbed QKD experiment employing molecular emitters as single-photon sources at room temperature, using a BB84 protocol and polarization encoding.

2.8 Formulae Compendium

In this last section of the chapter, we report the main formulae employed in Chapter 4 to evaluate the maximum secret key rate (SKR) which can be achieved by the molecular source and, for comparison, by a WCP-based protocol and by a decoy-state protocol. The SKR is indeed the crucial parameter which attests the ability of the QKD system to generate a secure key against the presence of any potential eavesdropping. A fundamental prerequisite to its evaluation is the measuring the Quantum Bit Error Rate (QBER) associated to the communication device, which is the ratio of the committed error rate to the key rate, or otherwise, the mismatch probability of the signals sent and received between Alice and Bob. The QBER, quantifies the amount of information Eve can potentially obtained by measuring the quantum state without being detected by leveraging on the protocol errors. In particular, if the QBER is higher than $\approx 11\%$, the generated key is considered not to be secure for the too high probability of Eve gaining information. In contrast, a low QBER indicates that the generated key is secure.

For the extrapolation of the expected SKR as a function of the communication distance, the QBERs shall be measured for a set of corresponding channel losses, which can be typically emulated experimentally by inserting a varying set of attenuators in the communication channel. Then, the signal, the communication channel and detection process shall be characterized to evaluate the corresponding efficiencies. In particular, the source efficiency (μ_{mol}) is given by the overall detected single-photon count rate normalized to the trigger excitation rate (the repetition rate of a pulsed laser). The probability of detecting a signal event is hence expressed by $P_{mol} = \eta \mu_{mol}$, where $\eta = \eta_{Bob} \eta_{channel}$, with $\eta_{Bob} = \eta_{opt,B} \eta_{det}$ being the efficiency of Bob's side including the optics and the detector, and $\eta_{channel}$ being the communication channel loss.

From the set of measured values for the QBER as a function of $\eta_{channel}$, the following

expression for the is used to extract the fitting parameters corresponding to the detector dark counts (P_D) and the detection error probability (e_{det}):

$$\text{QBER}_{mol} = \frac{P_D/2 + e_{det} P_{mol}}{P_D + P_{mol}}. \quad (2.11)$$

In particular, this same expression can be employed for the WCP case, after replacing P_{mol} in eq. 2.11 with $P_{WCP} = 1 - \exp(-\eta \mu_{WCP})$, where μ_{WCP} is the efficiency of the WCP, analogously calculated[176]. The fitting expression is hence changed as follows:

$$\text{QBER}_{WCP} = \frac{P_D/2 + e_{det}(1 - e^{-\eta \mu_{WCP}})}{P_D + 1 - e^{-\eta \mu_{WCP}}}. \quad (2.12)$$

For the evaluation of the expected SKR as a function of channel losses, the multi-photon events probability of the single-photon source (SPS) shall be characterized via the second order correlation function evaluated at zero time delay, $g^{(2)}(0)$ (see chapter 4.4). The resulting overall multi-photon probability is given by $P_m = \mu_{mol}^2 g^{(2)}(0)$ [41]. The expected SKR is hence evaluated using the expression derived in Ref. [43], which reads:

$$\text{SKR}_{SPS} = \frac{1}{2} P_{click} [\beta \alpha(\text{QBER}_{mol}) - f(\text{QBER}_{mol}) H(\text{QBER}_{mol})], \quad (2.13)$$

where the factor $1/2$ stems from the sifting ratio for symmetric basis encoding, $P_{click} = \mu_{mol} \eta + P_D$ is the probability of having a click in the detector, $\beta = (P_{click} - P_m)/P_{click}$ is the correction factor for possible multi-photon events, H is the standard binary Shannon information function, $\alpha(x) = -\log_2(1/2 + 2x - 2x^2)$ and $f(\text{QBER}_{mol})$ is the error correction efficiency [41], where we used $f(x) \simeq 1.22$.

In order to compute the SKR for the WCP with decoy method, we follow the work in ref. [176] assuming an optimal choice of μ_{dec} and decoy ν_{dec} (using two values of pulse intensity - see Chapter 4.5). The fitting expression in this case is the following:

$$\text{SKR}_{decoy} = \frac{1}{2} [Q_1(1 - H(e_1)) - Q_\mu f(\text{QBER}_\mu) H(\text{QBER}_\mu)], \quad (2.14)$$

where we evaluate the set of parameters according to the expressions below:

$$\begin{aligned}
Q_1 &= \frac{\mu^2 e^{-\mu}}{\mu \nu - \nu^2} K_{\nu\mu} \\
Y_1 &= \frac{\mu}{\mu \nu - \nu^2} K_{\nu\mu} \\
e_1 &= (\text{QBER}_\nu Q_\nu e^\nu - P_D/2) / \nu Y_1 \\
K_{\nu\mu} &= Q_\nu e^\nu - Q_\mu e^\mu \nu^2 / \mu^2 - P_D(\mu^2 - \nu^2) / \mu^2,
\end{aligned} \tag{2.15}$$

In particular, $Q_\mu = P_D + 1 - e^{-\eta\mu}$ and $Q_\nu = P_D + 1 - e^{-\eta\nu}$. If the experimental detector errors are very similar for μ and ν , the above parameters can be simplified to the one photon error rate of $e_1 = \frac{P_D/2 + e_{det}\eta}{P_D + \eta}$ and the one photon gain of $Q_1 = (P_D + \eta)\mu e^{-\mu}$.

Finally, the WCP SKR without decoy signal can be obtained from:

$$\text{SKR}_{WCP} = \frac{1}{2} \eta \mu_{opt} e^{-\mu_{opt}} FQ, \tag{2.16}$$

where $FQ = 1 - H(2\text{QBER}) - H(\text{QBER})$ and the optimal $\mu_{opt} = \eta FQ (1 - H(2\text{QBER}))^{-1}$.

Chapter 3

Experimental Characterization of Organic Molecule Based SPS

In this chapter, organic Molecule Based SPSs are investigated. Explored Key aspects include crystal growth, emitter concentration in the host matrices, techniques for protecting nano-crystals against sublimation, as well as the probing purity, indistinguishability, and various collection strategies. Additionally, the temporal and spatial stability of two-photon interference is thoroughly studied to ensure optimal performance of the SPS. It is worth noting that this SPS has been further developed for optimized application in QKD experiment at room temperature, which will be the argument of the subsequent chapter.

3.1 Introduction

Ideal quantum sources providing triggered indistinguishable single photons with negligible spectral diffusion as well as scalability potential are still today a major challenge[177, 64]. Quantum dots [178][101], Individual cold atoms, color centers in diamond [179][180][181] and molecules[182, 183] have been extensively investigated till date. Every quantum emitter comes with advantages and drawbacks for particular applications. Single organic molecules have shown remarkable quantum optical properties when integrated in an appropriate host matrix; e.g. single molecules of dibenzoterrylene in anthracene (DBT:Ac) exhibit bright and photostable emission at room[184] [40] and cryogenic temperature, with life-time limited linewidth at 3K[185, 186, 57, 58, 187, 188]. These features make organic dye molecule-based quantum emitters promising candidates as indistinguishable single photon sources with emission from the lowest pure electronic transition (00-Zero Phonon Line -ZPL). In this chapter, DBT:Ac NCs are thoroughly presented as SPSs, considering different key aspects

as sample preparation strategies and photophysics. The system is here characterized at cryogenic temperatures. In particular, some possible advantages over other SPSs will be briefly discussed.

3.2 Crystal Growth

The quantum light source on which my work has been focused is based on single organic molecules of polyaromatic hydrocarbons (PAH). Both the dibenzoterrylene fluorophore (DBT) and the anthracene crystalline host matrix belong to this family. A simple and cost-effective method has been recently developed in the group to grow anthracene crystals of sub microns size doped with DBT molecules, in which the concentration of DBT can be controlled to achieve the single molecule limit. Remarkably, the high quality crystallinity achieved in these particles determines the preservation of the fluorophore optical properties, which look almost unaffected with respect to the result established in the bulk, a non-trivial adjustment in sub-micrometric environment according to the literature[60]. The utilization of molecular emitters in NCs have gained significant interest in recent years.

3.2.1 The Fabrication of Anthracene Doped with Controlled Concentration of DBT

Microcrystal growth by reprecipitation has been studied for several decades and was introduced for the first time in 1992[189]. In Ref. [60] we apply similar techniques to our guest-host system. Indeed, SPSs based on organic hydrocarbon compounds have proven to be excellent quantum light sources since the early nineties. However, these results were generally obtained in extended crystalline environments, hundreds of nm thick and tens of μm wide, where high crystallinity and proper isolation from oxygen could be granted. Such geometrical constraints have limited the portability of the source, and hence the possibility of integration in photonic structures and more in general the attainable collection efficiency and single photon purity. In particular, Ac serves as a host matrix for DBT and offers various advantages. One of them is its affordability and simple purification and handling. Additionally, AC remains stable at room temperature and doesn't experience any phase transition when cooled. Furthermore, AC can be easily fabricated, enabling the production of high-quality crystals with a thickness of only a few tens of nanometers. The resulting crystals are highly pure, highly crystalline, and exhibit excellent optical and electronic properties, making them suitable for use in a wide range of applications. The whole procedure is presented below and graphically schematized in the Fig. 3.1.

- Prepare a solution of DBT in Toluene with concentration 1mg/2mL. Mix the contents of the vial by means of a sonicator until the DBT has completely dissolved in Toluene. This solution will be used as a solute for further steps.
- Prepare a solution of Anthracene in Acetone with concentration 9mg/10mL (saturated solution). Mix the contents of the vial by means of a sonicator until the Anthracene has completely dissolved in the Acetone.
- Mix 15uL of the DBT in Toluene solution prepared in step 1 with 4mL of the Anthracene in Acetone solution prepared in step 2. This mixture results in a 10uM solution of DBT in Acetone. Use sonicator every time until the solution is homogeneous. This step is crucial to create the desired concentration of DBT impurities in Anthracene. At this stage solution equals to 1 DBT molecule per 2000 Ac molecules.
- In order to prepare solution of lower concentrations of DBT in Anthracene, repeat the following steps using the 10uM suspension prepared in these two steps.
 - Mix 10uL of the 10uM solution with 1mL of the Anthracene in Acetone solution, hence attaining a 100nm solution of DBT in Acetone.
 - Repeat this process until a suspension with a concentration of 10pM or 0.1pM is obtained. These solutions can be stored for future use
- Finally, to prepare the DBT:AC nanocrystals suspension, mix 100uL of the solution with the desired concentration (either 10uM, 10pM, or 0.1pM) with 2mL of milli-Q water under sonication. The mixture should be sonicated for 30 minutes with the lid of the vial slightly opened. The NCx form by reprecipitation.

The resulting suspension of DBT:Ac nanocrystals in water can be stored for long-term use. It is recommended to store the vial in the dark, e.g. in a refrigerator at a temperature between 2-8°C to prevent degradation or other changes in the sample. The DBT:Ac suspension can be stored in the fridge for several months without any significant loss of quality or purity.

3.2.2 Sample Preparation and Protection of NC's

The general procedure used to obtain SPS sample form the suspension is based on drop-casting followed by desiccation of water. The desiccation method is a commonly used technique for preparing samples for various analytical and imaging applications. The procedure involves the removal of water from a solution or suspension, leaving behind a dry and stable sample for further processing or analysis. In the case of DBT:Ac, a small amount

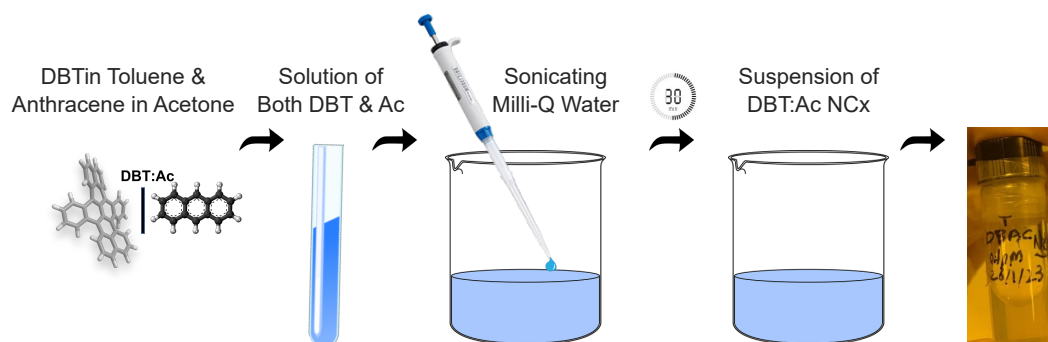


Fig. 3.1 DBT:AC NCx Preparation: Process start with dissolving 0.75mg of DBT in 1.5mL of Toluene & 9mg of Anthracene in 10mL of Acetone. The mixture is then carefully prepared by controlled concentration of DBT. Finally, the solution is mixed with milli-q water and sonicated for 30 minutes to produce DBT:Ac Suspension of Nanocrystals

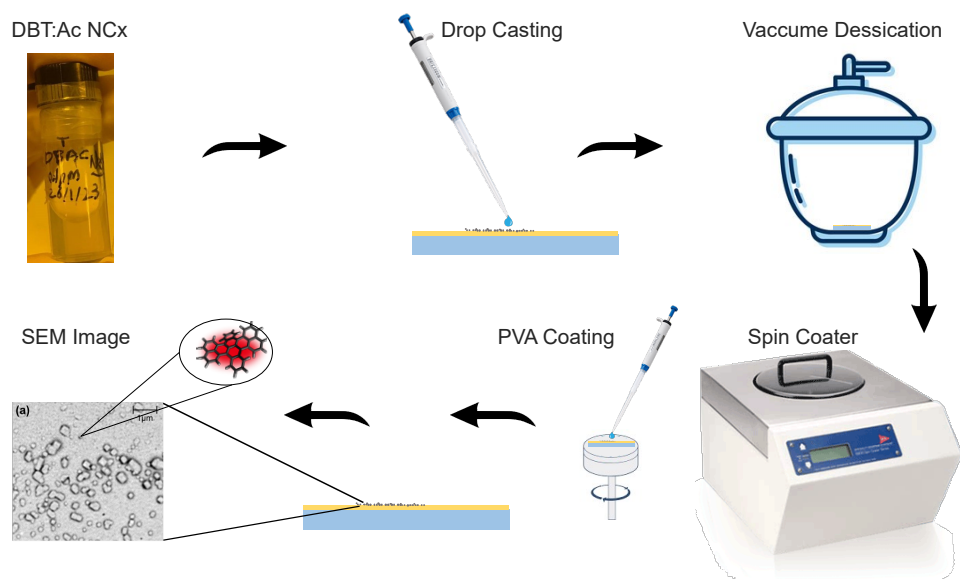


Fig. 3.2 Sample Preparation: First of all 15uL of DBT:Ac suspension is drop casted on gold coated silica substrate with then put it in the vacuum desiccator and wait until water is evaporated. To protect NCx against matrix sublimation, PVA coating with 200 nm thickness is done using a Spin coater.

(15 μ L) of the DBT:Ac solution is drop-casted onto the selected substrate, which is then placed into a desiccator as shown in Fig. 3.2. The desiccator is designed to create a low-pressure environment, which promotes the evaporation of water from the sample. The desiccation process typically takes up to 30 minutes. Once the water has been completely evaporated, the resulting DBT:Ac nanocrystals are left. However, to protect the nanocrystals, a layer of Polyvinyl Alcohol (PVA) is applied on top of the nanocrystals using a spin coating technique as shown in Fig. 3.2. The PVA layer acts as a protective coating, which prevents the nanocrystals sublimation. The substrate with the DBT:Ac nanocrystals is placed onto the spin coater, and a specific amount of PVA solution in water (generally 5% in weight) is added on top of the NCx. The spin coater is then activated, and the substrate rotates at high speed causing the PVA solution to spread uniformly across the surface of the substrate. The thickness of the resulting layer can be modulated varying the rotation speed. Once the spin coating process is complete, the sample is ready to use for the experiment. In total, the entire sample preparation process, which includes desiccation and spin coating, can be completed in less than one hour. This is an efficient and timely process, which is essential for obtaining accurate and reproducible results in a timely manner.

3.3 Experimental Setup

DBT doped anthracene samples are investigated at room and cryogenic temperature using confocal microscopy. First, we perform wide-field illumination to find a bright and isolated single molecule of DBT. A home-built experimental setup is used to excite single molecule and then collect fluorescence with a single objective lens in the so-called epifluorescence configuration. The experimental optical setup is shown in Fig. 3.3. It can be divided into excitation, collection and detection. DBT:Ac's is placed inside a cryostat (Montana Instrument) which is a closed cycle helium cryostat where the temperature can reach 2.7K. The excitation line consist of different lasers, galvo mirror, half wave plates, polarization beam splitters and finally epi-fluorescence microscope (Mitutoyo Plan Apo 100x) with 0.7 Numerical Aperture (N.A.). A Longpass filter (Semrock LP02-785RE) is chosen for its ability to allow long wavelength light to pass through while blocking shorter wavelengths. The next step involves separating the zero-phonon line (ZPL) component at 783.5 nm from the phonon sideband (PSB) by means of a reflective Notch filter with a width of 0.4 nm (OptiGrate model BNF-785-OD4-12.5M). The separated ZPL component is then directed into a single-mode fiber. A key aspect of the setup is the possibility to investigate the indistinguishability between photons that are consecutively emitted. This is achieved by dividing the photon stream into two paths using a polarizing beam splitter cube (PBS), and

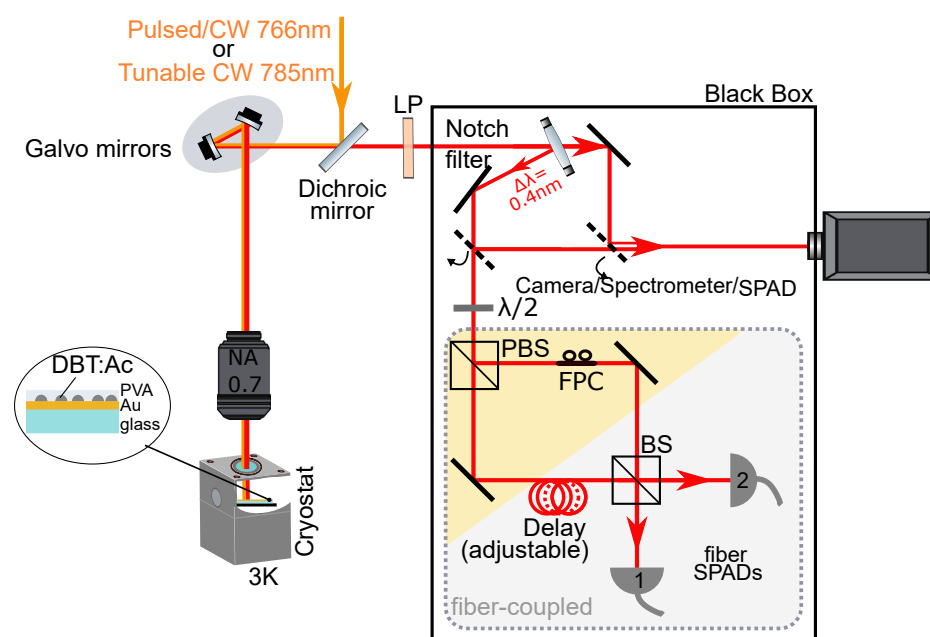


Fig. 3.3 Experimental Setup: A Picoquant laser operating at central wavelength of 766 nm is used, which can be operated both in pulsed and CW mode. DBT:Ac NCs are placed inside a cryostat at 3K. An epi-fluorescence microscope (0.7-N.A. objective) is used for excitation and collection of emission. 0.4-nm wide notch filter is employed to filter the ZPL from the phonon side band (PSB). Delay lines of different lengths and a fibered beam splitter (BS) are used in the interferometer. EMCCD Camera is used to image the fluorescence and a free-space-coupled single photon avalanche diode (SPADs) are employed to analyze the PSB and ZPL. Fibered SPAD's output is connected to time tagging system to reconstruct the histogram and arrival times of single photons.

placing a fiber polarization control (FPC, Thorlabs model FPC023) in front. To prevent any temporal correlations between the photons in the two paths, one of the paths is delayed by 40 ns using an 8 m-long fiber. This delay is significantly longer than the excited state lifetime of approximately 4 ns. In this way there is no memory left of temporal correlations and the two arms operate as if pumped by independent single photon sources. When the FPC is oriented such as to have the whole intensity on one arm, the setup measures the simple second order autocorrelation function in the so-called Hanbury Brown Twiss configuration. In order to measure quantum interference in the train of single photon pulses, an unbalanced fiber-based Mach-Zehnder interferometer (MZI) is utilized and the set up is used in the Hong-Ou Mandel configuration. Specifically, another FPC unit is placed on one path to switch between parallel and orthogonal configurations before the MZI is closed on a fibered 50/50 beam splitter (BS) (Thorlabs model TN785R5A2). The two output ports of the MZI are ultimately linked to a pair of single photon counting modules (Excelitas model SPCM-NIR-14, with a quantum efficiency of 70%). Overall, this experimental setup provides a robust method for investigating the indistinguishability of consecutively emitted photons and measuring quantum interference in the train of single photon pulses. By carefully selecting and implementing various optical filters, beam splitters, and fiber components, this setup is able to effectively manipulate and measure single photons in a controlled manner, which is crucial for many applications in quantum optics and quantum information processing.

3.4 Optical Characterization at Cryogenic Temperature

In order to effectively compare the performance of DBT as a quantum emitter to other cutting-edge quantum emitters, it is essential to conduct a comprehensive benchmarking analysis of the SPS. Such an analysis is necessary to evaluate the efficiency of fluorescence emission from a single DBT molecule at cryogenic temperatures, with particular emphasis on key figure of merit such as brightness, triggered operation, purity and indistinguishability. The benchmarking process involves the systematic evaluation of these critical parameters to provide an accurate assessment of the SPS's performance. Brightness measures the probability that an excitation event end in the emission in the desired EM mode. Triggered operation is a crucial figure of merit as it measures the ability of the SPS to produce single photons when required, as opposed to a continuous stream of photons. Purity, on the other hand, refers to the probability of multi-photon emission without any additional background noise or spurious signals. Finally, indistinguishability measures the interference ability of distinct photons, which is critical for applications such as quantum communication and cryptography (see Chapter 1 for definitions and more details). By conducting a comprehensive

benchmarking analysis of DBT as a quantum emitter, researchers can determine the efficiency of the SPS and compare it to other state-of-the-art quantum emitters.

3.4.1 Hanbury Brown-Twiss (HBT) Configuration

The HBT setup with TCSCP is shown in Fig. 3.4a. Single photons impinging on the SPADs are used to start and stop both inputs of a TCSCP module (PicoHarp300 by PicoQuant), which registers all the events with high precision. SPADs have high quantum efficiency with time jitters less than 100ps. Fig. 3.4b shows such histogram around zero time delay under CW operation. Anti-bunching dip around zero time delay shows suppression of multi-photon emission events under CW operation. The histogram is a valid estimation of the $g^2(t)$ without further processing until the probability of detecting a photon in the considered time interval is low (in our case it's always $< 1\%$). In a simple model considering weak CW coherent pumping $g^2(t)$ is given by:

$$g^{(2)}(\Delta t)_{HBT} = 1 - b \times e^{(-|\Delta t|/\tau_{HBT})} \quad (3.1)$$

where τ_{HBT} accounts for spontaneous emission life time and Δt is the delay in the arrival time. Best fit to the data using equation 3.1 gives $g^2(0) = 0.03 \pm 0.02$. This shows the purity of single DBT molecule emission. In order to have single photon on demand, pulsed excitation

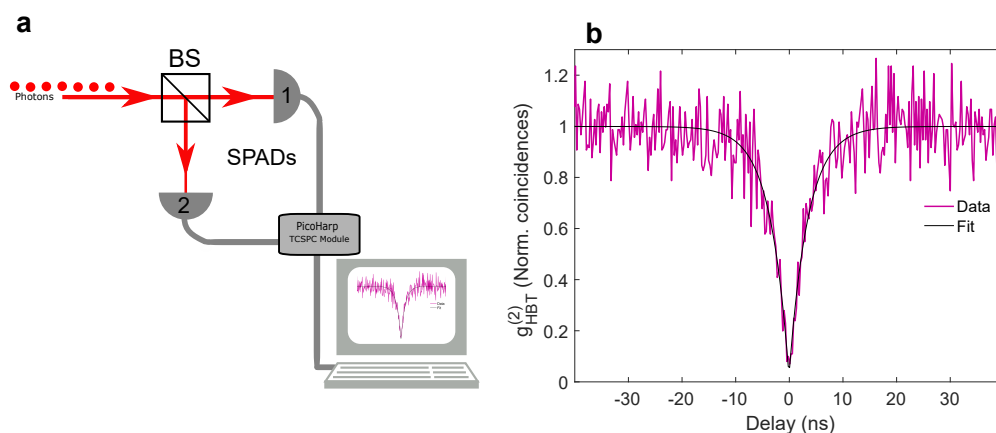


Fig. 3.4 Purity of Single DBT Molecule: (a)HBT Setup: Photons are split by by 50:50 BS and both photon streams are detected by two fibered SPADs are processed through the TCSCP module to reconstruct $g^2(t)$ function. (b) Second order correlation function $g^2(0)$ for single DBT emission under CW excitation(no photons in the delay line arm). Best fit to data shows $g^2(0) = 0.03 \pm 0.02$.

is necessary. In the Fig. 3.5a), $g^2(t)$ for the same DBT molecule is reported for the case of operation by PicoQuant Laser at central wavelength of 766 nm with 80 MHz repetition rate.

The resulting histogram of relative arrival time is fitted using the following equation 3.2.

$$g^{(2)}(\Delta t)_{Pulsed}^{HBT} = A_0 \cdot e^{-\frac{|x-t_0|}{\tau}} + A_1 \cdot e^{-\frac{|x-(t_0-3T)|}{\tau}} + A_1 \cdot e^{-\frac{|x-(t_0-2T)|}{\tau}} + \quad (3.2)$$

$$+ A_1 \cdot e^{-\frac{|x-(t_0-T)|}{\tau}} + A_1 \cdot e^{-\frac{|x-(t_0+T)|}{\tau}} + A_1 \cdot e^{-\frac{|x-(t_0+2T)|}{\tau}} + A_1 \cdot e^{-\frac{|x-(t_0+3T)|}{\tau}}$$

where A_0 is the amplitude of the peak around zero time delay and A_1 is the peak amplitude for the peak corresponding to distinct events. The peak characteristic time is denoted by the symbol τ while “ T ” represents the repetition period of the laser. nT is used to indicate the order number of the lateral peaks. According to best fit of the data yielded $g^{(2)}(\Delta t)_{Pulsed}^{HBT} = 0.008 \pm 0.008$. Spontaneous emission life time τ can be also independently evaluated by correlating single photon arrival time with laser trigger pulses (see Fig. 3.5a). From the best fit of the data life time $\tau = 4.01 \pm 0.01$ is obtained.

Excitation spectroscopy is used to measure the ZPL linewidth shown in Fig. 3.5b). In this technique, a CW narrow-band laser is tuned at frequencies close to the ZPL. Then the emission intensity in the Phonon side band (PSB) is monitored while scanning the laser frequency across the ZPL. recorded as a function of the excitation laser frequency, scanning across the ZPL.

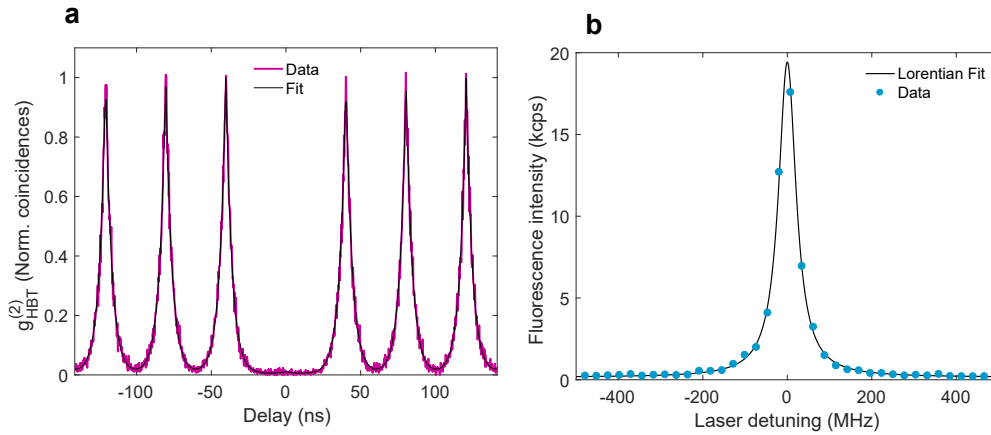


Fig. 3.5 Pulsed Excitation of DBT: **a)**HBT under pulsed excitation (80MHz) **b)** Excitation spectroscopy: Scanning the frequency of a resonant laser across the ZPL and measuring the resulting fluorescence intensity in the PSB. A Lorentzian fit is applied to the data, resulting in a Full Width at Half Maximum (FWHM) value of 55.1 ± 0.5 MHz.

3.4.2 Hong-Ou-Mandel experiment

In this experiment HOM is performed under both CW and pulsed operation. The Fig. 3.6a shows a prominent non-classical interference effect under CW operation and at zero time

delay. The dataset for parallel polarization is significantly lower than the one for photons with distinguishable polarization, i.e., orthogonal. Additionally, two dips can be seen away from the main one, which correspond to the suppressed probability of having two photons closer than the emitter lifetime. Indeed, the dips corresponds to the delay between the paths meaning that one of the four combination for two photons to till the detector implies they entered the interferometer at the same time. This occurs when one photon is transmitted or reflected while the other is reflected or transmitted. For CW case the measurement can be fitted with the following equation (derived from Ref. [190])

$$g_{HOM}^{(2)}(\tau) = 2|r|^2|t|^2g(\tau) + [|t|^4g(\tau - \Delta t) + |r|^4g(\tau + \Delta t)] \times (1 - Ve^{-|\tau|/|\tau_{||}|}) \quad (3.3)$$

In the equation 3.3 $g(t)$ means $g_{HBT}^{(2)}(t)$. First for the case of distinguishable photons (orthogonal case) we deduce $\Delta t = 40.3 \pm 0.2$ ns which is due to the 8m long fiber introduced in one of the interferometer paths. The beam splitter used before the detectors is a non-pol. 50/50 ($|r|^2 = |t|^2$) splitter, but still it has unbalance between reflectance and transmittance which is evaluated using laser light at 783.5 nm. The reflectance $|r|^2$ is 0.50 ± 0.01 and transmittance $|t|^2$ is 0.44 ± 0.01 with over all loses of BS and fiber connection of 0.06 ± 0.01 . The degree of coherence is calculated using all these parameters from independent measurements. The degree of coherence of molecule emission refers to the degree of coherence within each single-photon wave packet. In other words, it describes how well the wave packets can interfere. The following equation, defined as HOM visibility which corresponds to the first order auto-correlation function at zero delay, is used to evaluate the degree of coherence.

$$\left|g^{(1)}(0)\right|^2 = \frac{g_{\perp}^{(2)}(0) - g_{\parallel}^{(2)}(0)}{g_{\perp}^{(2)}(0)} \quad (3.4)$$

The best fit to the data of equation 3.4, gives HOM visibility of 0.89 ± 0.06 . The estimation of the first-order auto-correlation function also estimated from the second-order auto-correlation function measured in a Hanbury-Brown and Twiss (HBT) configuration using the following equation.

$$\left|g^{(1)}(0)\right|^2 = 1 - 2g_{HBT}^{(2)}(0) \quad (3.5)$$

The degree of coherence obtained in equation 3.4 is consistent with the estimation of 0.94 ± 0.04 from equation 3.5. One important aspect of this analysis to be noted is that actually the visibility obtained for CW HOM experiment (that is the value of the dip) corresponds to the interference attainable after temporal post selection on the photon arrival time of the order of

the histogram temporal resolution. This expression is useful to determine for the given system the maximum achievable HOM visibility as it is valid in the limit of negligible dephasing i.e. perfectly coherent wave packets. When severe post-selection is applied, suppressed coincidences at zero time delay are still expected also in the case the sources are detuned or there is dephasing with spectral fluctuations smaller than the overall setup temporal resolution. Any non-perfect visibility can be attributed solely to two main factors - detector time-jitter or mismatch between the spatial modes of the two photon stream. In order to clearly determine the degree of the coherence of the whole photon wave packet, pulsed operation is required, and this will be the argument of the next section. However, the Hong-Ou-Mandel (HOM) interference profile for CW operation still provides useful information regarding the indistinguishability of the photon stream. The minimum of the dip is associated with

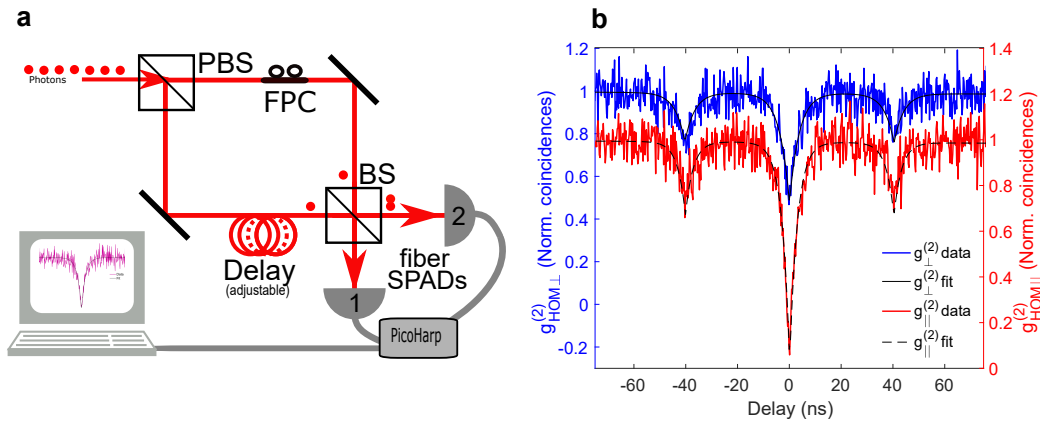


Fig. 3.6 Hong-ou-Mandel experiment: **a)** HOM optical Setup **b)** HOM under CW Operation: A histogram of the relative photon arrival times is shown for parallel (red) and orthogonal (blue) polarizations, with a shifted y-axis scale for clarity. The solid and dashed lines represent fits to the data using expression 3.3

the suppression of multi-photon emission events and other technical aspects. However, the characteristic time of the exponential profile is dependent on the coherence of the emission. Therefore, by analyzing the shape of the HOM interference profile, it is possible to gain insights into the degree of coherence of the emitted photons. It should be noted that although the HOM interference effect is often used as a measure of photon indistinguishability, it is not a perfect metric. Other factors, such as spectral distinguishability or frequency correlation, can also affect the visibility value[191, 192]. However, the HOM effect remains a useful tool for characterizing the coherence properties of the emitted photon stream. For the molecule represented in the Fig. 3.3 and 3.6, the time scale of the dip for parallel configuration is shorter (2.7 ± 0.2 ns) than that for orthogonal (3.6 ± 0.2 ns) and HBT ones (3.5 ± 0.2 ns). This estimation of the coherence time ($\tau_c = 2\tau_{\parallel} = 5.4 \pm 0.5$ ns) is in agreement with the

FWHM linewidth measurement obtained from the molecule excitation spectrum (reported in Fig. 3.5b). Indeed, in the latter case we read ($FWHM = 55.1 \pm 0.5 \text{ MHz}$), while from the HOM interference time scale we can estimate ($FWHM = 1/(2\pi\tau_c) = 51.3 \pm 4 \text{ MHz}$). In order to obtain a precise estimation of the interference ability of the emitted photon wave packets, pulsed laser is employed. Indeed this methodology allows the investigation of isolated wave packets giving access to the trend of the coherence throughout the whole envelope.

3.4.3 Life-time and TPI Visibility Evaluation

As already shown in addition to the histogram of relative photon arrival times, pulsed operation allows an independent measurement of the excited state lifetime. This is obtained building the histogram of the fluorescence photon arrival time with respect to the laser pulses. subsequently measuring the fluorescence lifetime. A typical dataset is shown in in Fig. 3.7(b). As a general approach, with the aim of maximizing the knowledge on the investigated emitter, pulsed operation is studied on molecule after characterization under CW operation. In this line, the measurements reported in the Fig. 3.4, 3.5, 3.6, 3.7 and 4.8 refer to the same molecule, whose performances are within the reach routinely after the selection of good emitters. Focusing first on lifetime of $4.01 \pm 0.01 \text{ ns}$ is determined to be the best fit with a single exponential decay with uncertainty calculated as standard deviation over 10 measurements like the represented Fig. 3.5(b). The discrepancy between this timescale and the 3.5 ns obtained for anti-bunching profiles under CW operation can be explained by the fact that τ_{HBT} is affected by both the excited state lifetime and pumping rate. The normalized results for pulsed excitation are presented in the Fig. 3.7a) shows instead the histogram of the relative arrival time in case of HOM experiment. Red and blue solid lines, results for parallel and orthogonal polarization are reported respectively. The two data sets are represented by 15 ns for the sake of clarity. The peak amplitude for normalization is calculated by averaging over more than ten pulses, excluding those occurring at zero and $\pm\Delta t$ delay. The visibility of Two-Photon Interference (TPI) can be assessed by comparing the peak area around zero delay between indistinguishable and distinguishable photons. This comparison can be quantified using the following equation:

$$V = \frac{A_{\perp} - A_{\parallel}}{A_{\perp}} \quad (3.6)$$

where A_{\perp} and A_{\parallel} can be calculated as the sum over the histogram lines corresponding to the central peak for the two cases. By integrating over a time window of 26 ns, which corresponds to roughly 96% of the photon wave packet area, we were able to estimate a

visibility value of $V = 78\% \pm 4\%$. Investigating the interference of photon wave packets involves carefully controlling the timing between the packets. To further analyze these results, we used a model based on Ref.[193], which is extrapolated for a train of infinite pulses. This model introduced a phenomenological parameter, denoted as " ν ", that accounts for factors such as imperfect spatial alignment and polarization control, residual multiphoton probability, and the emission of distinguishable photons within the filtered range but outside the ZPL. This parameter represents the visibility value that would be obtained in the limit of negligible dephasing. In order to reduce the number of free parameters in the model the factors $|r|^2$

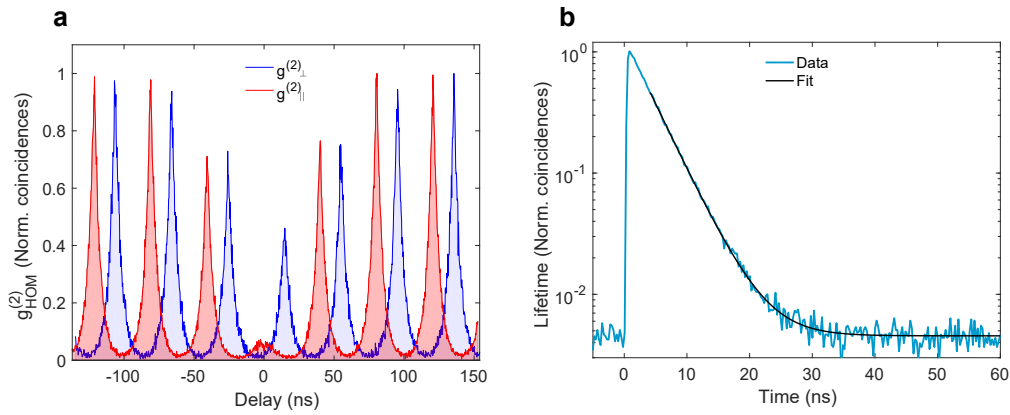


Fig. 3.7 Hong-ou-Mandel:**a**) HOM under Pulsed Operation: A histogram of the relative photon arrival times is shown for parallel (red) and orthogonal (blue) polarizations, with a shifted y-axis scale for clarity. The solid and dashed lines represent fits to the data using expression 3.3. To obtain the results shown in panels (c) and (d), the integrated count rates for 100 kilo-counts per second (kcps) were collected on each Single Photon Avalanche Diode (SPAD) for a duration of 10 minutes. The normalization level corresponds to around 250 coincidences with a binning size of 256 ps. **b**)

and $|t|^2$ of the second beam splitter, the temporal resolution of the electronic system (230 ps), and the delay corresponding to the inverse of the laser's nominal repetition rate (24.79 MHz) are determined independently and kept fixed for this analysis. The model has hence only three free parameters: the excited state lifetime τ_1 , the pure dephasing Γ^* , and ν . Using a least squares fitting algorithm, we obtain the following parameter values: $\tau_1 = 4.046 \pm 0.02$ ns, $\Gamma^* = 55 \pm 10$ MHz, and $\nu = 0.956 \pm 0.02$. These values allow for an independent estimation of the linewidth, which follows as:

$$FWHM = \frac{\Gamma}{\pi} = \frac{1}{2\pi\tau_1} + \frac{\Gamma^*}{\pi} \quad (3.7)$$

which gives a value of 55 ± 4 MHz and it is in substantial agreement with the direct measurement reported in Fig. 3.5b). The factor ν plays a crucial role in understanding the

achievable maximum visibility in the system. Interestingly, this factor represents the visibility that could be achieved by further cooling the system to 1.4 K, where pure dephasing should be completely suppressed. This highlights the importance of understanding why the value of v is less than 1. On the one hand, the experimenter may introduce errors in setting the relative polarization between the two arms, leading to additional distinguishability due to non-perfectly parallel states. The control on the polarization setting is estimated to hold an uncertainty around 1/1600. Moreover, the single-photon Fock state may not be perfectly pure, which is evident from the measurement of the $g_{HBT}^2(\tau)$ in the HBT. This measurement yields $g_{HBT}^2(0)$ value of $A0/AN = 0.0086 \pm 0.0008$, indicating the not-perfect purity of the single-photon Fock state. Using this information and assuming full distinguishability for the non single photon component of the input state[194], the mean wave packet overlap of the single-photon component can be estimated as $M_S = \frac{v+1}{4RT(1-g(2)(0))}$. Under the assumption of negligible dephasing, this estimate yields value of approximately 97% for the mean wave packet overlap of the single photon component. However, this value is affected by the filtering efficiency and the presence of a residual component of distinguishable photons ($1-\alpha$), given by the portion of the emission in the PSB leaking through the notch filter. The fluorescence spectrum measured before and after the filter suggests that roughly 98% of the light overlaps with the ZPL. In the optimal condition of zero dephasing but with the same filtering window, the expected maximum visibility would be degraded to a maximum of α^2 . Therefore, one can expect a visibility of 96% under optimal conditions, which is consistent with the estimated value.

3.4.4 Temporal and Spatial stability of TPI

In order for the HOM interference to occur, the two photons have to be exactly in the same state, included temporal localization. This means that the delay between the two paths of the MZI has to carefully match the temporal separation between the selected emission events. In our setup, this can be conveniently obtained operating on the adjustable repetition rate of the pulsed laser source, which effectively changes the delay between the packets. The resulting data are then used to plot the HOM visibility versus relative delay, as shown in Fig. 3.8(a) along with the theoretical curve. In particular, for the given 8m fiber length difference, the best matching (obtained as the delay for which highest HOM visibility is obtained) occurs for a repetition rate of 24.79 MHz. However, estimating the delay line introduces some uncertainty, which is found to contribute the most to the uncertainty in visibility, with an error of around 4%. In the perspective of quantum technology applications an important aspect is the robustness of the TPI, both in terms of temporal distance between the emission of the two interfering photons and in terms of fluorescence cycles separating them. The

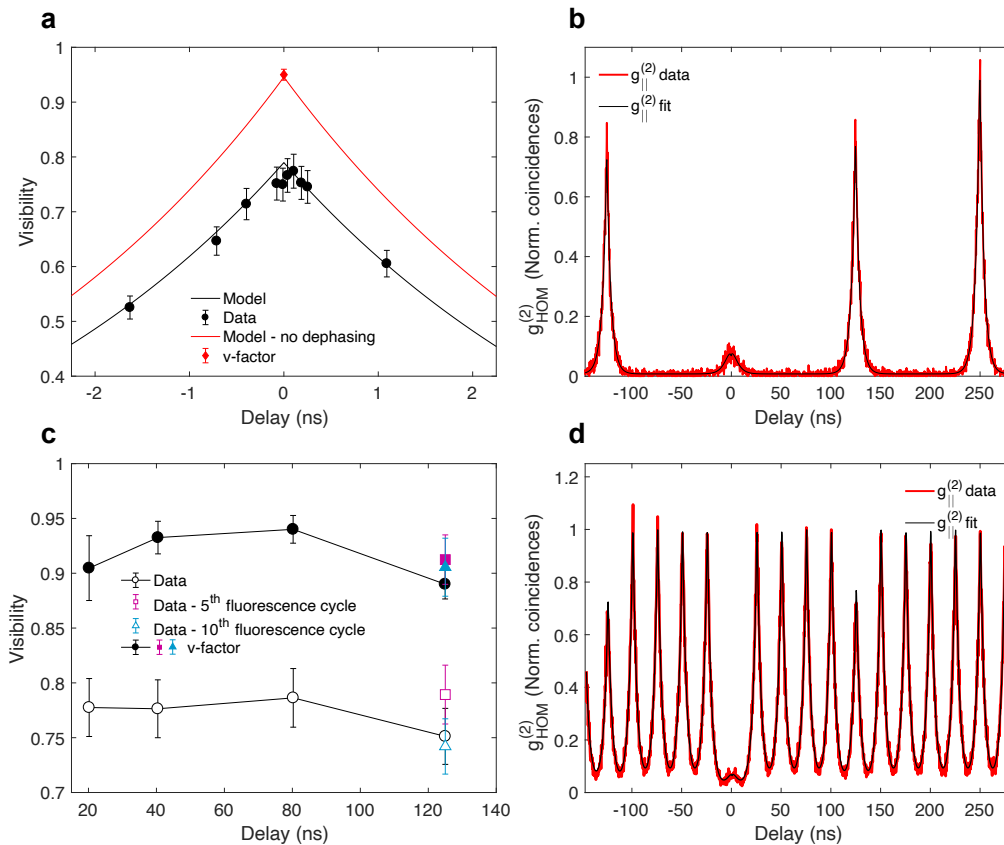


Fig. 3.8 Temporal and spatial stability of TPI: **a)** The visibility and v-factor vary with the laser repetition rate, as the delay is determined by adjusting the repetition rate to achieve temporal overlap between the photon wave packets. **b)** The coincidence histogram for a delay line with a length of 25 meters and a delay of 125 ns, with parallel polarization. **c)** This graph shows the optimal HOM visibility and v-factor as a function of delay line length. The colored dots indicate the visibility of the interference between photons separated by multiple fluorescence cycles, specifically for the longest delay of 125 ns. **d)** The coincidences showing the interference between photons separated by five fluorescence cycles, obtained with a 15 ns-long delay line and parallel polarization, using a laser repetition rate of 40 MHz

$g_{HOM}^2(\tau)$ using parallel polarizations is reported for a delay of 125.0 ± 0.2 ns (around 25 m) in Fig. 3.8(b). Interestingly, the visibility only begins to decrease at this time delay, which corresponds to about 30 times the photon wave packet extension. Moreover, It is noteworthy that no significant drop in TPI is observed even between photons separated by up to 10 fluorescence cycles, as reported in the visibility graph in Fig. 3.8(c). To illustrate this, Fig. 3.8(d) shows the coincidences histogram for the interference between photons separated by five fluorescence cycles, where the same delay Δt of 125 ns as in the Fig. 3.8(b) is employed with a laser repetition rate of 40 MHz. This remarkable spectral stability is in agreement with the negligible spectral diffusion reported for continuous wave operation in this study and in literature.

3.5 Conclusion

This experiment demonstrates the triggered generation of highly indistinguishable single photons from a single organic dye molecule in a cryogenic experiment (3k) under non-resonant pulsed excitation. This is achieved without the aid of any photonic resonance and using only a 0.4nm-wide spectral filter to select the emission. The emitters are located in a sub-micrometric environment, and a HOM interference visibility of over 78% is reported, limited only by the residual dephasing present at the operating temperature of 3 K. Interestingly, a visibility of 96% is expected for the same experiment at 1.5 Kelvin operation. Moreover, the remarkable spectral stability demonstrated in this experiment, where the HOM visibility remains largely unaffected even for photons separated by up to 125 ns (which is equivalent to 30 times the wave packet duration) and by up to 10 fluorescence cycles, holds promising potential for the practical implementation in quantum technologies. The utilization of multiple photons is crucial for linear optical quantum computing, where the temporal demultiplexing technique is commonly employed to increase the number of available resources. Hence, the stable and predictable behavior of the HOM visibility observed in this experiment represents a significant step forward in the quest for reliable and efficient quantum computing. However, the brightness of the source at detector is currently limited to around 2%, corresponding to a brightness at the first lens (N.A. 0.67) of around 5%. Therefore, the integration of the emitter with photonic devices becomes essential for implementation in quantum applications. Employing photonic resonance can modify both the radiation pattern and spectral distribution of the emission, thereby enhancing the source brightness to the state-of-the-art level. Recent studies have demonstrated the potential of this type of system to be seamlessly integrated into hybrid photonic structures.

Chapter 4

Room Temperature Quantum Key Distribution with molecular emitters

Here, we employ the molecular emitters characterized in the previous chapter as triggered single-photon sources operating at room temperature for quantum key distribution (QKD) experiments. We implement a test-bed QKD setup to demonstrate a BB84 protocol based on polarization encoding of the single-photon states generated by the molecule, in a free-space laboratory link. After a preliminary characterization of the molecular single-photon source efficiency and of the quantum bit error rate (QBER), we estimate the associated secret key rate (SKR) and compare it to the performances of weak coherent pulses, with and without decoy. Finally, we evaluate the achievable maximum secret key rate upon the optimization of the optical setup and of the photonic configuration of the sample.

4.1 Introduction

As introduced in Chapter 2, QKD is a cryptographic technology that exploits the principles of quantum mechanics to enable secure key exchange between two or more parties. Quantum key distribution (QKD) is considered the most advanced technology in the field of quantum communication, and a fundamental step towards realizing the quantum internet[195, 196, 158]. However, despite the presence of a few companies and startups operating in the global market, several factors are currently hindering the full adoption of the QKD technology. These can be divided in four different categories: the maximum link distance[197–199], the amount of key generation[200, 201], the coexistence of quantum signals with classical communication channels [201, 202] and the security parameters of the implemented QKD systems[158]. In fact, current QKD systems (considering only discrete variable systems) are

mainly based on so-called weak coherent pulses (WCP), where a coherent quantum state is prepared with a strongly attenuated laser approaching the single-photon regime to emulate quantized light emission. Since multi-photon events in coherent states are still possible, WCP-based QKD protocols involve a significant possibility of information leakage to an eavesdropper. To mitigate this risk, one solution that has gained traction in the quantum communication community is the use of decoy states, i.e., a random change of the laser intensity over time[35, 171]. Although the decoy state method is well-established and widespread, owing to the complexity of the protocol implementation and the consequent possibility of errors, the technique is not immune to security threats through the opening back doors in the quantum communication system[203]. An alternative solution to weak coherent pulses consists in using high purity SPS, which can provide several advantages in terms of both secret key rate (SKR) and security. This is due to the extremely low probability of multi-photon events associated to deterministic SPS, as they are based on spontaneous emission processes.

Despite the great advancements achieved by SPSs in the solid-state, the application to quantum communication remains barely unexplored, with only few experiments showing the ability to generate quantum keys by exploiting a deterministic SPS. The examples in the literature involve quantum dots [42, 43, 204, 64, 44, 41, 45, 50, 48, 49, 47, 46], transition metal dichalcogenides (TMDCs)[52] and color centers in diamond[205], where promising results were obtained in terms of key generation rates as compared to standard QKD systems. The interest in the field is also confirmed by recent theoretical studies which explore the advantage of non-standard excitation schemes for enhanced quantum cryptography performances [206]. However, the systems used in most of the above mentioned experimental QKD demonstrations need cryogenic temperatures, which involve high costs and limited portability. It is hence worth highlighting the experiments employing single-photon sources working at room temperature[205, 207, 55], all exhibiting emission in the red or near-infrared band. Among these demonstrations, we point out Zeng et al. [207], who have achieved the most promising results in terms of secret key rate and link-budget up to about 29dB, exploiting a passive transmitter source based on hexagonal boron nitride (hBN), and Leifgen et al. [205], only authors to have implemented a real-time polarization-encoding technique, achieving an overall link-budget of about 15dB.

In this context, we have tested the performances of DBT:Ac nanocrystals (NCX) as a triggered SPS for QKD experiments at room temperature. In particular, we have demonstrated the feasibility of a BB84 protocol in a free-space laboratory link by implementing polarization encoding of the single-photon states generated by a single molecule under pulsed

laser excitation. As described in Chapter 3, DBT:Ac NCX at cryogenic temperature excellent photophysical properties as quantum light sources, emitting bright, pure and highly indistinguishable photons[58] (a characteristic which also opens up possibilities for implementing more complex quantum communication protocols[208] and linear optic processing[209]. Furthermore, molecular single-photon sources can be integrated into hybrid photonic structures with almost 100% collection efficiency[210, 211], offering an attractive alternative to conventional quantum emitters, which suffer from low collection efficiency. Most importantly, molecules can be operated also at room-temperature operation[212, 60, 37, 103], and DBT:Ac NCX have shown to preserve excellent emission properties (brightness and purity) despite the nanostructured environment.

The results of our experiment, in terms of source efficiency and SKR, are better or at least competitive with state-of-the-art experiments conducted at cryogenic or room temperatures[213, 43, 204, 205, 207]. Most importantly, our approach has the added advantage of operating at room temperature with great photostability, and of involving an easy, fast and cost-effective sample fabrication, all relevant benefits to the practical implementation of SPS-based quantum communication systems[40, 214, 215], especially for the installation in satellite quantum-encrypted networks. Finally, we also provide a comprehensive evaluation of the attainable secret key rate (SKR) upon the realistic optimization of the optical setup, of the nano-photonic configuration and of the integrated molecular emitter. The results indicate competitive SKR even against protocols utilizing decoy states. Considering the maximum expected SKR of 0.5 Mbps, extrapolated from the experimental measurements, and the room for further improvements, this technology has the potential to significantly enhance the deployment of single-photon sources for QKD applications, as well as for other quantum communication protocols.

4.2 Optimization of Sample Fabrication

In the context of QKD applications, the optimization of the collection efficiency is especially important since it directly impacts on the overall source efficiency and hence on the final SKR. In this sense, a crucial preliminary part of the work presented in this chapter was aimed at identifying an optimal photonic configuration in terms of both ease of fabrication and attained collection efficiency. We hence investigated several planar geometries inspired by the successful results previously obtained by the group and published in Checcucci et al [216].

In particular, we consider three different planar geometries where molecules are embedded in, for which we compare both the simulated collection efficiency and experimental

results. The simulations are run with a Matlab code optimized in the Ref. [216], which consists in semi-analytical calculations based on Fresnel laws to calculate the k-vector components of the emitted field after transmission and reflection at the interfaces of a planar multilayer structure. The DBT:Ac NCX emitter, is modelled as an Hertzian dipole parallel to the substrate interface and embedded in the middle point of a homogeneous anthracene (Ac) layer of 100nm thickness. From the work in Checchucci The three investigated configurations are sketched in Fig. 4.1 a,b,c:

a: The active layer (DBT:Ac) is deposited on a glass coverslip (thickness = 0.15 mm) and is protected by a spin-coated polyvinyl alcohol (PVA) layer, which is finally sputter-coated with a thin gold film (150 nm -thick). The sample is used in combination with an oil objective lens (from the glass substrate side), as shown in Fig. 4.1a.

b: In the Fig. 4.1b, The glass coverslip is firstly coated with film film of gold (same thickness), where the active layer is deposited, and finally covered with the spin-coated PVA layer on top.

c: In the Fig. 4.1c, the same configuration of Fig. 4.1b is utilized in combination with an air objective lens.

In the Fig. 4.2a),b), the simulated collection efficiency and the radiation patterns are computed for the configurations used with the oil objective ('Oil') and the air objective ('Air'), respectively. The three configurations sketched in the Fig. 4.1, from the point of view of simulations can indeed be grouped in these two sub-classes if we consider that the refractive indexes of PVA and Ac are approximately the same (refractive index 1.6). In all results we show the power density normalized by the maximum value obtained in the case where the dipole is placed in a homogeneous medium of Ac. In particular, for collection efficiency we consider the integration over the azimuthal angle and show the results for polar angles within the range $[0,90]$, since, experimentally, the objective lens collects only the mission radiated towards the upper hemisphere. For the radiation patterns, two vertical phi-cut planes, namely $\phi = 90$ and $\phi = 0$. We conclude from the simulated results, that despite the Air configuration seems more suitable for coupling into a single mode fiber (the two azimuthal cuts coincide in Fig. 4.2b), giving evidence of a more Gaussian beam), the Oil configuration brings the best advantage in terms of collection efficiency. For the numerical aperture of the employed oil objective ($NA=1.4$), corresponding to a semi-collection angle of about 67 degrees, a collection efficiency of about 80% is achieved.

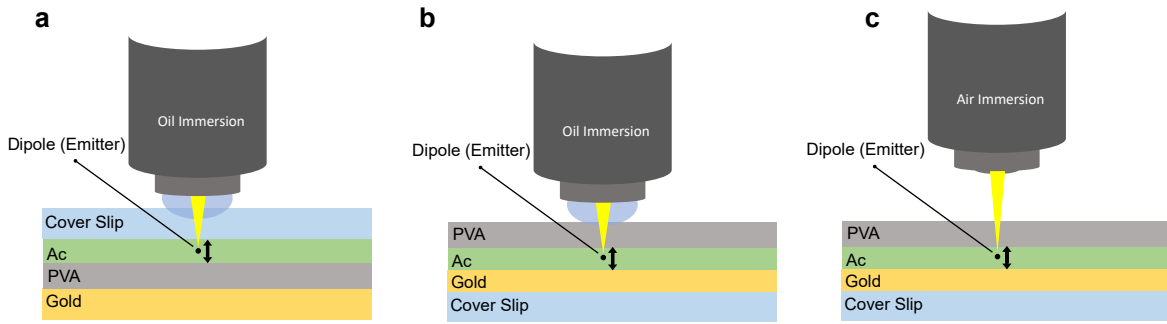


Fig. 4.1 **Optimization of Sample Fabrication:** Three investigated configurations of sample fabrication, used in combination with an oil immersion lens (a) and b)) and with an air objective (c).

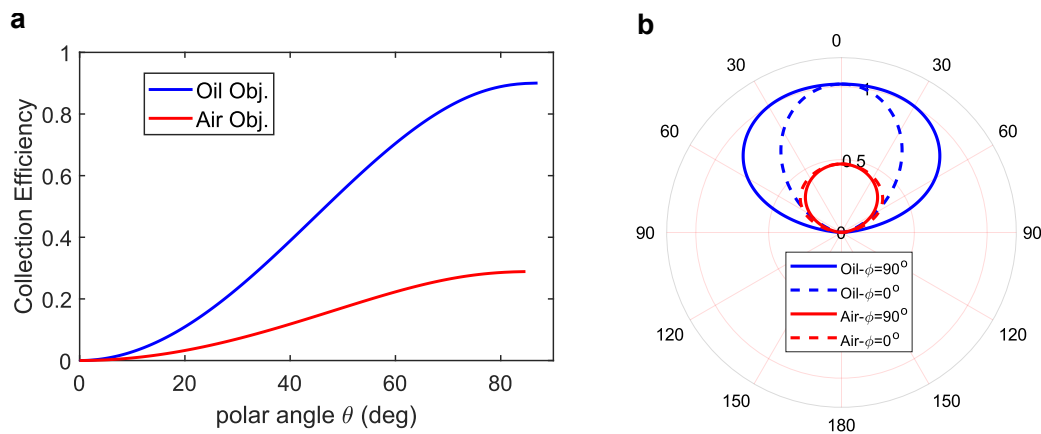


Fig. 4.2 **Simulations:** Comparison between the configurations used in combination with an oil-immersion objective and with an oil objective, respectively. **a)** Collection efficiency as a function of the polar collection angle. **b)** Radiation pattern on two phi-cut planes. For both figures the the results are normalized to emission in a homogeneous anthracene medium.

Experimentally, the configuration depicted in Fig. 4.1b resulted disadvantageous since the PVA layer dissolves in about one hour when in contact with the oil, being detrimental for the DBT emission properties. In conclusion, we chose the configuration in Fig. 4.1a (also shown in the zoom-in of the experimental setup diagram in Fig. 4.3), which gave proof of stability for several weeks of continuous measurements. The overall photonic scheme offers the advantage of a robust and planar geometry obtained with a straightforward fabrication method which, which in combination with an oil-immersion objective allows for enhanced collection efficiency. The full fabrication process is limited to the use of thin-film deposition and metal coating technology, resulting in a sample preparation time of approximately one hour.

4.3 Test-bed Setup for Room-Temperature QKD

The custom-made optical setup used in this work was optimized targeting compactness, optical stability and minimization of losses in the detection optical path. The concept scheme is shown in Figure 4.3. The setup is divided into three main parts, namely the source, the transmitter (Alice), and the receiver (Bob) sections.

The Source: DBT:Ac nanocrystals are integrated in the planar photonic geometry described in the previous section. The sample is carefully positioned on a sample holder which lays on the top of a custom-made epifluorescence confocal microscope. This is based on a 100x oil objective (numerical aperture 1.4) and on a pivot element (beam-splitter 70:30 - transmission:reflection), which, in combination to a long-pass filter in detection, allows to efficiently separate the fluorescence emission from the laser excitation. This latter, consists on a pulsed laser (PicoQuant) conveying 50-picosecond long pulses at 766 nm with variable repetition rate, also switchable to the CW mode. In this particular experiment, the excitation laser serves a dual purpose, also functioning as a WCP source for the comparison of the performances of triggered single-photon source with the decoy state method. The accurate manipulation of the sample is enabled by a 3D positioning stage connected to a piezo servo controller (Model: PI Physik E501), which is combined to a manual 3D stage for coarse exploration of the sample. In order to select the optimal DBT:Ac nanocrystals for the experiment, the sample is preliminarily observed under wide-field illumination by using an Electron Multiplying Charge-Coupled Device (EMCCD) camera (Model: iXon 897). During this step, isolated nanocrystals with the highest fluorescence intensity are selected for a more thorough analysis under confocal excitation. Hence, the laser polarization is matched to the molecular dipole (which is generally parallel to the substrate plane[217]) for optimal excitation, and the fluorescence emission is characterized in terms of brightness and purity via the saturation curve measurement and the second-order correlation function (see next section).

The Transmitter (Alice): At the Alice station, after the fluorescence signal is separated from the pump through the long-pass filter, an achromatic half-wave plate and a quarter-wave plate are employed for the preparation of the quantum state, which is encoded in the polarization of each single-photon pulse. In this proof-of-concept demonstration, the wave-plates are manually rotated to switch among the horizontal (H), vertical (V), diagonal (D), and anti-diagonal (A) polarizations, in order to realize a four-state BB84 QKD protocol. A set of neutral density optical filters are used to control the photon flux and emulate lossy channel conditions that would be encountered in real-world QKD scenarios. By adjusting the overall filter attenuation, optical loss over a broad dB range can be simulated and tested, thus mimicking the transmission at long distances. This aspect is crucial for the assessment

of the performance of the SPS for QKD applications.

The Receiver (Bob): At the Bob station, the photons are analyzed with a passive choice of measurement basis, where the received photons are split using a beam splitter (BS). The photons that are reflected by the beam splitter are directed into a free-space channel, where a combination of a half-wave plate, a polarizing beam-splitter, and a free-space Single-Photon Avalanche Detector (SPAD, D1) is used for the discrimination between $|D\rangle$ and $|A\rangle$ states. The half-wave plate is manually rotated to switch the detection between the two states. The transmission of the beam splitter is instead coupled to a single-mode fiber polarizing beam-splitter (PBS), where fiber polarization controls (PC) are optimized to discriminate between state $|H\rangle$ and $|V\rangle$ at either of the fiber SPADs connected to the outputs, D2 and D3, respectively. The fiber setup is also used in a Hanbury-Brown-and-Twiss (HBT) configuration for the measurement of the second-order correlation function during the preliminary SPS characterization. Finally, the detected photon counts and arrival times in the four channels are recorded via a multi-port time-tagging system. This setup allows for the accurate measurement of the polarization state of the photons received by Bob, which is then compared with the polarization state sent by Alice to determine the security of the transmitted information.

4.4 Characterization of Single-Photon Emission at Room Temperature

To assess the performance of the DBT SPS, we characterize the fluorescence emission in terms of multi-photon probability and collected photon rate, by analyzing the second-order correlation function $g^{(2)}(\tau)$ and the collected photon flux as a function of pump power, respectively. This is repeated for different molecules to collect a meaningful statistics associated to the molecular SPS in the planar geometry considered in this experiment. The results are presented in Fig. 4.4.

Purity

Panel (a) shows the normalized histogram of the inter-photon arrival times, which approximates $g^{(2)}(\tau)$ for small time delays, for the photon streams collected at D2 and D3 in the HBT configuration, under excitation pulses at a repetition rate of 80 MHz. The suppressed peak at zero-time delay provides compelling evidence of the extremely low multi-photon

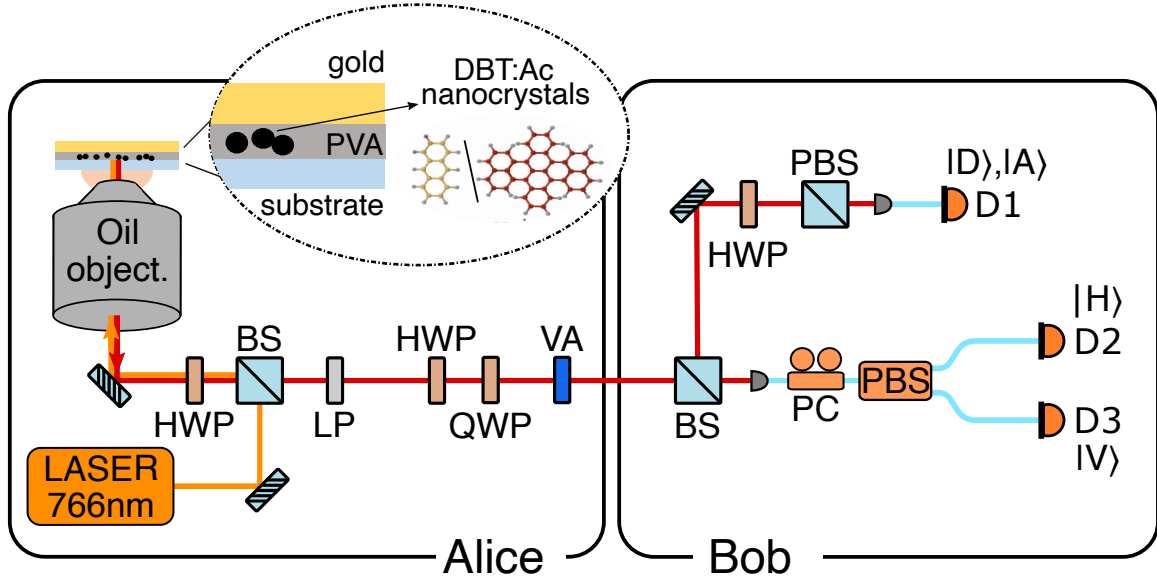


Fig. 4.3 **Experimental test-bed for room temperature QKD:** **Alice)** Single dibenzoterrylene molecules embedded in anthracene nanocrystals (DBT:Ac) are integrated in a planar multi-layer photonic structure for collection enhancement (**zoom-in**). An epifluorescence confocal microscope with oil-immersion objective is used to trigger and collect the emission of single-photon packets with 50-picosecond long laser pulses at 766 nm and 80 MHz repetition rate. The pump laser is filtered-out with a long-pass filter (LP), four quantum states are encoded in the single-photon polarization ($|H\rangle$, $|V\rangle$, $|D\rangle$ and $|A\rangle$) by means of a half-wave (HWP) and a quarter-wave plate (QWP). Variable attenuators (VA) emulate channel losses. **Bob)** At the reflection of a beam splitter (BS), a HWP and a polarizing beam splitter (PBS) are used to discriminate between $|D\rangle$ and $|A\rangle$ at the free SPAD D1. At the BS-transmission port, photons are fiber-coupled and a fiber polarization control (PC) is optimized to route the $|H\rangle$ and $|V\rangle$ states at the two outputs of a fiber PBS, respectively connected to fiber SPADS D2 and D3.

emission probability. Considering the expression below:

$$g^{(2)}(\tau) = g^{(2)}(0) \exp(-|\tau|/\tau_c) + \sum_n \exp(-|\tau + nT|/\tau_c) \quad (4.1)$$

where the n -index runs on the order number of the lateral peaks, τ_c is the dip characteristic time and T the laser repetition period, we retrieve from the best fit to the data $\tau_c = (3.6 \pm 0.1)$ ns. For a more precise evaluation of the single-photon emission purity we fit the data measured for the same molecule at half of the laser repetition rate (see inset of Fig. 4.4(a)) where the suppressed peak can be clearly distinguished, and we obtain $g^{(2)}(0) = 0.02 \pm 0.01$. This result is compatible with the characterization of the nanocrystal

source reported in ref. [88].

Saturation Curve

Considering only Bob's side in Fig. 4.3, the overall collected single-photon rate is measured at D1 by summing the contributions from states $|D\rangle$ and $|A\rangle$ and accounting for the BS reflection and for the losses of Bob free space channel, namely the optics $\eta_{opt,B} \sim 80\%$ and detector efficiency $\eta_{det} = (30 \pm 2)\%$. Owing to the broad molecule's emission spectrum at room temperature (~ 50 nm), η_{det} is experimentally estimated by calibration against power-meter measurements for different laser wavelengths and calculating the weighted average, based on the spectral-intensity distribution. Bob's efficiency is then given by the product $\eta_{Bob} = \eta_{opt,B} \cdot \eta_{det}$. A typical result for the collected photon rate as a function of laser power is shown in Fig. 4.4(b). The experimental data follow a characteristic saturation behaviour, which is well described by the equation 1.11 given in the Chapter 1.5.3. In particular, the operational pump power (P) employed for the QKD experiments corresponds to a saturation parameter $s = P/p_s \sim 2$, i.e. is twice the saturation power. In practice, this is chosen during the preliminary characterization phase in order to optimize the combination of the resulting single-photon purity, quantum bit error rate and source efficiency, and is kept constant along the QKD experiment. The resulting mean photon number is obtained by dividing the corresponding collection rate by the laser repetition rate, which for the case of the saturation curve in Fig. 4.4(b) yields $\mu_{mol} = 0.08 \pm 0.01$ and is among the best values reported for solid-state single-photon sources for QKD [213, 205, 204]. The maximum collected count rate instead yields $R_\infty = (10 \pm 2)$ Mcps. Repeating the procedure on 16 molecules in different nanocrystals leads to the distribution displayed in the inset of Fig. 4.4(b). The inherent variability is likely due to different factors, such as the different local crystalline environment at the molecular dipole position (i.e. different distance to the nanocrystal surface and interface effects), as well as the distance to the gold film (see inset of Fig. 4.3, which provides optimal enhancement for a value of ~ 100 nm (see also the Discussion section).

4.5 Result and Analysis

The previously characterized single-photon pulses are employed as polarization-encoded qubits in a four-state BB84 QKD protocol for the key generation.

In this proof-of-concept QKD demonstration, the polarization encoding of the generated single-photon qubits is prepared manually. The preparation of the four polarization states $|H\rangle$, $|V\rangle$, $|D\rangle$, and $|A\rangle$ is detailed in the following, and is based on the manual manipulation

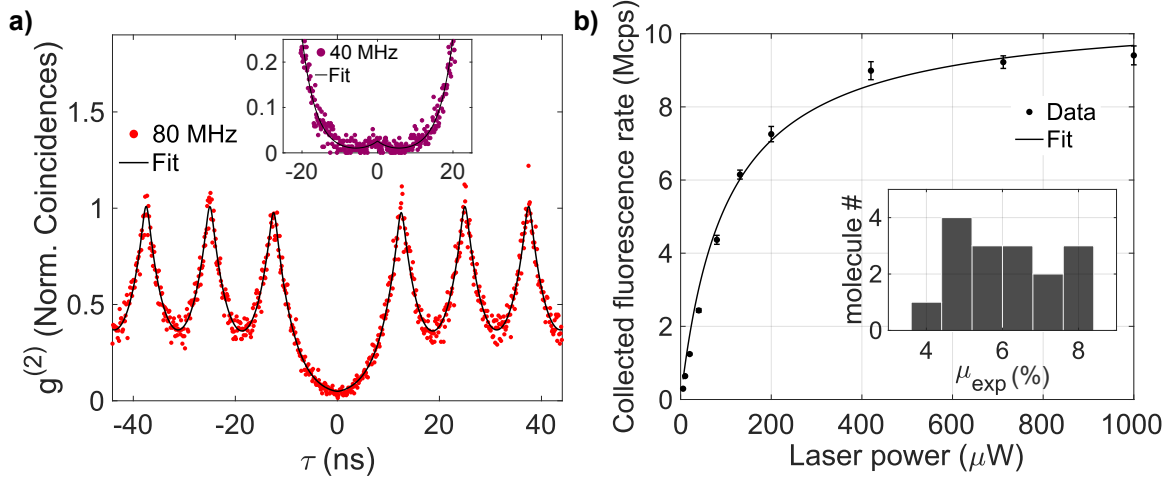


Fig. 4.4 **Characterization of single-photon emission:** **a)** Normalized histogram of photon coincidences measured in a HBT configuration under 80 MHz repetition rate (red dots) and fit to the data (solid black line) for the second-order correlation function $g^{(2)}(\tau)$. **inset** Zoom-in of the central suppressed peak for data measured under 40 MHz repetition rate (purple dots) and associated fit (solid black line). **b)** Collected single-photon rate as a function of laser pump power (black dots) and fitted saturation function (black solid line). Distribution of mean photon number values for 16 molecules in different nanocrystals (**inset**).

of a set of a half (HWP) and a quarter (QWP) wave plate in Alice station. The reading of the states is achieved, in Bob station, via manual setting of the polarization control (PC) in the fiber channel and of the HWP in the free space channel (see Fig. 4.3).

1. First of all, $|H\rangle$ is prepared by acting on the HWP and QWP in Alice station and on the PC in Bob station as to extinct counts on one of the fiber-SPADs (D3). The corresponding values on both plates are marked.
2. State $|H\rangle$ is used to find and mark the zero-angle position of the HWP on the free space channel of the Bob station, by maximizing counts on the free SPAD after the PBS.
3. The $|H\rangle$ state is read on both fiber-SPADs and on the free SPAD, in this latter case both by setting the HWP at zero and rotating by ± 22.5 degrees. Counts shall be maxima in D2 fiber-SPAD and minima in D3, while, in the free SPAD, they shall be maxima with the HWP set at zero, while halved when the HWP is set to ± 22.5 degrees.
4. $|V\rangle$ state is set by rotating by 45 degrees the HWP in Alice station. The reading of the state shall give maxima counts for D3 and minima for D2. In Bob free space channel, counts shall be minima when the HWP is set to zero, while halved when the HWP is set to ± 22.5 degrees.

5. $|D\rangle$ and $|A\rangle$ are prepared by rotating the HWP in Alice station by ± 22.5 , respectively. $|D\rangle$ ($|A\rangle$) is read on the free SPAD by rotating the HWP in Bob station by $+22.5$ (-22.5) degrees from the initial zero angle position, with counts which shall be maxima (they shall be minima for -22.5 ($+22.5$) degrees). For both states preparation, counts shall be evenly split between D2 and D3.



	Half WP		Quarter WP		Half WP (D)		Half WP (D)		QBER(%)	
	WCP	Fluo.	WCP	Fluo.	WCP	Fluo.	WCP	Fluo.	WCP	Fluo.
H	169	163	334	177	210	210	255	255	0.7 ± 0.7	3.8 ± 0.2
V	214	208	334	274	255	255	210	210	0.2 ± 0.3	2.8 ± 0.2
D	236.5	230.5	334	238	210	210	255	255	0.1 ± 0.2	6.8 ± 0.1
AD	191.5	185.5	334	215	255	255	210	210	0.12 ± 0.08	7.2 ± 0.4

Fig. 4.5 Manual States Encoding: To encode information in the four distinct polarization states (H, V, D, and AD), it is necessary to use four different combinations of angles for both WCP and Fluorescence measurements. When changing the state from H to V and D to AD, the difference in angle on the HWP is 45° . For non-orthogonal states (H to D and AD, V to D and AD), the difference in angle is 22.5° .

Following the state preparation of $|H\rangle$, $|V\rangle$, $|D\rangle$, and $|A\rangle$, we evaluated the quantum bit error rate (QBER) for each of the four discrimination channels, as described in the previous section. In Fig. 4.3, the experimental angles set for each waveplate in Alice and Bob station are reported, together with the corresponding QBER. The resulting average $QBER_{mol}$ was found to be $3.4 \pm 0.2\%$ in the back-to-back configuration, with $QBER_H = (3.8 \pm 0.2)\%$, $QBER_V = (2.8 \pm 0.2)\%$, $QBER_D = (6.8 \pm 0.1)\%$ and $QBER_A = (7.2 \pm 0.4)\%$, respectively. In Fig. 4.6(a), the matrix of the normalized counts using single-photon emission in each output channel for a given input channel (equivalent to the outcome distribution for the four set of states) is presented in a 3D colour map for the best case scenario of zero channel losses, corresponding to having no attenuator in Fig. 4.3. In panel (b), we report the state preparation matrix using an attenuated laser (i.e., WCP) with a mean photon number per pulse of $\mu_{WCP} = 0.50 \pm 0.03$. To quantify the fidelity of the states and the transmission effects we resort to the expression of fidelity $F(p, r) = \langle \sum_i (p_i r_i)^{1/2} \rangle$ [218], where p_i and r_i are the experimental and theoretical elements of the probability distribution for each polarization state, and $\langle \cdot \rangle$ stands for the average over the four considered states. We note here, that p_i is obtained from the matrix shown in Fig. 4.6 (experimental outcome distribution) upon normalization (probability distribution). Hence, the fidelity yields, respectively, $(99 \pm 1)\%$ and $(99.78 \pm 0.03)\%$ for the single-photon state and the WCP with $\mu_{WCP} = 0.5$, respectively. This result attests to the robustness of the molecule-based proposed test-bed. To determine

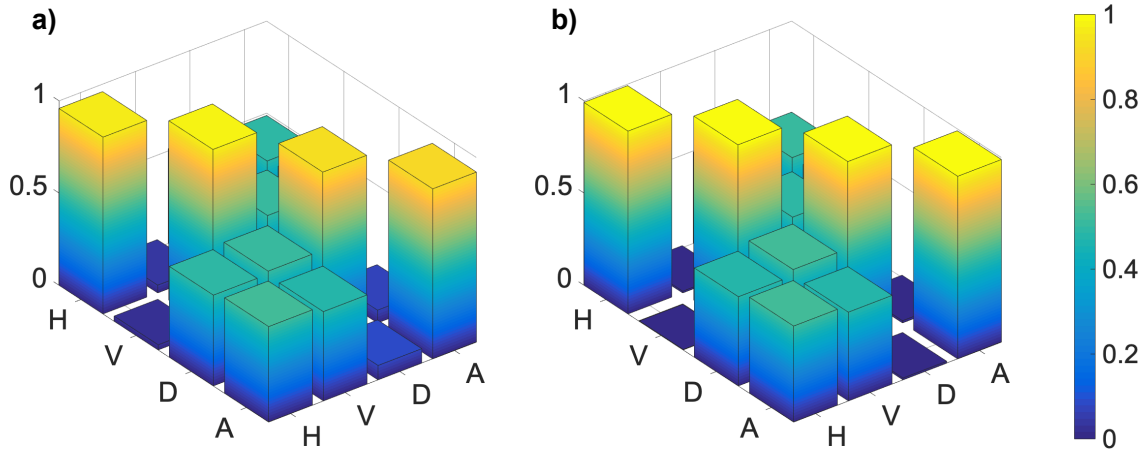


Fig. 4.6 **Outcome distribution** in the output discrimination channels for the set of four input states $|H\rangle$, $|V\rangle$, $|D\rangle$ and $|A\rangle$, in the case of zero channel losses **(a)** for the single-photon emission - fidelity $F = (99 \pm 1)\%$ **(b)** and for the WCP with $\mu_{WCP} = 0.5$ - fidelity $F = (99.78 \pm 0.03)\%$, respectively.

the expected SKR as a function of the channel loss we can experimentally evaluate the corresponding QBERs by inserting a varying set of attenuators (see Fig. 4.3). The weighted average QBER is shown in Fig. 4.7(a) as a function of the channel loss, $\eta_{channel}$. We show the experimental results for a WCP source at $\mu_{WCP} = 0.5$ and two different molecules exhibiting different $\mu_{mol} = 0.08$ and $\mu_{mol} = 0.04$. Using the total loss $\eta = \eta_{channel} \cdot \eta_{Bob}$, and eq. 2.11, we extract a value for the detector dark counts (P_D) in the range $0.4 - 4 \times 10^{-6}$ counts per pulse, while the detection error probability $e_{det} = (3.9 \pm 0.5)\%$ for a molecule with $\mu_{mol} = 0.08 \pm 0.01$ counts per pulse (see Chapter 2.8 for more details). In particular, a relevant contribution to e_{det} can be ascribed to the non-optimal efficiency of the wave-plates and fiber PC over the molecules' broadband emission spectrum at room temperature. This can be improved by adding a band pass filter (40 nm – see blue results in Fig. 4.7), which yields $e_{det} = (2.0 \pm 0.2)\%$ but to the detriment of $\mu_{mol} = 0.04$ counts per pulse. Similarly, for the WCP case we can fit the $QBER_{WCP}$ by using eq. 2.12 and taking into account the Poisson distribution of the photon number per pulse [176]. The best fit leads to a similar P_D as above and to $e_{det} = (0.8 \pm 0.1)\%$. We are now in the position to evaluate the expected SKR as a function of channel loss. For the SPS case with molecules, multi-photon events are strongly suppressed, as characterized by the second order correlation at zero time delay $g^{(2)}(0) \simeq 0.02$ (see section 4.4 for more details). The SKR_{SPS} together with the experimental data points obtained with single molecule sources at room temperature are shown in Fig. 4.7(b). (see Chapter 2.8 for more details, eq. 2.13)

In order to evaluate the performance of our single-photon source (SPS), we compare its SKR with the SKR that would be obtained using a WCP laser. Additionally, we consider the efficient vacuum and weak decoy state method proposed by Ma and co-workers [176], assuming an optimal choice of $\mu_{dec} \simeq 0.5$ and decoy $\nu_{dec} \simeq 0.05$ (see Chapter 2.8 for more details on the employed equations). We also show in the same figure the case where no decoy state is used for the attenuated laser source. This situation is actually more relevant to the comparison with our SPS, since it does not require decoy states to be secure. To compute the simulation of the weak-coherent QKD protocol without decoy, we have employed the results from Ref. [146]. For the purpose of illustrating the potential of our room-temperature molecular SPS platform, the expected SKR for an average number of photons per pulse between $\mu_{ref} = 0.3 - 0.5$ is depicted in Fig. 4.7(b) as an ideal case scenario (assuming the same $QBER_{mol}$ as in the left figure).

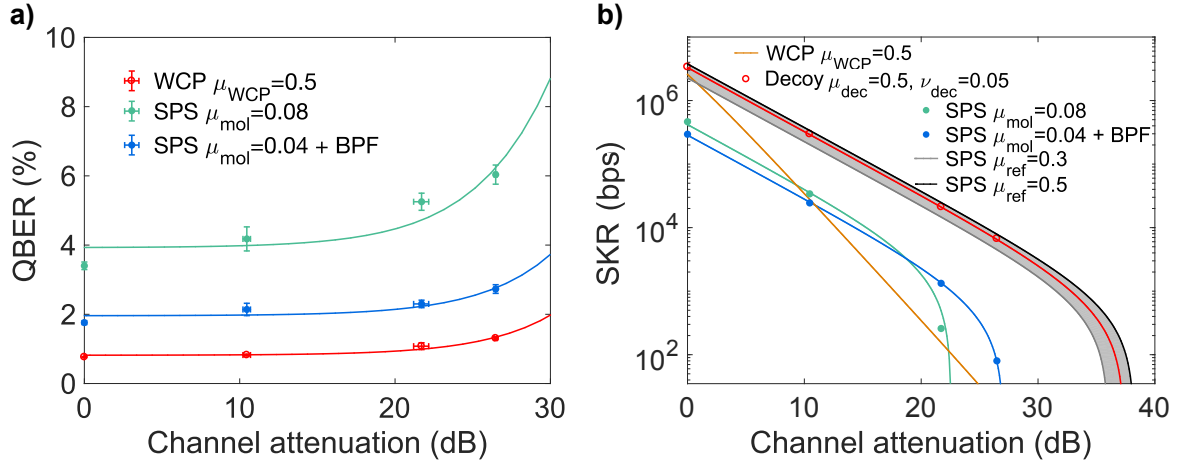


Fig. 4.7 **QKD channel characterization:** **a)** QBER as a function of total losses for two different molecule-based SPSs (with and without band pass filter) and for a WCP source. Scattered points stand for the experimental data while the corresponding lines are fits to eq. (2.11). **b)** The lines show the extracted SKRs based on the experimentally determined detection error probability (e_{det}) and dark counts for the molecule source and for the WCP SKR, without decoy and with decoy [176]. The scattered points are based on the measured QBERs for different channel attenuations. In addition, we show with the gray and black lines and shaded area the expected SPS-source SKR with an ideal $\mu_{ref} = 0.3 - 0.5$ (assuming the same $QBER_{mol}$ as in the left figure).

4.5.1 Discussion

We observe that the developed SPS is already competitive when compared to the attenuated laser case. This is noteworthy also if we consider that the results are achieved using

room-temperature operating conditions, which is a significant advantage over solid-state quantum emitters requiring cryogenic temperatures as semiconductor epitaxial quantum dots. However, a protocol implementing decoy states with attenuated lasers offers a higher SKRs compared to our 8%-efficiency source. In Fig. 4.7(b), the almost one order of magnitude difference between the SKR achieved with the SPS versus the WCP with decoy state, clearly shows that the use of our SPS platform for QKD applications would benefit from further optimization. The picture changes quickly if one considers higher efficiency values, albeit with the same $g^{(2)}(0)$. The SKR extrapolated for the ideal case scenarios of molecules exhibiting a μ_{ref} between 0.3 and 0.5 demonstrates that molecule-based SPSs could bring a key advantage upon optimization, as discussed in more detail below. If we focus on the single-photon case, we already achieved an expected SKR of ~ 0.5 Mbps for the back-to-back configuration (green circles) and, as a second reference point, ~ 80 bps for 27 dB channel losses (blue circles). These values are already better or competitive with the best ones obtained in the literature for cryogenic SPSs [213, 204, 43] or room temperature SPSs [205, 207]. In some of these implementations, longer telecom wavelengths are used and include quantum dots, nanowire quantum dots, colour centers in diamond and epitaxial quantum dots. Longer wavelengths lead to larger losses on Bob's side due to less efficient photon counting at these wavelengths [213]. They are instead optimal for fiber-based communication networks.

4.5.2 Evaluation of Optimal Molecular Mean Photon Number

As discussed above, to achieve an even higher SKR with a SPS the mean photon number has to be increased, as illustrated by μ_{ref} in Fig. 4.7(b). The molecular mean photon numbers can be enhanced upon realistic optimization of the experimental configuration. First, we need to consider the different contributions to molecular mean photon number μ_{mol} , which given by the following expression:

$$\mu_{mol} = \eta_{opt,A} \eta_{col} \eta_{mol} \quad (4.2)$$

where $\eta_{opt,A}$ is the efficiency of the optics on Alice side (see Fig. 4.3), η_{col} is the collection efficiency and η_{mol} the efficiency of the molecule emission, respectively. In particular, $\eta_{opt,A} = 0.54 \pm 0.02$ is given by the measured transmittivity of all the components along the optical path from the sample to the attenuators (Alice side). The evaluation of η_{col} is a geometrical factor based on the simulation of the angular emission profile and is calculated numerically by modelling the sample multilayer presented in the inset of Fig. 4.4(b). The molecule emission dipole is placed into a nanocrystal with thickness of 500 nm. In Fig. 4.9(a),

the resulting collected flux is compared to the total flux including also non-radiative losses for two values of the dipole distance from the gold layer, i.e. the optimal condition $d_1 = 90$ nm for enhanced collection, and a worst case $d_2 = 300$ nm. Bigger values are not considered because of the occurrence of interface effects due to the vicinity of the crystal surface, which would result in non-optimal photophysical properties of the molecule's emission which are instead not observed. Correspondingly, we can extrapolate the two bounds for the collection efficiency for our objective numerical aperture (NA=1.3 - grey vertical line in the figure) yielding $\eta_{col,1} = 0.74 \pm 0.06$ and $\eta_{col,2} = 0.44 \pm 0.08$. As final contribution to μ_{mol} to consider, $\eta_{mol} = QY\eta_{pump}ON\%$ depends on the quantum yield of the emitter QY , on the pumping efficiency η_{pump} and on the ON-times of the molecule $ON\%$, defined as percentage of emission events over excitation cycles. This latter parameter can be evaluated from the $g^{(2)}(\tau)$ at long times, which is shown in panel (b) and is measured under CW excitation for clarity. The photon bunching we observe in the microseconds range is attributed to intersystem crossing (ISC), which is responsible for the the trapping of the electron into the long-lived triplet state[219–221]. The ISC yield, which directly impacts in a detrimental way on the source efficiency, can be retrieved from the analysis of the three-level system dynamics, which we present hereafter.

For the analysis of the $g^{(2)}(\tau)$ at long times we have used the following expression[219, 185]:

$$g^{(2)}(\tau) = 1 + Ae^{-\sigma\tau}. \quad (4.3)$$

In the previous expression, A is the contrast of the correlation and σ the decay parameter, which can be expressed as:

$$A = \frac{\sigma - k_{31}}{k_{31}}, \sigma = k_{31} + \frac{k_{31}S}{1 + 2S\frac{k_{31}}{k_{23}}} \quad (4.4)$$

where the rate k_{31} is the transitions from the first triplet excited state to the ground state, k_{21} is the radiative decay rate and k_{23} is the ISC rate(see Fig. 4.8) which are extrapolated from the fitting parameters σ and A (see Fig. 4.8b)). The inter-system branching ratio is hence evaluated from the following expression[185]:

$$\phi = \frac{k_{23}}{k_{21} + k_{31}} \quad (4.5)$$

From ϕ , the average trapping time in the dark triplet state ($OFF\%$) can be extrapolated, and hence $ON\% = 1 - OFF\% = 77\% \pm 5\%$ is retrieved. After calculating this ISC, next step is to

evaluate the pumping efficiency which can be expressed as:

$$\eta_{pump} = P_{e,\infty} \frac{R(P)}{R_\infty} \quad (4.6)$$

where $P_{e,\infty}$ is the excitation probability and $\frac{R(P)}{R_\infty}$ is the ratio between the collected rate at the operational laser power and the maximum rate. Assuming an excitation probability $P_{e,\infty} = 0.75$, which is the maximum value at room temperature [222], we obtain $\eta_{pump} = 0.47 \pm 0.07$. Hence, we can extrapolate the quantum efficiency for the two considered cases of dipole distance, yielding $QY_{ex,1} = 0.6 \pm 0.1$ and $QY_{ex,2} = 0.9 \pm_{0.3}^{0.1}$. These values are lower than the almost unitary QY displayed by several PAH molecules [223], but this is motivated by the room-temperature operation at which the QY can be strongly reduced owing to temperature dependent non-radiative decay pathways. Finally, based on the estimation of all the involved

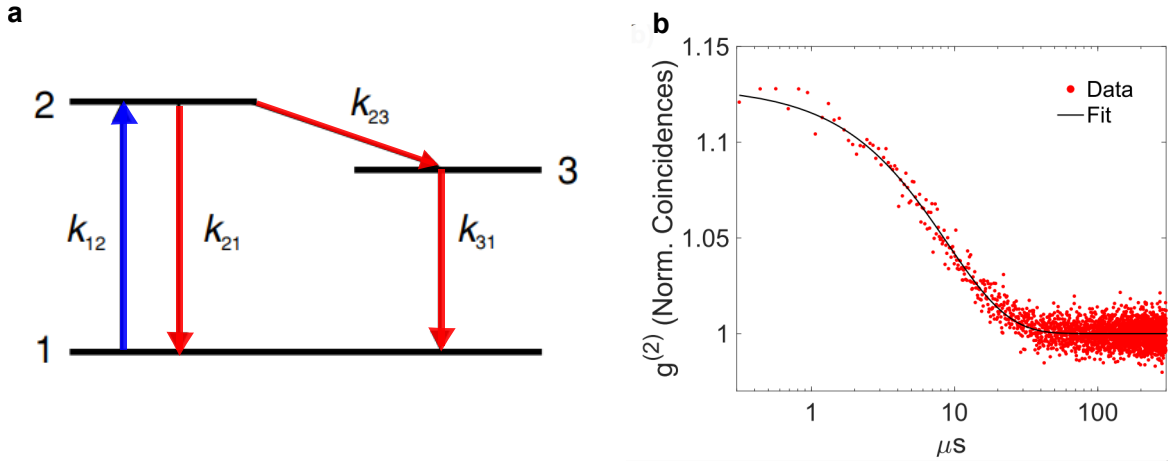


Fig. 4.8 **a**) A simplified energy level diagram for a three-level model **b**) Experimental data (dots) for the $g^{(2)}$ at long times and fit (line) describing a three-level system dynamics [220].

experimental parameters contributing to μ_{mol} , we can extrapolate the reference value μ_{ref} in the ideal case scenario in terms of sample configuration and setup optimization. If we consider the demonstrated 99% collection efficiency for organic molecules in Ref.[211], a realistic improvement of the optics efficiency up to $\eta_{opt,A}^* = 90\%$, and the upper bound to the pumping efficiency $\eta_{pump}^* = P_{e,\infty}$, we can obtain reference mean photon number μ_{ref} ,

$$\mu_{ref} = \eta_{opt,A}^* \eta_{col}^* \eta_{pump}^* QY_{exp,i} ON\% \quad (4.7)$$

which yields $\mu_{ref,1} = 0.31 \pm 0.06$ and $\mu_{ref,2} = 0.5 \pm 0.2$ for the two estimated values of $QY_{exp,i}$. This considered, the combination of molecule-based emitters and an optimal optical

configuration would bring beyond the break-even point and become advantageous with respect to the use of weak coherent pulses and decoy states.

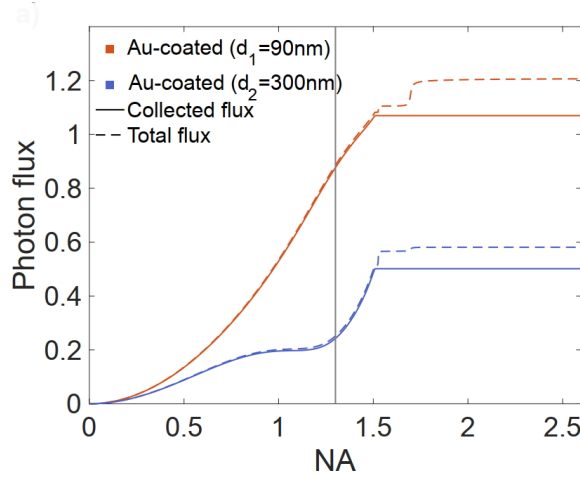


Fig. 4.9 Normalized photon flux as a function of the objective numerical aperture NA. The photon flux is calculated for the sample multilayer shown in Fig. 4.3 and composed of 120nm of gold film and 500nm-thick nanocrystals in PVA on a glass substrate, and is then normalized to the emission in a homogeneous medium of anthracene. The collected flux (solid line) is compared to the total flux (dashed line) integrated in the full 4π solid angle around the dipole emitter. Colours stand for different dipole distances d_i from the gold layer.

4.6 Conclusion

We successfully implemented a proof-of-concept QKD setup employing a deterministic single-photon source operating at room temperature. The results, in terms of expected SKR_{mol} (0.5Mbps at zero losses), are competitive with state-of-the-art experiments - at cryogenic and room temperature - and can be further improved in the near future by optimizing the nano-photonics of the sample configuration and the optical setup. In this regard, taking into account all the experimental contributions to the overall source efficiency and analyzing in detail the margin for improvement, we have evaluated the achievable SKR_{mol} of the molecular emitter demonstrating the potential advantages in using the generated single-photon states even compared to the decoy state performances.

The room-temperature operation and long-term photostability of the molecular emitter makes the proposed hybrid technology particularly interesting for satellite quantum communication. With an ultra-compact and cost-effective QKD setup configuration, this technology could be integrated into next-generation satellite quantum-encrypted networks, or used in a CubeSat for preliminary testing and experiments. Furthermore, the system can be efficiently operated

in fiber communication networks upon down-conversion to telecom wavelengths [224, 225]. The future upgrade to real-time state-preparation and -measurement has the potential to significantly enhance the performance and reliability of the proposed QKD setup. This would enable a continuous monitoring and optimization of the single-photon source, which is crucial for achieving high SKR_{mol} values and for detecting potential eavesdropping attacks. Additionally, the integration of real-time state-preparation and -measurement can boost the practical implementation of truly single photons for QKD applications both in terrestrial and spatial links.

Chapter 5

Progress towards Real-time Encoding with room temperature sources

In this chapter, we demonstrate real-time polarization encoding of single-photon states for quantum communication at room temperature using a Polarization Modulator. We first recall the working principle of such a device based on an Electro-Optic Modulator (EOM). Then we provide a characterization of the modulator capabilities after setup optimization. Additionally, we outline the procedure for encoding three distinct states using the EOM with an RF signal applied for both weak coherent pulses and quantum-emitter based single photon sources. We present the experimental setup and the preliminary results obtained towards an efficient and reliable polarization modulation for quantum communication using DBT-based SPS.

5.1 The Polarization Modulator

In the previous chapter we have explored the potentiality of a molecular SPS as resource for QKD systems based on true single-photons. However, in order to implement a real device, an arbitrary polarization choice for each photon must be achieved. This request implies a fast modulation method, able to switch among the output states within the waiting time between successive pulses, typically of the order of 10 ns or less. Such a demanding capability is nowadays routinely obtained thanks to the implementation of integrated electro-optical modulators (EOM), which combine high speed operation (around 10GHz) with low voltage driving signals (around few volts, i.e. three orders of magnitude less than equivalent free space modulators). Generally speaking, an EOM is a device based on a non-linear crystal whose refractive index can be modulated by applying external electric fields. Hence, such

devices are essentially phase modulators. This effect is exhibited in polar materials as well as ferro-electric crystals, with lithium niobate ($LiNbO_3$) being a commonly used material for integrated-optical modulator fabrication. In order to work as polarization modulator, the polarization of the input light beam has to be set circular or (linear), at an angle of e.g. 45 degrees with respect to the modulated axis. The beam can be hence separated in two components, only one of which undergoes phase modulation according to the applied electric field. The output polarization can be switched in this way between orthogonal states for any couple of voltage values whose difference corresponds to a π phase shift (commonly referred to as V_π). The polarization modulator used in the experiment is a custom model by EoSpace Inc. (PM-0S5-20-SFA-SFA-770/830-DP-UL), shown in the Fig.5.1 together with a table of its basic characteristics from data-sheet. In fact, integrated EOM in the optical domain



Key Specifications

Model	PM-0S5-20-SFA-SFA-770/830-DP-UL
Insertion Loss	0.44dB (66%)
PDL	1.8dB (90%)
V_π	3.1V

Fig. 5.1 The EOSPACE Polarization Modulator, model number PM-0S5-20-SFA-SFA-770/830-DP-UL, is shown on the left side; key specifications are listed in the table on the right side.

can generally work only with a single polarization, due to constrains given by fabrication techniques. This *de facto* prevents the implementation of integrated polarization modulators. EoSpace Inc. is the only company which accepted the challenge of fabricating a custom device with low losses for both TE and TM modes, operating in the 780-830nm wavelength range. The modulator provided to us shows insertion loss and Polarization Dependent Losses (PDL) equal to 0.44 dB and 1.8 dB, respectively, and is hence adequate for the project.

Working with an EOM-based polarization modulator, it is crucial to carefully stabilize the temperature of the device. Indeed, due to the actual length of the waveguide (around 70 mm), the phase difference accumulated between the light components aligned with the two axes of the modulator just in passing (for zero applied voltage) is highly sensitive to temperature drifts. Even though this phase does not change the required V_π , it determines a "drift" of the basis used for encoding. In our experiments, we have exploited a home-made

PID temperature controller to stabilize the temperature of the modulator around 40°C with a relative uncertainty lower than 10^{-5} . Details on the implementation of the system can be found in the dedicated technical subsection 5.3.

5.2 PM for Real-time State Encoding

In order to successfully operate polarization encoding on single photons with an EOM-based polarization modulator, the following conditions must be satisfied:

- The input polarization must be splitted equally into the TE and TM modes of the modulator;
- The switching time for the voltage applied to the modulator must be faster than the pump laser repetition rate and the amplitude should be equal to V_π (for orthogonal state preparation);
- The switching events must be temporally located in the quiet time window between successive wavepackets.

In order to set up this modulation system, we have considered the apparatus reported in fig. 5.4, with Bob's detection station realized with fibered elements (as already introduced in chapter 4) and directly coupled to Alice's station.

The first point in the list of conditions is not trivial since the 1m-long single mode fibers at the input and output of the integrated modulator act on the polarization in unknown ways which are also dependent on temperature and strain. As a consequence it is not trivial to have a direct measurement of the polarization at the entrance and at the exit of the electro-optic waveguide. The protocol elaborated to fulfill this request is based on a blind exploration of the polarization states at the input of the fiber while monitoring the effects induced by a varying signal applied to the modulator on the output state. Indeed, for an arbitrary polarization at the fiber input (set by means of a half-wave and a quarter-wave plates placed just before), the output polarization must vary according to the applied voltage unless the polarization at the entrance of the waveguide is linear and aligned with one of the two crystalline axes (let us call them H and V polarizations for simplicity), in which case simple phase modulation occurs and the beam polarization does not change. Once identified such reference state, the required input polarization is obtained for an additional half-wave plate rotation equal to $\pi/8$, which corresponds to a change from H or V to D or A polarization at the waveguide entrance. The second step is more straightforward. It consists in estimating the voltage step amplitude for which the two output states are orthogonal, i.e. the relative phase between the two

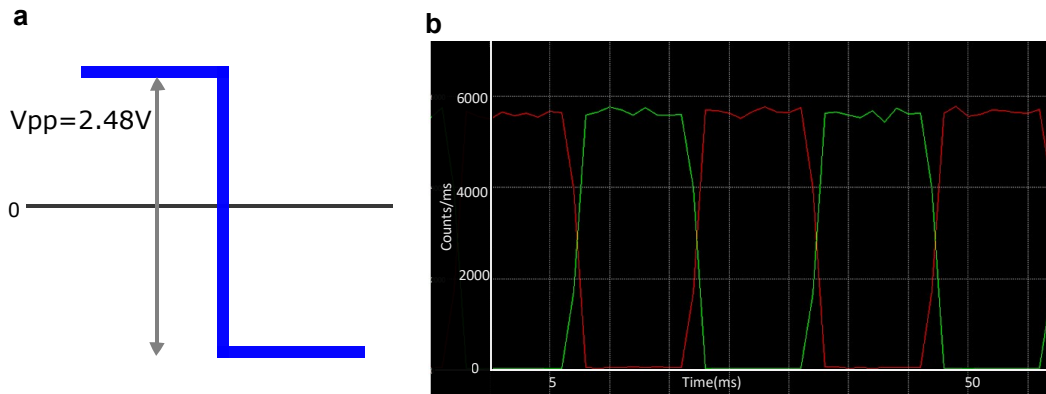


Fig. 5.2 Two Orthogonal States Encoding: **a** A square wave with a peak-to-peak voltage of 2.48V, a frequency of 10Hz, and an arbitrary offset is used to generate two orthogonal states. **b** Chart of the count rates measured for the two fibered SPADs of Bob's station (red and green curve, respectively). The traces show very good extinction in the two orthogonal channels, yielding a QBER smaller than 1%. The integration time for counters is 5 ms and the polarization state is switched every 50ms.

components is changed by π . Actually, the orthogonality condition is achievable only if both first and second conditions are fulfilled at the same time.

The third condition implies to determine the correct time delay between the external trigger for the pump laser pulse and the switch instant for the voltage applied to the modulator. Again we have identified it looking at the effects of arbitrary chosen values: i.e. the delay corresponding to the lowest QBER.

The first and second steps of our procedure can be conveniently implemented with CW laser light and then checked/optimized for pulsed operation, for which lower performance is expected due to broader spectrum.

As recalled in the introduction, the output polarization is extremely sensitive to temperature fluctuations. Indeed, by tracking the polarization drift for constant conditions, we found evidence that a temperature control of the order of 0.1°C still entails up to 10% polarization fluctuations, which brought us to upgrade the level of control to 0.001°C .

5.2.1 Different States Encoding using an Arbitrary Waveform Generator (AWG)

Another temperature-related problem we have immediately faced working on the implementation of the EOM-based polarization modulator is determined by the heating induced by the applied voltage. In fact, in order to work at very high frequencies, the modulator circuit needs to be 50 Ohm terminated. After careful characterization of such effect for our modulator,

we found that passing from ground level to V_π (corresponding to a power dissipated in the internal circuit of around 0.1W), on top of the expected relative phase shift of π , the two polarization components undergo an additional relative phase shift of more than 2π which takes place in a time scale of 10s. As a consequence, a strategy to avoid sequence dependent Alice's base rotations had to be developed in order to move on with the implementation of real-time encoding. The solution we found overcomes this issue by operating the modulator with periodic arbitrary step functions, with the following constraints:

- periodicity of the arbitrary sequence must be shorter than the thermalization time scale in the modulator (i.e. shorter than 1s);
- average dissipated power in the modulator must be constant.

For the optimization of input polarization and V_π , we have considered a periodicity of 0.1s (10Hz), which on one hand is fast enough to guarantee no appreciable temperature oscillations, and on the other hand allows enough signal integration on the SPADs to properly evaluate the quality of the polarization encoding.

The manufacturer's data sheet may provide an estimate of the half-wave voltage (V_π), but it is often necessary to determine the actual value experimentally. Just to initiate the measurement we fed the modulator with a square wave ($V_{pp}=3.1V$, $F=10Hz$). The integration time for the SPADs was set to 5ms, a compromise between time resolution and signal to noise ratio, and the photon flux was monitored continuously for both detectors on a graph chart thanks to a digital counter (quTAG by qutools GmbH) connected to the polarization controller. A typical time trace after input polarization and V_π optimization is shown in Fig. 5.2. The green and the red traces indicate the count rates registered for the two SPADs, with the stable values, separated by low resolved transients, corresponding to the encoded states. Hence, the extinction ratio in such traces holds a direct estimation of the attained QBER. We have explored the dependency of V_π and attainable QBER on the voltage offset applied to the modulator, with the following results:

- $V_\pi=V_{pp}=2.32V$, Offset=-1.16V
- $V_\pi=V_{pp}=2.48V$, Offset=0V (Best)
- $V_\pi=V_{pp}=2.63V$, Offset=1V

The following step of the experiment consisted in providing three states encoding, namely H or V, and AD or D. To achieve this result, we fed the AWG with an arbitrary waveform having three different voltage levels corresponding to the different states. From the two state study we learn that best performance is achieved working around zero voltage. The

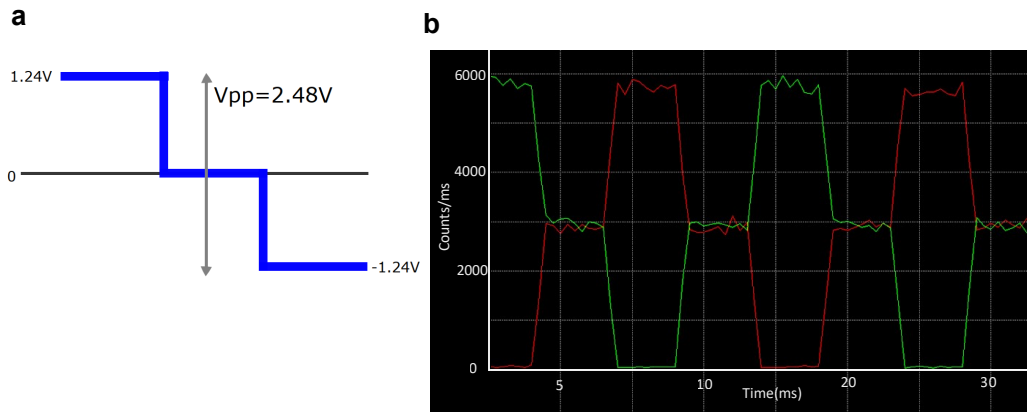


Fig. 5.3 Three States Encoding: **a** Waveform with three voltage levels (1.24V, 0V, -1.24V) used for three-state encoding. **b** Chart of the count rates recorded for the two fibered SPADs of Bob's station, confirming successful encoding. Very clean discrimination between the three states is reported, confirming the QBER level read for two-state encoding, and showing $50 \pm 2\%$ spitting of the photon stream when the third state is encoded.

waveform was hence designed with +1.24V for state zero, -1.24V for the orthogonal state (w.r.t. state one), and 0V for the third state, as shown in the Fig. 5.12a). The V_{pp} of 2.48V is chosen because it yields lower QBER (0.1%) but for the other two cases QBER is $\approx 1\%$. It is worth noting that, beside confirming the high quality QBER of 0.1% for state zero and one, the third state results in the same counts on the two SPADs with few percent error, hence demonstrating successful implementation of the three state encoding.

5.3 Temperature Stabilization for PM

Maintaining a stable temperature is crucial for the reliable operation of the modulator. Temperature fluctuations can cause significant changes in the polarization of the light at the output of the modulator. After moving the modulator inside a dedicated thick copper box and implementing a PID temperature controller on the latter, we observed a significant improvement in the stability of the polarization.

The modulator is sandwiched between two copper plates, so as to ensure efficient heat exchange between the two parts. In order to keep the system as simple as possible, we have considered resistive actuators (acting as heaters), while the temperature of the copper box is measured with a thermistore. The target temperature has been chosen so that active heating and passive cooling (with actuators switched off) show almost the same time constant, condition obtained for 40°C in our lab. In order to manage correctly the minute-long time constant of the copper box, we have implemented a digital PID controller, based on a home-

made software loaded on a commercial simple FPGA card. Monitoring and adjustment can be easily managed through USB connection to the PC and a simple user interface; heating power is provided by an external 20V-10A power supply and modulated by means of a Pulse Width Modulation stage integrated in the card (see Fig. 5.4). With the precise temperature stabilization system in place, any temperature fluctuation/drift in the room is strongly mitigated, ensuring that the polarization remains constant and reliable over extended periods.

(we have been able to perform continuous measurements of polarization using SPADs for 24 hours without any significant drift in the polarization state).

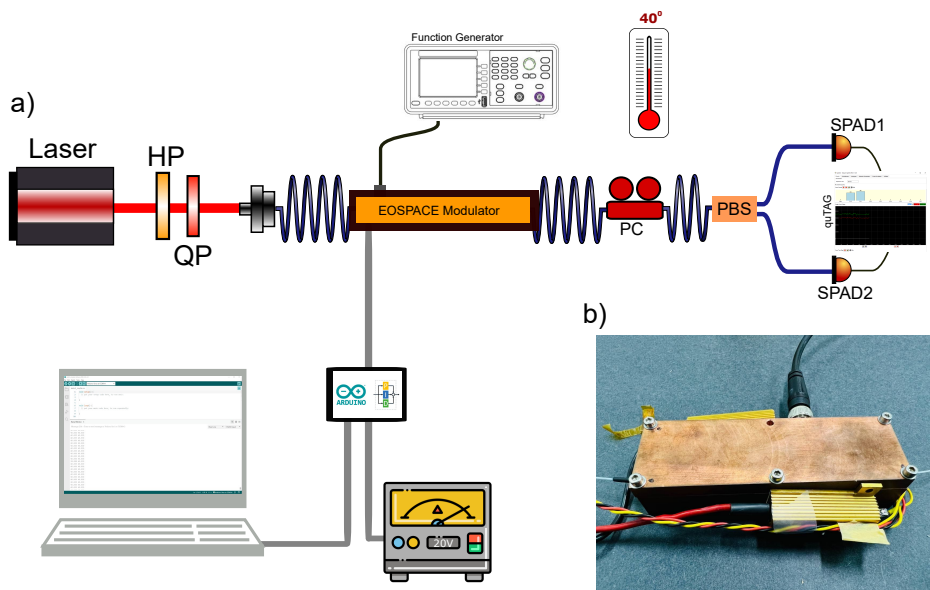


Fig. 5.4 Setup for real-time polarization encoding: **(a)** The light to be modulated (CW laser in this case) enter the modulator after passing a manual HWP-QWP stage. The output fiber is directly connected to the fiber PC of Bob's station. The fiber PBS and fiber SPADs follow. The fiber PC is set after input polarization and V_π optimization, searching for maximum achievable extinction ratio. The copper plates are tightly sandwiched around the modulator and connected to a digital PID temperature controller. Monitoring and parameter setting are performed thanks to a simple PC interface. **(b)** Photo of the modulator sandwiched with copper plates and heaters.

5.4 Real-time QKD Experiment

After the successful implementation of the polarization modulator for two and three state encoding with CW laser radiation, we begin the real-time quantum key distribution experiment using both WCP and single photons from SPS. To assess the capabilities of the system,

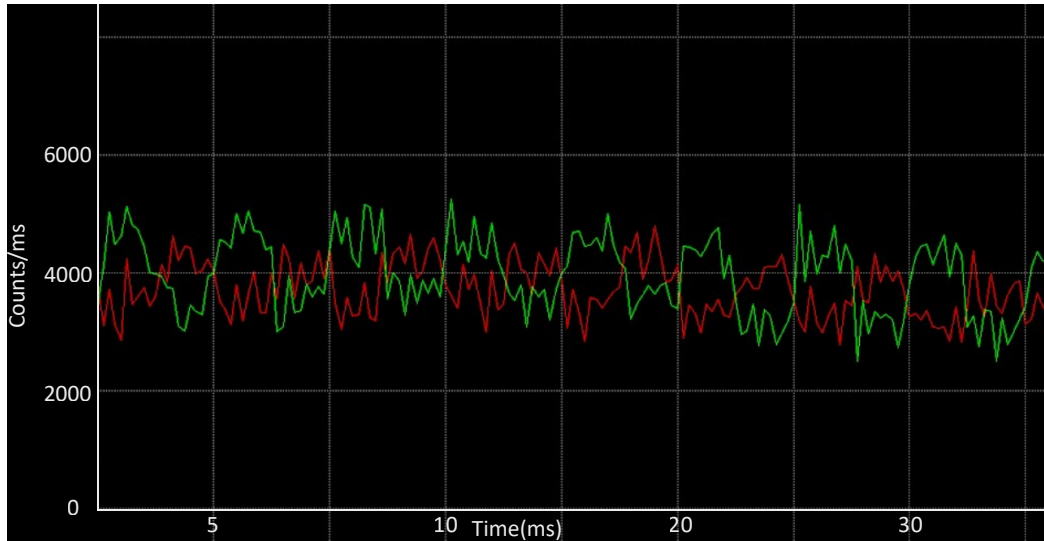


Fig. 5.5 QBER under Pulsed Operation: Two orthogonal states have low extinction resulting in very high QBER

we have performed the same analysis described above just replacing the light source with the pulsed ones. A similar QBER was expected, but instead moving from CW to pulsed operation, even with the very same laser source (PicoQuant lase), the device is no longer working: for any choice of Bob's base, low contrast for the two nominally orthogonal states and low extinction for any of them was found, with QBER of the order of 50% which is shown in the Fig. 5.5. Probing the system with single-photon emission from molecular SPS resulted in even a lower extinction associated to the polarization modulation. This behavior has been interpreted as the result of Polarization Mode Dispersion (PMD) caused by walk-off between the two orthogonal components and/or differential phase dispersion for the various spectral components in case of broadband emission.

5.4.1 Polarization Mode Dispersion

When a light beam is guided at an angle of 45° along the $LiNbO_3$ waveguide, it experiences Polarization Mode Dispersion (PMD) due to the different speeds at which the orthogonal polarization components travel, caused by the material birefringence. EOSPACE modulators are particularly susceptible to PMD due to the path delay between the two orthogonal polarization components, as depicted in Figure 5.6. The length of the modulator is 71 mm. The refractive indices of ordinary and extraordinary axes are $\eta_{ord} = 2.21$ and $\eta_{ext} = 2.14$ respectively. therefore, when an optical pulse travels through this modulator, an overall path delay of 16.5ps is produced between the orthogonal components. The optical pulses we have employed to test the modulator with WCPs are characterized by a length of 50 ps

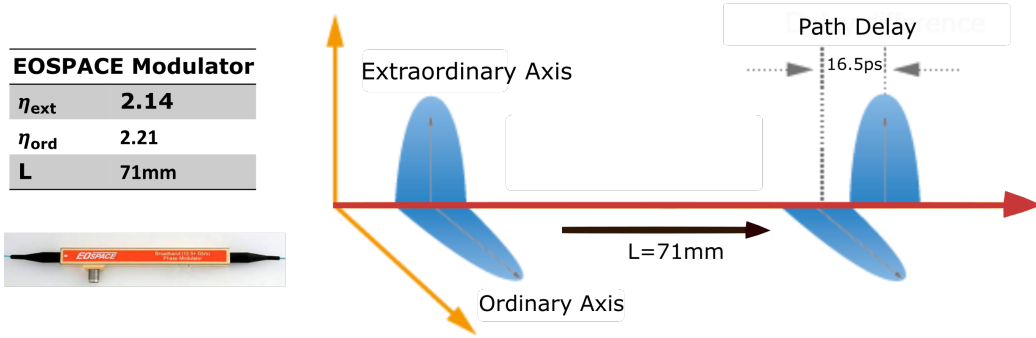


Fig. 5.6 PMD in the EOSPACE Modulator: Length of the $LiNbO_3$ waveguide $L=71$ mm, refractive index for the two axes $\eta_{ord} = 2.21$ and $\eta_{ext} = 2.14$. Overall differential path delay for the two polarization components: $L * (\eta_{ord} - \eta_{ext}) = 16.5$ ps . In the image we present a pictorial description of the PMD. In the temporal windows in which the envelope for the two components are not overlap, the polarization is modified according to their relative amplitude.

and a spectral width of 0.3 nm (they are obtained by a Picoquant LDH-D-FA-765L laser). Their length in particular is comparable to the accumulated delay, determining a not-uniform polarization along the pulse at the output of the modulator. If the pulse is longer than 1 ns, the PMD induced by the walk-off is negligible instead[226]. Our SPS shows a lifetime of ~ 3.5 ns, and hence do not suffer the effects of the walk-off. However, its broad spectrum, as wide as ~ 50 nm, can be responsible for a relevant dispersion among the different components, justifying the experimental evidence.

5.4.2 QKD with Molecular SPS at cryogenic temperature

We have shown in Chapter 3 that at cryogenic temperature our SPS holds the same lifetime (around 4ns) but can provide very narrow line-width photons (<100 MHz, i.e. $<2 * 10^{-4}$ nm). This emission is hence ideal to verify if, in the case of photons from a molecular SPS, the failure of the modulation system is caused by wavelength dispersion. A sketch of the setup implemented for this investigation is shown in Fig. 5.7. We exploited for this test a standard sample for cryogenic pulsed operation as described in the previous chapter. In this case, however, the photon stream selected by the Notch filter (the narrowband component corresponding to the ZPL) was coupled to the input fiber of the polarization modulator. A standard pre-characterization of the source was performed in order to select a proper SPS. In particular, a molecule showing a lorentzian FWHM of 81.1 ± 0.2 MHz after excitation spectroscopy, and a $g_{HBT}^{(2)}(0) = 0.01 \pm 0.02$ (obtained using the modulator circuits as HBT setup), was eventually selected for the QKD experiment (see Fig. 5.8).

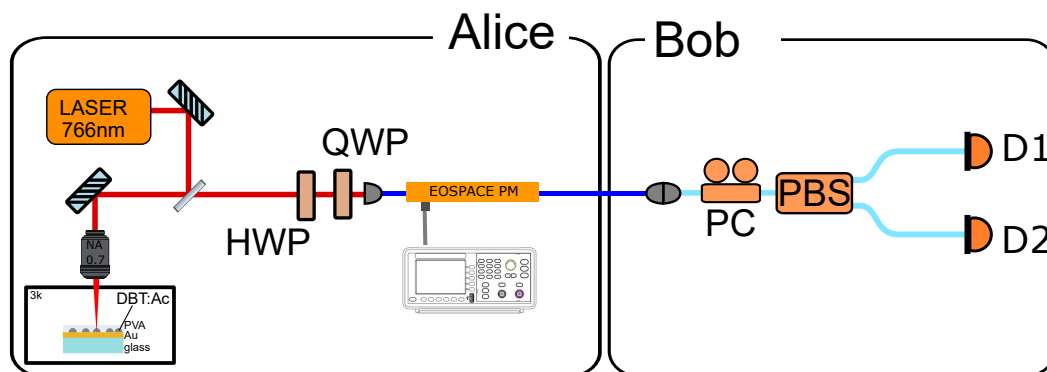


Fig. 5.7 Real-time QKD Experiment with SPS at 3K: **Alice:** DBT molecule kept inside cryostat is excited with a non-resonant laser and emission is collected via air objective (NA=0.7). A notch filter is employed to extract the ZPL emission which is then sent, after proper polarization setting, to the polarization modulator **Bob:** Fibered PC is employed before PBS in order to match Alice and Bob bases and read the information with minimal error (QBER).

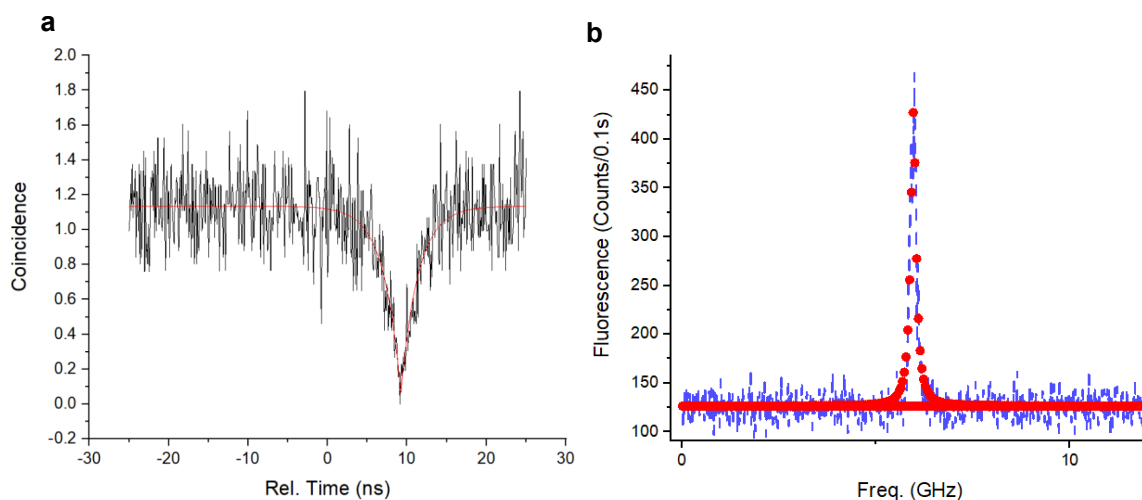


Fig. 5.8 DBT Molecule Characterization: **a)** Second order autocorrelation function under CW operation, best fit to the data yielding $g^2(0)=0.01\pm 0.02$ **b)** Emission intensity in the PSB as the resonant frequency is scanned across the ZPL; best lorentzian fit to the data yielding a FWHM of 81.1 ± 0.2 MHz

After setting the correct input polarization using the procedure described above and resonant CW laser light, we could test the effectiveness of the polarization modulator on triggered narrow-band single-photons. Considering two state encoding, a QBER as low as $2.3 \pm 0.2\%$ was measured. This value is quite good, even compared to manual encoding of chapter 4, and confirms the idea that efficient modulation of photons from a SPS at room temperature is prevented due to the presence of wavelength dispersion (i.e. wavelength dependent delay between the two polarization components), responsible for a wavelength dependent output polarization.

5.4.3 Probing frequency dispersion in the modulator: different bases for different wavelengths

In order to thoroughly understand the causes that prevent a proper polarization modulation in case of broadband single-photons, we performed another set of measurements. After optimization of the modulation system for a specific CW wavelength (with measured QBER below 1%), we have explored the attainable QBER for different wavelength considering only re-optimization of Bob's polarization base. Thanks to our tunable source (MogLab Motorised Cateye Laser), we could explore a significant wavelength range (767-789 nm), even though not completely overlapping the molecular emission spectrum (780-830 nm). The results for this analysis are reported in fig. 5.9. We were able to recover QBER below 1% for any selected wavelength. It is clear from this study that orthogonal state generation for all the probed wavelengths is obtained operating the modulator in the very same conditions (both input polarization and applied voltage). In other words, we have got strong evidence that the bad result obtained for broadband emission can be attributed to a wavelength dependent rotation of the encoding base, while the modulation depth is correct over the whole explored frequency range. This is in agreement with the interpretation that the problem is given by wavelength dispersion, responsible for a wavelength dependent phase between the two orthogonal components at the EO waveguide output. V_π is instead only weakly wavelength dependent.

5.4.4 Polarization Mode Dispersion Compensation

In literature we can find several ways for PMD compensation. E.g. using Polarization Maintaining Fibers such effect is obtained leveraging on the difference of refractive index for the two principal axes [227]. Another strategy, able to provide high degree of compensation on a broad frequency range, consists in appending a twin modulator to the first one, with axes rotated by 90° with respect to it[226]. In this way, the two polarization components end up

with the same total path delay, while the total voltage-related delay is determined by the sign and the amplitude of the voltage applied to each of the modulators (simplest implementation consists in passive use of the second one, i.e. no voltage applied to it). A more compact design based on the same principle is obtained using a single modulator in double passage, with the second way occurring after polarization swapping, e.g. thanks to a fibered Faraday Rotator Mirror (FRM).

Wavelength(nm)	QBER (%) Before/After Changing Measurement Bases?	
	Before	After
767.363	7	0.42
774.997	42.2	0.59
779.976	0.4	0.3
779.98	47.5	0.2
780.025	0.4	0.2
781.866	0.65	0.3
781.914	0.4	0.1
781.96	0.9	0.1
782.009	0.49	0.06
785.984	1	0.17
785.99	0.94	0.1
786.041	20.5	0.14
788.999	5.2	0.3

Fig. 5.9 QBER vs Wavelength: QBER as a function of wavelength before and after changing measurement base. It is evident from these measurements that the same setting for the modulator are valid for all the considered wavelength, while the "encoding" base is wavelength dependent.

Test with a Faraday Rotating Mirror for PMD Compensation

In order to overcome the wavelength dispersion problem in our device we have implemented the latter configuration introduced in the last section, with the help of a fiber-based optical circulator and a fiber-based FRM[228]. The setup is shown in Fig. 5.10. A polarization insensitive optical circulator is inserted before the modulator, as first element in the fiber circuit. It allows for the redirection of most of the input light toward the modulator, while

back reflected light is deviated on a third way, different from the input. A HWP and a QWP at the entrance of the fiber circuit are still used for setting the input polarization with respect to the EO waveguide axes. The FRM returns light after rotation of the polarization by 90° . When the light is reflected back from the FRM and passes through the modulator for the second time, the applied voltage is turned to zero to avoid updating the polarization of the previously modulated signal. In this way, second passage in the modulator only affects the phase accumulated on passing, and only PMD is compensated. With this new configuration, the alignment and testing procedure exploited up to here was no more valid. Indeed, on the one hand, the applied voltage has to be switch back to zero value at each event; on the other hand, the PMD compensation makes the system free from the temperature dependent relative phase problems. The new procedure consists hence on the use of a periodic two step function with periodicity equal to the time separating the two passages of a pulse through the modulator. Moreover, the laser repetition rate has to be chosen such that the following pulse does not arrive until the previous one has left the modulator after the second passage, saving the signal from double modulation. The modulator is 7.1 cm long, and the fiber is 2 m long (FRM and the Modulator, each, 1m). Light pulses take $\approx 12\text{ns}$ to cover this whole path. So, the pulses must be separated by at least $\approx 12\text{ns}$ to save from double modulation. In our implementation, we utilized 40 MHz (25ns pulse spacing), which is more than necessary for WCP, but required to ensure proper separation among the wavepackets in case of single photons from a molecule.

Now the QBER can be evaluated by measuring one state per time: maximum extinction at one SPAD in case $V_\pi/2$ is applied to the modulator (state zero), and same estimation for the other SPAD in case $-V_\pi/2$ is applied (state one), without any readjustment of Bob's base between the two measurements.

We tested the new device and procedure with two-state encoding for WCP, using the PicoQuant laser introduced above (pulse characteristics: 50ps of envelope extent, 400GHz spectral width). The behavior of the modulator is greatly different with respect to the single pass configuration, with a reported QBER equal to 1.4%. The new setup is hence able to avoid the PMD issue and provide high quality polarization encoding in case of implementation for WCP. However, a careful test of the device with our molecular emission, performed just after the WCP one, revealed an overall efficiency of Alice stage μ limited to ≈ 0.0004 , and only a weak improvement of the achievable QBER (limited to $\approx 40\%$). Also the reduction of the spectral width by means of the 10nm-wide bandpass filter resulted in a very small effect on QBER.

The system still fails to work properly in the case of broadband emission.

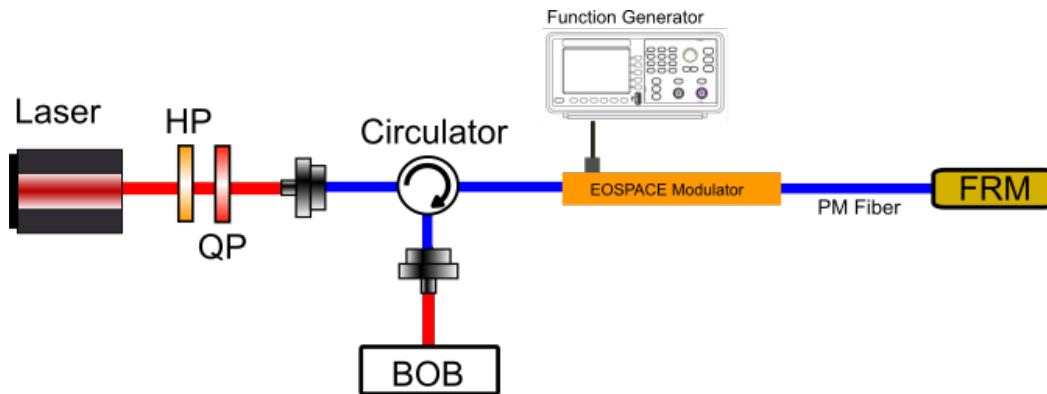


Fig. 5.10 FRM-based PMD Compensation: HWP and QWP are employed to set input polarization. Circulator operates in a way that light entering from one port exits from the next port (clockwise ordering). FRM reflects light back with 90° Polarization rotation. The efficiency of the circulator and FRM is 75% and 34.6% respectively.

Test with Sagnac Ring-based PMD Compensation

The setup based on FRM shows great advantages given by the simplicity and portability of the system, but also is accompanied by relevant losses and a limited working bandwidth. A careful experimental estimation of losses yields ≈ 4.6 dB, while the optimal operation bandwidth is dominated by FRM (bandwidth 20nm). Both these aspects are generally not relevant in case of WCP implementation, but make the upgrade useless in case of application to SPS at room temperature, as reported in the previous section. Starting from the last finding, we have developed an alternative design for PMD compensation based on free-space optical elements, which guarantees reduced losses and more than 100nm-wide operation range. The alternative device is depicted in fig.5.11. It is based on a Sagnac-like ring interferometer: at the output of the modulator, the signal is split into two paths by employing a PBS. The reflected and transmitted beams are then re-combined on the same PBS by using two mirrors. With the help of a HWP plate, the polarization of each beam is rotated by 90° , and as a consequence all the light is sent back into the modulator, but with swapped polarization components. All the optical elements used in the circuit have been selected in order to guarantee broadband operation; in particular, we considered an achromatic HWP (Shalom EO Technology 2081-004, working range 690-1200nm) for the swapping operation.

After configuration, we are currently testing the new PMD compensated setup for real-time polarization encoding with both WCP from PicoQuant laser and single photons from molecules at room temperature. The QBER obtained for WCP is very close to the value found with FRM-based PMD, verifying the proper operation of the new device. Investigation on real-time polarization modulation of molecular emission has not been performed yet, but

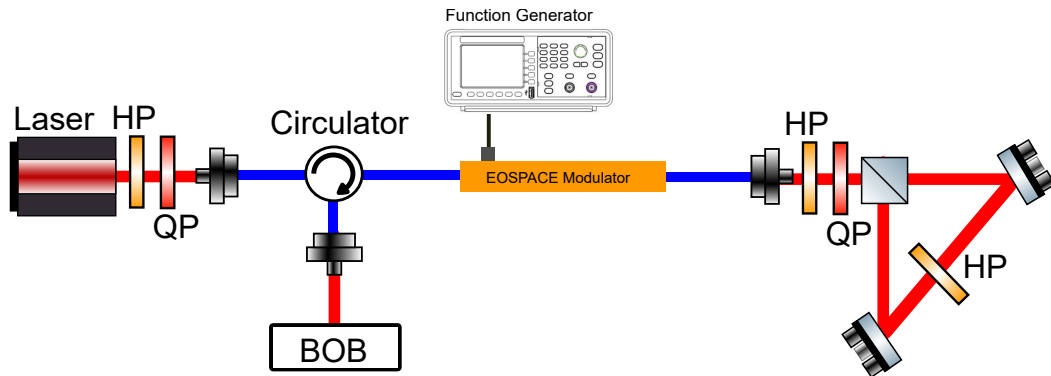


Fig. 5.11 Sagnac Ring based PMD Compensation: a broadband free-space PBS is used to split the modulated signal into two paths. The reflected and transmitted beams are then combined using two mirrors and a HWP to send the light back into the modulator. The HWP and QWP before the PBS have to be set so as to separate the two polarization components defined by the modulator; this can be determined by finding the condition for which PBS shows 50/50 splitting whatever applied voltage.

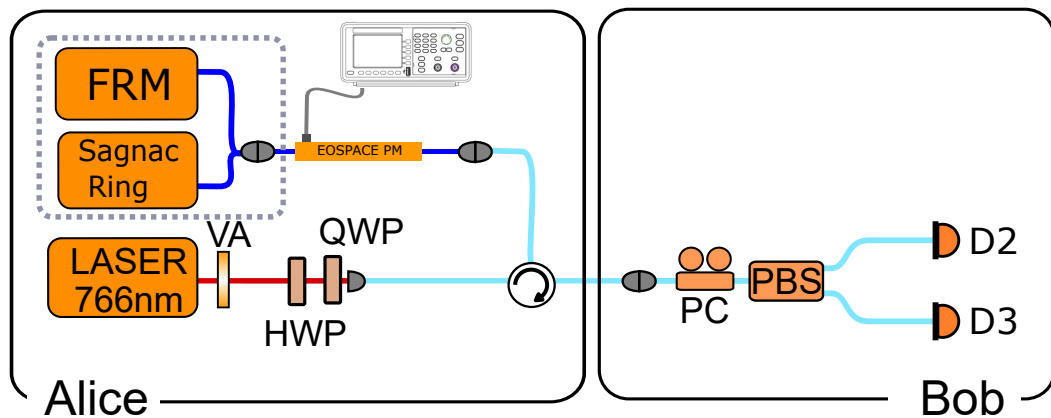


Fig. 5.12 Real-time QKD Experiment with WCP: Laser pulsed are attenuated using VA. HWP and QWP are used to set input base for the modulator. Circulator is used to direct light from the source to the modulator and then from the modulator to Bob. PMD correction is obtained either with FRM or Sagnac ring (Dotted Box) back reflectors. On the Bob side, PC is used to discriminate between two orthogonal states with the following PBS and SPADs (D1 and D2) detection stage.

Source	Temperature	FRM/Sagnac Ring	BPF	QBER(%)
CW Laser	-----	-----	-----	0.1
Pulsed Laser	-----	-----	-----	≈45
Pulsed Laser	-----	FRM	-----	1.4
Pulsed Laser	-----	Sagnac Ring	-----	≈1.5
SPS	3K	-----	-----	2.3
SPS	RT	-----	-----	>45
SPS	RT	FRM	-----	<45
SPS	RT	FRM	10 nm	≈ 40

Fig. 5.13 QBER for Different Sources: Modulator was characterized with CW laser and QBER is as low as 0.1%. Our SPS at cryogenic temperature gives QBER of 2.3%. QBER is ≈ 45% while using pulsed laser and SPS at RT. Using FRM/Sagnac ring with Pulsed laser reduces PMD resulting in QBER of 1.4%.

is scheduled in the next months. However, the preliminary results obtained for WCPs and the as broadband operation as required to manipulate in homogeneous way the whole molecular spectrum, let us be quite optimistic about the final result.

5.5 Conclusion and Future Challenges

In conclusion, this experiment aimed to develop and characterize a polarization modulator for real-time states encoding in QKD experiments. Through the implementation of a PID controller, we were able to regulate the temperature of the modulator with relative fluctuations at regime of less than 10^{-4} , which is critical for achieving reliable and consistent results.

Initially, we used a CW laser and an arbitrary waveform generator to obtain three states encoding, resulting in a low QBER of 0.1 percent. Subsequently, we attempted to use a narrowband (100MHz FWHM) single photon source at cryogenic temperature, which resulted in a QBER of 2.3 percent. However, when we used a pulsed laser and a single photon source at room temperature, we encountered the challenge of PMD due to the birefringence of the material constituting the modulator.

In order to overcome this issue, we have employed a FRM-based and a Sagnac ring-based setup to compensate for PMD, resulting in significantly improved results. Our experiments using a pulsed laser with a 40 MHz repetition rate demonstrated a low QBER of 1.6 percent. Overall, this experiment was successful in developing and characterizing a polarization modulator for real-time states encoding in QKD experiments, demonstrating the importance

of precise temperature control and compensation strategies for achieving low QBER in case of broadband emission. Overall, our findings provide valuable insights into the development of practical and reliable quantum communication systems, and we believe that our work has contributed to the ongoing efforts to achieve secure and efficient quantum communication.

Chapter 6

Conclusions and Future Perspectives

Many quantum emitters have been extensively investigated till date, but important challenges remains open. Such challenges include ambient temperature operation as well as the portability of the quantum emitter within communication devices. In this thesis we have discussed the investigation of DBT:AC-based single photon sources for quantum photonics technologies, obtaining promising results. The presented SPS exhibits high levels of purity and interference ability, both of which are essential for the success of quantum technologies. In particular, the triggered generation of highly indistinguishable single photons from a single organic dye molecule under non-resonant pulsed excitation is achieved without the aid of any photonic resonance, resulting in a HOM interference visibility of over 78%, limited only by the residual dephasing present at the operating temperature of 3K. The remarkable spectral stability demonstrated in this experiment, where the HOM visibility remains largely unaffected even for photons separated by up to 125 ns, holds tremendous potential for the practical implementation of quantum technologies. Multiple photons are integral to the functioning of linear optical quantum computing, where the stable and predictable behavior of the HOM visibility observed in this experiment represents a significant step forward in the quest for reliable and efficient quantum computing. However, the brightness of the source at detector is currently limited to around 2%, which corresponds to a brightness at the first lens of around 5%. Therefore, the integration of the emitter with photonic devices becomes essential for implementation in quantum applications. Recent studies have demonstrated the potential of this type of system to be seamlessly integrated into hybrid photonic structures, where photonic resonance can modify both the radiation pattern and spectral distribution of the emission, thereby enhancing the source brightness to the state-of-the-art level.

Moreover, the successful implementation of a proof-of-concept QKD setup employing a deterministic single-photon source operating at room temperature is demonstrated in this study.

The use of a molecular emitter as a single-photon source has several advantages, including its room-temperature operation and long-term photostability, making it an attractive candidate for practical quantum communication applications. The experimental results indicate that the expected SKR_{mol} (0.5, Mbps at zero losses) of the molecular emitter is competitive with state-of-the-art experiments at cryogenic and room temperature. This performance can be further improved by optimizing the nano-photonics of the sample configuration and the optical setup, offering a promising avenue for future research. Furthermore, the analysis of the overall source efficiency suggests that the use of the generated single-photon states can offer potential advantages compared to the decoy state performances. The room-temperature operation and long-term photostability of the emitter make the proposed hybrid technology particularly interesting for satellite quantum communication.

Finally, we demonstrated real-time state preparation by means of a polarization modulator. Two alternative approaches, such as FRM and a Sagnac circuit, were applied to compensate for polarization mode dispersion arising in the lithium niobate crystal. In the case of WCP, the QBER is $\approx 1.6\%$ employing any of the compensation methods. We also used the SPS operated at 3k for real-time states encoding, demonstrating a QBER of $\approx 2.1\%$.

As a future work, with an ultra-compact and cost-effective QKD setup configuration, the technology could be integrated into next-generation satellite quantum-encrypted networks or used in a CubeSat for preliminary testing and experiments. Additionally, the system can be efficiently operated in fiber communication networks upon down-conversion to telecom wavelengths[229, 230].

The future upgrade to real-time state-preparation and -measurement has the potential to significantly enhance the performance and reliability of the proposed QKD setup. This would enable a continuous monitoring and optimization of the single-photon source, which is crucial for achieving high SKR_{mol} values and for detecting potential eavesdropping attacks. The integration of real-time state-preparation and -measurement with the emitter at low temperatures might enable the implementation of advanced quantum communication protocols, such as quantum teleportation and superdense coding, which have the potential to revolutionize the field of quantum communication.

References

- [1] David Kahn. *The codebreakers : the story of secret writing*. Macmillan, 1967.
- [2] Dong Ik Kim, Hyug-Gyo Rhee, Jae-Bong Song, and Yun-Woo Lee. Lives of the noble greeks and romans: Lysander, end i c. - beginning ii c, available on-line(<http://classics.mit.edu/plutarch/lysander.html>).
- [3] Polybius. The histories, book x, 45.6, ii c. b.c., available on-line(http://penelope.uchicago.edu/thayer/e/roman/texts/polybius/2*.html).
- [4] Dennis Luciano and Gordon Prichett. Cryptology: From caesar ciphers to public-key cryptosystems. *The College Mathematics Journal*, Vol, 18:2–17, 1987.
- [5] G. J. Caesar. Commentaries on the gallic war, book v, available on-line(<http://classics.mit.edu/caesar/gallic.5.5.html>).
- [6] Stefano Selleri. The roots of modern cryptography: Leon battista alberti's "de cifris". *URSI Radio Science Bulletin*, 2020(375):55–63, 2020.
- [7] G. S. Vernam. Cipher printing telegraph systems for secret wire and radio telegraphic communications. *Transactions of the American Institute of Electrical Engineers*, XLV:295–301, 1926.
- [8] N. Cawthorne. Alan turing, the enigma man. 2014, London, England.
- [9] Horst Feistel. Cryptography and computer privacy. *Scientific American*, 228(5):15–23, 1973.
- [10] S L Graham, R L Rivest, A Shamir, and L Adleman. Programming techniques a method for obtaining digital signatures and public-key cryptosystems. 1978.
- [11] Bernard Marr. The 4 biggest trends in big data and analytics right for 2021, Oct 2022.
- [12] Richard P. Feynman. Simulating physics with computers. *International Journal of Theoretical Physics*, 21(6/7):467–488, 1982.
- [13] Sonia López Bravo. Quantum computing history - azure quantum.
- [14] Frank Arute, Kunal Arya, Ryan Babbush, Dave Bacon, Joseph C Bardin, Rami Barends, Rupak Biswas, Sergio Boixo, Fernando GSL Brandao, David A Buell, et al. Quantum supremacy using a programmable superconducting processor. *Nature*, 574(7779):505–510, 2019.

- [15] Google AI Quantum. Google AI Quantum Laboratory. <https://ai.google/research/teams/applied-science/quantum/>.
- [16] IBM Q System One. <https://www.ibm.com/quantum-computing/system-one>.
- [17] Peter W Shor. Polynomial-time algorithms for prime factorization and discrete logarithms on a quantum computer *. *Society for Industrial and Applied Mathematics*, 41:303–332, 1999.
- [18] W K Wootters and W H Zurek. A single quantum cannot be cloned. *Nature*, 299:802–803–802–803, 10 1982.
- [19] Valerio Scarani, Helle Bechmann-Pasquinucci, Nicolas J. Cerf, Miloslav Dušek, Norbert Lütkenhaus, and Momtchil Peev. The security of practical quantum key distribution. *Reviews of Modern Physics*, 81:1301–1350, 2009.
- [20] C H Bennett and G Brassard. Quantum cryptography: Public key distribution and coin tossing. *Proceedings of IEEE International Conference on Computers, Systems, and Signal Processing, Bangalore, India (IEEE, New York)* pp. 175–179, 1984.
- [21] Norbert Lütkenhaus. Security against individual attacks for realistic quantum key distribution. *Phys. Rev. A*, 61:052304, Apr 2000.
- [22] Mark Oxborrow and Alastair G Sinclair. Single-photon sources. *Contemporary Physics*, 46(3):173–206, 2005.
- [23] D Gottesman H.-K. Lo N. Lütkenhaus and J Preskill. Security of quantum key distribution with imperfect devices. *Quantum Inf. Comput.* 5, 325, 2004.
- [24] H. Inamori, N. Lütkenhaus, and D. Mayers. Unconditional security of practical quantum key distribution. *The European Physical Journal D*, 41:599–627, 3 2007.
- [25] Joseph F Fitzsimons. Private quantum computation: an introduction to blind quantum computing and related protocols. *npj Quantum Information*, 3(1):23, 2017.
- [26] M. Mohseni, P. Read, H. Neven, et al. Commercialize quantum technologies in five years. *Nature*, 543(7644):171–174, 2017.
- [27] G. L. Roberts, M. Lucamarini, Z. L. Yuan, J. F. Dynes, A. J. Shields, R. V. Penty, K. Kalli, T. D. Bradley, T. N. H. Truong, J. R. Ong, et al. Experimental measurement-device-independent quantum digital signatures. *Nature communications*, 8(1):1–10, 2017.
- [28] Daniel A Vajner, Lucas Rickert, Timm Gao, Koray Kaymazlar, and Tobias Heindel. Quantum communication using semiconductor quantum dots. 2022.
- [29] Leonard Mandel. Quantum effects in one-photon and two-photon interference. *Reviews of Modern Physics*, 71(2):S274, 1999.
- [30] Xiongfeng Ma and Hoi-Kwong Lo. Quantum key distribution with triggering parametric down-conversion sources. *New Journal of Physics*, 10:073018, 7 2008.

- [31] Stephen Wiesner. 78 conjugate coding.
- [32] Hoi Kwong Lo, Xiongfeng Ma, and Kai Chen. Decoy state quantum key distribution. *Physical Review Letters*, 94, 6 2005.
- [33] Bernd Fröhlich, Marco Lucamarini, James F. Dynes, Lucian C. Comandar, Winci W.-S. Tam, Alan Plews, Andrew W. Sharpe, Zhiliang Yuan, and Andrew J. Shields. Long-distance quantum key distribution secure against coherent attacks. *Optica*, 4:163, 1 2017.
- [34] Sheng Kai Liao, Wen Qi Cai, Wei Yue Liu, Liang Zhang, Yang Li, Ji Gang Ren, Juan Yin, Qi Shen, Yuan Cao, Zheng Ping Li, Feng Zhi Li, Xia Wei Chen, Li Hua Sun, Jian Jun Jia, Jin Cai Wu, Xiao Jun Jiang, Jian Feng Wang, Yong Mei Huang, Qiang Wang, Yi Lin Zhou, Lei Deng, Tao Xi, Lu Ma, Tai Hu, Qiang Zhang, Yu Ao Chen, Nai Le Liu, Xiang Bin Wang, Zhen Cai Zhu, Chao Yang Lu, Rong Shu, Cheng Zhi Peng, Jian Yu Wang, and Jian Wei Pan. Satellite-to-ground quantum key distribution. *Nature*, 549:43–47, 9 2017.
- [35] Hoi-Kwong Lo, Xiongfeng Ma, and Kai Chen. Decoy state quantum key distribution. *Physical Review Letters*, 94(23):230504, 2005.
- [36] J. C. Loredó, M. A. Broome, P. Hilaire, O. Gazzano, I. Sagnes, A. Lemaitre, M. P. Almeida, P. Senellart, and A. G. White. Boson sampling with single-photon fock states from a bright solid-state source. *Phys. Rev. Lett.*, 118:130503, Mar 2017.
- [37] B Lounis and W E Moerner. Single photons on demand from a single molecule at room temperature. *NATURE*, 407, 2000.
- [38] Brahim Lounis and Michel Orrit. Single-photon sources. *Reports on Progress in Physics*, 68(5):1129, 2005.
- [39] Poompong Chaiwongkhot. Toward standardization of quantum key distribution. 2020.
- [40] Ghulam Murtaza, Maja Colautti, Michael Hilke, Pietro Lombardi, Francesco Cataliotti, Alessandro Zavatta, Davide Bacco, and Costanza Toninelli. Efficient room-temperature molecular single-photon sources for quantum key distribution. *Optics Express*, 12 2022.
- [41] Edo Waks, Charles Santori, and Yoshihisa Yamamoto. Security aspects of quantum key distribution with sub-poisson light. *Phys. Rev. A*, 66:042315, Oct 2002.
- [42] Kazuya Takemoto, Yoshihiro Nambu, Toshiyuki Miyazawa, Yoshiki Sakuma, Tsuyoshi Yamamoto, Shinichi Yorozu, and Yasuhiko Arakawa. Quantum key distribution over 120km using ultrahigh purity single-photon source and superconducting single-photon detectors. *Scientific Reports*, 5, 9 2015.
- [43] Timm Kupko, Martin von Helversen, Lucas Rickert, Jan Hindrik Schulze, André Strittmatter, Manuel Gschrey, Sven Rodt, Stephan Reitzenstein, and Tobias Heindel. Tools for the performance optimization of single-photon quantum key distribution. *npj Quantum Information*, 6, 12 2020.

- [44] Yasuhiko Arakawa and Mark J. Holmes. Progress in quantum-dot single photon sources for quantum information technologies: A broad spectrum overview. *Applied Physics Reviews*, 7(2):021309, 2020.
- [45] Christopher L. Morrison, Roberto G. Pousa, Francesco Graffitti, Zhe Xian Koong, Peter Barrow, Nick G. Stoltz, Dirk Bouwmeester, John Jeffers, Daniel K. L. Oi, Brian D. Gerardot, and Alessandro Fedrizzi. Single-emitter quantum key distribution over 175 km of fiber with optimised finite key rates. 9 2022.
- [46] P M Intallura, M B Ward, O Z Karimov, Z L Yuan, P See, P Atkinson, D A Ritchie, and A J Shields. Quantum communication using single photons from a semiconductor quantum dot emitting at a telecommunication wavelength. 2009.
- [47] Thomas Aichele, Gaël Reinaudi, and Oliver Benson. Separating cascaded photons from a single quantum dot:demonstration of multiplexed quantum cryptography. *Physical Review B*, 70:235329, 12 2004.
- [48] Markus Rau, Tobias Heindel, Sebastian Unsleber, Tristan Braun, Julian Fischer, Stefan Frick, Sebastian Nauwerth, Christian Schneider, Gwenaëlle Vest, Stephan Reitzenstein, Martin Kamp, Alfred Forchel, Sven Höfling, and Harald Weinfurter. Free space quantum key distribution over 500 meters using electrically driven quantum dot single-photon sources—a proof of principle experiment. *New Journal of Physics*, 16:043003, 4 2014.
- [49] R. J. Collins, P. J. Clarke, V. Fernández, K. J. Gordon, M. N. Makhonin, J. A. Timpson, A. Tahraoui, M. Hopkinson, A. M. Fox, M. S. Skolnick, and G. S. Buller. Quantum key distribution system in standard telecommunications fiber using a short wavelength single photon source. *Journal of Applied Physics*, 107, 4 2010.
- [50] Tobias Heindel, Christian A Kessler, Markus Rau, Christian Schneider, Martin F. Urst, Fabian Hargart, Wolfgang-Michael Schulz, Marcus Eichfelder, Robert Roßbach, Sebastian Nauwerth, Matthias Lermer, Henning Weier, Michael Jetter, Martin Kamp, Stephan Reitzenstein, Sven Höfling, Peter Michler, Harald Weinfurter, and Alfred Forchel. New journal of physics quantum key distribution using quantum dot single-photon emitting diodes in the red and near infrared spectral range. *New Journal of Physics*, 14:83001, 2012.
- [51] Peter Michler. *Quantum dots for quantum information technologies*, volume 237. Springer, 2017.
- [52] Timm Gao, Martin v. Helversen, Carlos Anton-Solanas, Christian Schneider, and Tobias Heindel. Atomically-thin single-photon sources for quantum communication. 4 2022.
- [53] Matthias Leifgen, Tim Schröder, Friedemann Gädeke, Robert Riemann, Valentin Métillon, Elke Neu, Christian Hepp, Carsten Arend, Christoph Becher, Kristian Lauritsen, and Oliver Benson. Evaluation of nitrogen- and silicon-vacancy defect centres as single photon sources in quantum key distribution. *New Journal of Physics*, 16, 2 2014.

- [54] Hao Zeng, Daniele Martella, Piotr Wasylczyk, Giacomo Cerretti, Jean-Christophe Gomez Lavocat, Chih-Hua Ho, Camilla Parmeggiani, and Diederik Sybolt Wiersma. High-resolution 3d direct laser writing for liquid-crystalline elastomer microstructures. *Adv. Mater.*, 26(15):2319–2322, 2014.
- [55] Çağlar Samaner, Serkan Paçal, Görkem Mutlu, Kıvanç Uyanık, and Serkan Ateş. Free-space quantum key distribution with single photons from defects in hexagonal boron nitride. 4 2022.
- [56] Jean-Baptiste Trebbia, Philippe Tamarat, and Brahim Lounis. Indistinguishable near-infrared single photons from an individual organic molecule. *Physical Review A*, 82:63803, 12 2010.
- [57] Pietro Lombardi, Marco Trapuzzano, Maja Colautti, Giancarlo Margheri, Ivo Pietro Degiovanni, Marco López, Stefan Kück, and Costanza Toninelli. A molecule-based single-photon source applied in quantum radiometry. *Advanced Quantum Technologies*, 3(2):1900083, 2020.
- [58] P. Lombardi, M. Colautti, R. Duquennoy, G. Murtaza, P. Majumder, and C. Toninelli. Triggered emission of indistinguishable photons from an organic dye molecule. *Applied Physics Letters*, 118, 2021.
- [59] Rocco Duquennoy, Maja Colautti, Ramin Emadi, Prosenjit Majumder, Pietro Lombardi, and Costanza Toninelli. Real-time two-photon interference from distinct molecules on the same chip. *Optica*, 9(7):731–737, 2022.
- [60] Sofia Pazzagli, Pietro Lombardi, Daniele Martella, Maja Colautti, Bruno Tiribilli, Francesco Saverio Cataliotti, and Costanza Toninelli. Self-assembled nanocrystals of polycyclic aromatic hydrocarbons show photostable single-photon emission. *ACS Nano*, 12(5):4295–4303, May 2018.
- [61] C. Toninelli, K. Early, J. Breimi, A. Renn, S. Götzinger, and V. Sandoghdar. Near-infrared single-photons from aligned molecules in ultrathin crystalline films at room temperature. *Optics Express*, 18:6577, 3 2010.
- [62] Charles Santori, David Fattal, Jelena Vučković, Glenn S. Solomon, and Yoshihisa Yamamoto. Indistinguishable photons from a single-photon device. *Nature*, 419(6907):594–597, 2002.
- [63] KF Reim, P Michelberger, KC Lee, J Nunn, NK Langford, and IA Walmsley. Single-photon-level quantum memory at room temperature. *Physical Review Letters*, 107(5):053603, 2011.
- [64] Daniel A. Vajner, Lucas Rickert, Timm Gao, Koray Kaymazlar, and Tobias Heindel. Quantum communication using semiconductor quantum dots. *arXiv:2108.13877*, 2021.
- [65] F. Troiani, A. Ghirri, M.G.A. Paris, C. Bonizzoni, and M. Affronte. Towards quantum sensing with molecular spins. *Journal of Magnetism and Magnetic Materials*, 491:165534, 2019.

- [66] Xueshi Guo, Casper R. Breum, Johannes Borregaard, Shuro Izumi, Mikkel V. Larsen, Tobias Gehring, Matthias Christandl, Jonas S. Neergaard-Nielsen, and Ulrik L. Andersen. Distributed quantum sensing in a continuous-variable entangled network. *Nature Physics*, 16(3):281–284, 2020.
- [67] D. M. Jackson, D. A. Gangloff, J. H. Bodey, L. Zaporski, C. Bachorz, E. Clarke, M. Hugues, C. Le Gall, and M. Atatüre. Quantum sensing of a coherent single spin excitation in a nuclear ensemble. *Nature Physics*, 17(5):585–590, 2021.
- [68] Jeremy L. O’Brien. Optical quantum computing. *Science*, 318(5856):1567–1570, 2007.
- [69] Jacques Carolan, Christopher Harrold, Chris Sparrow, Enrique Martín-López, Nicholas J. Russell, Joshua W. Silverstone, Peter J. Shadbolt, Nobuyuki Matsuda, Manabu Oguma, Mikitaka Itoh, Graham D. Marshall, Mark G. Thompson, Jonathan C. F. Matthews, Toshikazu Hashimoto, Jeremy L. O’Brien, and Anthony Laing. Universal linear optics. *Science*, 349(6249):711–716, 2015.
- [70] J. M. Arrazola, V. Bergholm, K. Brádler, T. R. Bromley, M. J. Collins, I. Dhand, A. Fumagalli, T. Gerrits, A. Goussev, L. G. Helt, J. Hundal, T. Isacsson, R. B. Israel, J. Izaac, S. Jahangiri, R. Janik, N. Killoran, S. P. Kumar, J. Lavoie, A. E. Lita, D. H. Mahler, M. Menotti, B. Morrison, S. W. Nam, L. Neuhaus, H. Y. Qi, N. Quesada, A. Repeatingon, K. K. Sabapathy, M. Schuld, D. Su, J. Swinerton, A. Száva, K. Tan, P. Tan, V. D. Vaidya, Z. Vernon, Z. Zabaneh, and Y. Zhang. Quantum circuits with many photons on a programmable nanophotonic chip. *Nature*, 591(7848):54–60, 2021.
- [71] Jonathan P Dowling and Gerard J Milburn. Quantum technology: the second quantum revolution. *Philosophical Transactions of the Royal Society of London. Series A: Mathematical, Physical and Engineering Sciences*, 361(1809):1655–1674, 2003.
- [72] Lars Jaeger. The second quantum revolution. *From Entanglement to Quantum Computing and Other Super-Technologies*. Copernicus, 2018.
- [73] Max Planck. On the theory of the energy distribution law of the normal spectrum. *Verh. Deut. Phys. Ges*, 2:237–245, 1900.
- [74] A. Einstein, B. Podolsky, and N. Rosen. Can quantum-mechanical description of physical reality be considered complete? *Phys. Rev.*, 47:777–780, May 1935.
- [75] Arthur H. Compton. A quantum theory of the scattering of x-rays by light elements. *Phys. Rev.*, 21:483–502, May 1923.
- [76] Gilbert N Lewis. The conservation of photons. *Nature*, 118(2981):874–875, 1926.
- [77] P. A. M. Dirac. The quantum theory of the emission and absorption of radiation. *Proceedings of the Royal Society of London. Series A*, 114(767):243–265, 1927.
- [78] R. HANBURY BROWN and R. Q. TWISS. A test of a new type of stellar interferometer on sirius. *Nature*, 178:1046–, November 1956.

- [79] C. W. Sandbo Chang, Carlos Sabín, P. Forn-Díaz, Fernando Quijandría, A. M. Vadiraj, I. Nsanzineza, G. Johansson, and C. M. Wilson. Observation of three-photon spontaneous parametric down-conversion in a superconducting parametric cavity. *Phys. Rev. X*, 10:011011, Jan 2020.
- [80] B. Lounis and M. Orrit. Single-photon sources. *Reports On Progress In Physics*, 68(5):1129–1179, 2005.
- [81] Claude Cohen-Tannoudji, Bernard Diu, and Franck Laloë. *Quantum mechanics, volume 3: fermions, bosons, photons, correlations, and entanglement*. John Wiley & Sons, 2019.
- [82] Satoshi Kako, Charles Santori, Katsuyuki Hoshino, Stephan Götzinger, Yoshihisa Yamamoto, and Yasuhiko Arakawa. A gallium nitride single-photon source operating at 200 k. *Nature materials*, 5(11):887–892, 2006.
- [83] V. Giesz, N. Somaschi, G. Hornecker, T. Grange, B. Reznichenko, L. De Santis, J. Demory, C. Gomez, I. Sagnes, A. Lemaitre, O. Krebs, N. D. Lanzillotti-Kimura, L. Lanco, A. Auffeves, and P. Senellart. Coherent manipulation of a solid-state artificial atom with few photons. *Nature Communications*, 7:11986–, June 2016.
- [84] M Hennrich, T Legero, A Kuhn, and G Rempe. Photon statistics of a non-stationary periodically driven single-photon source. *New Journal of Physics*, 6(1):86, jul 2004.
- [85] A. Gruber, A. Dräbenstedt, C. Tietz, L. Fleury, J. Wrachtrup, and C. von Borczyskowski. Scanning confocal optical microscopy and magnetic resonance on single defect centers. *Science*, 276(5321):2012–2014, 1997.
- [86] Christian Kurtsiefer, Sonja Mayer, Patrick Zarda, and Harald Weinfurter. Stable solid-state source of single photons. *Physical Review Letters*, 85:290–293–290–293, 7 2000.
- [87] Th. Basché, W. E. Moerner, M. Orrit, and H. Talon. Photon antibunching in the fluorescence of a single dye molecule trapped in a solid. *Physical Review Letters*, 69:1516–1519, 9 1992.
- [88] Sofia Pazzagli, Pietro Lombardi, Daniele Martella, Maja Colautti, Bruno Tiribilli, Francesco Saverio Cataliotti, and Costanza Toninelli. Self-assembled nanocrystals of polycyclic aromatic hydrocarbons show photostable single-photon emission. *ACS Nano*, 12:25, 2018.
- [89] Mohammad Musavinezhad, Dominik Rattenbacher, Alexey Shkarin, Jan Renger, Tobias Utikal, Stephan Götzinger, and Vahid Sandoghdar. Quantum efficiency of single dibenzoterrylene molecules in para-dichlorobenzene at cryogenic temperatures. *arXiv preprint arXiv:2303.12933*, 2023.
- [90] Christian Erker and Thomas Basche. The energy gap law at work: Emission yield and rate fluctuations of single nir emitters. *Journal of the American Chemical Society*, 144(31):14053–14056, 2022.
- [91] KH Drexhage. Influence of a dielectric interface on fluorescence decay time. *Journal of luminescence*, 1:693–701, 1970.

- [92] William E. Moerner and David P Fromm. Methods of single-molecule fluorescence spectroscopy and microscopy. *Review of Scientific Instruments*, 74(8):3597–3619, 2003.
- [93] Katiúscia N Casseiro, Kaisa Laiho, and Christine Silberhorn. Accessing the purity of a single photon by the width of the hong–ou–mandel interference. *New Journal of Physics*, 12(11):113052, 2010.
- [94] Philippe Grangier. Single photons stick together. *Nature*, 419(6907):577–577, 2002.
- [95] Mohammad Rezai, Jörg Wrachtrup, and Ilja Gerhardt. Coherence properties of molecular single photons for quantum networks. *Phys. Rev. X*, 8:031026, Jul 2018.
- [96] Chong-Ki Hong, Zhe-Yu Ou, and Leonard Mandel. Measurement of subpicosecond time intervals between two photons by interference. *Physical review letters*, 59(18):2044, 1987.
- [97] Hannes Bernien, Lilian Childress, Lucio Robledo, Matthew Markham, Daniel Twitchen, and Ronald Hanson. Two-photon quantum interference from separate nitrogen vacancy centers in diamond. *Phys. Rev. Lett.*, 108:043604, Jan 2012.
- [98] Ville Ahtee, Robert Lettow, Robert Pfab, Alois Renn, Erkki Ikonen, Stephan Götzinger, and Vahid Sandoghdar. Molecules as sources for indistinguishable single photons. *Journal of Modern Optics*, 56(2-3):161–166, 2009.
- [99] Marcus W Doherty, Neil B Manson, Paul Delaney, Fedor Jelezko, Joerg Wrachtrup, and Lloyd C L Hollenberg. The nitrogen-vacancy colour centre in diamond. *Physics Reports*, 528(1):1–45, 2013.
- [100] S Laurent, S Varoutsis, L Le Gratiet, A Lemaître, I Sagnes, F Raineri, A Levenson, I Robert-Philip, and I Abram. Indistinguishable single photons from a single-quantum dot in a two-dimensional photonic crystal cavity. *Applied Physics Letters*, 87(16):163107, 2005.
- [101] Natasha Tomm, Alisa Javadi, Nadia Olympia Antoniadis, Daniel Najer, Matthias Christian Löbl, Alexander Rolf Korsch, R??diger Schott, Sascha Ren?© Valentin, Andreas Dirk Wieck, Arne Ludwig, and Richard John Warburton. A bright and fast source of coherent single photons. *Nature Nanotechnology*, 16(4):399–403, 2021.
- [102] AJ Bennett, DC Unitt, AJ Shields, P Atkinson, and DA Ritchie. Influence of exciton dynamics on the interference of two photons from a microcavity single-photon source. *Optics express*, 13(20):7772–7778, 2005.
- [103] C. Toninelli, I. Gerhardt, A. S. Clark, A. Reserbat-Plantey, S. Götzinger, Z. Ristanovic, M. Colautti, P. Lombardi, K. D. Major, I. Deperasińska, W. H. Pernice, F. H. L. Koppens, B. Kozankiewicz, A. Gourdon, V. Sandoghdar, and M. Orrit. Single organic molecules for photonic quantum technologies. *Nature Materials*, 20:1615–1628, 2021.
- [104] The Bright Future Being Created by Diamonds - Orbray MAGAZINE - Orbray Co., Ltd., January 2023.

- [105] Gediminas Juska, Valeria Dimastrodonato, Lorenzo O Mereni, Agnieszka Gocalinska, and Emanuele Pelucchi. Towards quantum-dot arrays of entangled photon emitters. *Nature Photonics*, 7(7):527–531, 2013.
- [106] Dharmendra K Tiwari, Manisha Tiwari, and Takashi Jin. Near-infrared fluorescent protein and bioluminescence-based probes for high-resolution in vivo optical imaging. *Materials Advances*, 1(5):967–987, 2020.
- [107] Igor Aharonovich, Dirk Englund, and Milos Toth. Solid-state single-photon emitters. *Nat Photon*, 10(10):631–641, October 2016.
- [108] Julia Benedikter, Hanno Kaupp, Thomas Hümmer, Yuejiang Liang, Alexander Bommer, Christoph Becher, Anke Krueger, Jason M Smith, Theodor W Hänsch, and David Hunger. Cavity-enhanced single-photon source based on the silicon-vacancy center in diamond. *Physical Review Applied*, 7(2):024031, 2017.
- [109] Daniel Riedel, Immo Söllner, Brendan J Shields, Sebastian Starosielec, Patrick Appel, Elke Neu, Patrick Maletinsky, and Richard J Warburton. Deterministic enhancement of coherent photon generation from a nitrogen-vacancy center in ultrapure diamond. *Physical Review X*, 7(3):031040, 2017.
- [110] LJ Rogers, Kay D Jahnke, Mathias H Metsch, Jonas N Becker, Brett C Johnson, Kenichi Ohno, Patrick Maletinsky, Neil B Manson, and Liam P McGuinness. All-optical initialization, readout, and coherent preparation of single silicon-vacancy spins in diamond. *Physical Review Letters*, 113(26):263602, 2014.
- [111] Xing-ji Liu, Shang-da Li, Jing-yuan Zhang, Pei Wang, Xing-ji Zhang, Ya-nan Xie, Xiao-dong Xu, Wen-jiang Wu, and Lian-mao Duan. Coherent control of a single tin-vacancy center in diamond. *Physical Review Letters*, 122(6):063602, 2019.
- [112] B L Green, A Di Paola, and G D Fuchs. Generation of germanium-vacancy centers in diamond via electron irradiation and annealing. *Physical Review B*, 99(7):075442, 2019.
- [113] Peter Michler. *Single semiconductor quantum dots*, volume 28. Springer, 2009.
- [114] Dieter Bimberg, Marius Grundmann, and Nikolai N Ledentsov. *Quantum dot heterostructures*. John Wiley & Sons, 1999.
- [115] M. D. Eisaman, J. Fan, A. Migdall, and S. V. Polyakov. Invited review article: Single-photon sources and detectors. *Review of Scientific Instruments*, 82(7):071101–, July 2011.
- [116] D. Leonard, M. Krishnamurthy, C. M. Reaves, S. P. Denbaars, and P. M. Petroff. Direct formation of quantum-sized dots from uniform coherent islands of ingaas on gaas surfaces. *Applied Physics Letters*, 63(23):3203–3205, 1993.
- [117] X. Brokmann, E. Giacobino, M. Dahan, and J. P. Hermier. Highly efficient triggered emission of single photons by colloidal cdsezns nanocrystals. *Applied Physics Letters*, 85(5):712–714, 2004.

- [118] V. Zwiller, T. Aichele, W. Seifert, J. Persson, and O. Benson. Generating visible single photons on demand with single inp quantum dots. *Applied Physics Letters*, 82(10):1509–1511, 2003.
- [119] Zhiliang Yuan, Beata E Kardynal, R Mark Stevenson, Andrew J Shields, Charlene J Lobo, Ken Cooper, Neil S Beattie, David A Ritchie, and Michael Pepper. Electrically driven single-photon source. *science*, 295(5552):102–105, 2002.
- [120] F Basso Basset, F Salusti, L Schweickert, M B Rota, D Tedeschi, S F Covre da Silva, E Roccia, V Zwiller, K D Jöns, A Rastelli, and R Trotta. Article quantum teleportation with imperfect quantum dots.
- [121] Fiber-pigtailing quantum-dot cavity-enhanced light emitting diodes. 2021.
- [122] M. Orrit, J. Bernard, R. Brown, and B. Lounis. II Optical Spectroscopy of Single Molecules in Solids. volume 35 of *Prog. Opt.*, pages 61–144. Elsevier, 1996.
- [123] S. C. Kitson, W. L. Barnes, and J. R. Sambles. Photoluminescence from dye molecules on silver gratings. *Opt. Commun.*, 122(4-6):147–154, 1996.
- [124] Svetlana G Lukishova, Ansgar W Schmid, Andrew J McNamara, Robert W Boyd, and Carlos R Stroud. Room temperature single-photon source: single-dye molecule fluorescence in liquid crystal host. *IEEE Journal of selected topics in quantum electronics*, 9(6):1512–1518, 2003.
- [125] Lukas Novotny and Bert Hecht. *Principles of nano-optics*. Cambridge university press, 2012.
- [126] Sofia Pazzagli. *Organic nanocrystals and polymeric waveguides: a novel path towards integrated quantum nanophotonics*. PhD thesis, University of Florence, 2018.
- [127] Thomas Basché, WE Moerner, M Orrit, and UP (eds Wild. *Single-molecule optical detection, imaging and spectroscopy*. John Wiley & Sons, 2008.
- [128] Karl K Rebane and Inna Rebane. Peak value of the cross-section of zero-phonon line’s absorption. *Journal of luminescence*, 56(1-6):39–45, 1993.
- [129] Chloe Clear, Ross C. Schofield, Kyle D. Major, Jake Iles-Smith, Alex S. Clark, and Dara P. S. McCutcheon. Phonon-induced optical dephasing in single organic molecules. *Phys. Rev. Lett.*, 124:153602, Apr 2020.
- [130] AM Stoneham. Shapes of inhomogeneously broadened resonance lines in solids. *Reviews of Modern Physics*, 41(1):82, 1969.
- [131] Karl K Rebane. *Impurity Spectra of Solids: Elementary Theory of Vibrational Structure*. Springer Science & Business Media, 2012.
- [132] Douwe A Wiersma. Coherent optical transient studies of dephasing and relaxation in electronic transitions of large molecules in the condensed phase. *Advances in Chemical Physics: Photosensitive Chemistry. Part 2*, pages 421–485, 1981.

- [133] Helen Zhi Jie Zeng, Minh Anh Phan Ngyuen, Xiaoyu Ai, Adam Bennet, Alexander S. Solntsev, Arne Laucht, Ali Al-Juboori, Milos Toth, Richard P. Mildren, Robert Malaney, Igor Aharonovich, Igor Aharonovich, and Igor Aharonovich. Integrated room temperature single-photon source for quantum key distribution. *Optics Letters*, 47:1673, 4 2022.
- [134] Christopher J. Chunnillall, Ivo Pietro Degiovanni, Stefan Kuck, Ingmar M??ller, and Alastair G. Sinclair. Metrology of single-photon sources and detectors: a review. *Optical Engineering*, 53(8):081910–081910, 2014.
- [135] Uwe Jantzen, Andrea B Kurz, Daniel S Rudnicki, Clemens Schäfermeier, Kay D Jahnke, Ulrik L Andersen, Valery A Davydov, Viatcheslav N Agafonov, Alexander Kubanek, Lachlan J Rogers, and Fedor Jelezko. Nanodiamonds carrying silicon-vacancy quantum emitters with almost lifetime-limited linewidths. *New Journal of Physics*, 18(7):073036, 2016.
- [136] Momtchil Peev, Christoph Pacher, Romain Alléaume, Claudio Barreiro, Jan Bouda, W Boxleitner, Thierry Debuisschert, Eleni Diamanti, Mehrdad Dianati, JF Dynes, et al. The secoqc quantum key distribution network in vienna. *New Journal of Physics*, 11(7):075001, 2009.
- [137] Summit Supercomputer. <https://www.olcf.ornl.gov/summit/>.
- [138] Thomas Mertens and Stefan Schrauf. Quantum computing: An employee’s guide to the latest advances. <https://www.mckinsey.com/business-functions/mckinsey-digital/our-insights/quantum-computing-an-employees-guide-to-the-latest-advances>, 2020.
- [139] Claude E Shannon. A mathematical theory of communication. *The Bell System Technical Journal*, 27(3):379–423, 1948.
- [140] Robert H Dennard, Fritz H Gaensslen, Vaughan L Rideout, Ernest Bassous, and André R LeBlanc. Design of ion-implanted mosfet’s with very small physical dimensions. *IEEE Journal of Solid-State Circuits*, 9(5):256–268, 1974.
- [141] Dominic Mayers and Andrew Yao. Quantum cryptography with imperfect apparatus. In *Proceedings 39th Annual Symposium on Foundations of Computer Science (Cat. No. 98CB36280)*, pages 503–509. IEEE, 1998.
- [142] DGBJ Dieks. Communication by epr devices. *Physics Letters A*, 92(6):271–272, 1982.
- [143] Charles H. Bennett. Quantum cryptography using any two nonorthogonal states. *Physical Review Letters*, 68:3121–3124, 5 1992.
- [144] Dagmar Bruß and Gerd Leuchs. Lectures on quantum information. 2007.
- [145] Asher Peres and William K Wootters. Optimal detection of quantum information. *Physical Review Letters*, 66(9):1119, 1991.
- [146] Valerio Scarani, Helle Bechmann-Pasquinucci, Nicolas J Cerf, Miloslav Dušek, Norbert Lütkenhaus, and Momtchil Peev. The security of practical quantum key distribution. *Reviews of Modern Physics*, 81(3):1301, 2009.

- [147] Ulrik L Andersen, Tobias Gehring, Christoph Marquardt, Gerd Leuchs, and Radim Filip. Continuous variable quantum key distribution: current status and future challenges. *Laser Photonics Reviews*, 4(3):337–354, 2010.
- [148] Christian Weedbrook, Stefano Pirandola, Raul Garcia-Patron, Nicolas J Cerf, Timothy C Ralph, Jeffrey H Shapiro, and Seth Lloyd. Gaussian quantum information. *Reviews of Modern Physics*, 84(2):621–669, 2012.
- [149] Fr’ed’eric Grosshans and Philippe Grangier. Continuous variable quantum cryptography using coherent states. *Journal of Modern Optics*, 56(2):219–234, 2009.
- [150] G. Zhang, J. Y. Haw, H. Cai, F. Xu, S. M. Assad, J. F. Fitzsimons, X. Zhou, Y. Zhang, S. Yu, J. Wu, W. Ser, L. C. Kwek, and A. Q. Liu. An integrated silicon photonic chip platform for continuous-variable quantum key distribution, 12 2019.
- [151] Mingjian He, Robert Malaney, and Jonathan Green. Multimode cv-qkd with non-gaussian operations. *Quantum Engineering*, 2, 6 2020.
- [152] Dong Huang, Yongtao Liu, Xiaolong Zhang, Yijun Zhao, Bo Zhao, and Peng Guo. Free-space continuous-variable quantum key distribution over 1 km. *Optics Letters*, 45(3):708–711, 2020.
- [153] Xiaolong Zhang, Dong Huang, Yongtao Liu, Yijun Zhao, and Peng Guo. Experimental demonstration of continuous-variable quantum key distribution over free-space atmospheric channels. *IEEE Photonics Journal*, 12(4):1–9, 2020.
- [154] Davide Bacco, Luigi Cacciapuoti, Francesc Ciurana, LC Comandar, Jordi Diaz, and Fernando Dréau, Antoine Tand Soldevila. Free-space continuous-variable quantum key distribution with polarization encoding. *Physical Review A*, 102(5):052612, 2020.
- [155] Dong Huang, Xiaolong Zhang, Yongtao Liu, Yijun Zhao, and Peng Guo. Continuous-variable quantum key distribution over a turbulent free-space channel. *Optics Letters*, 46(10):2506–2509, 2021.
- [156] Artur K Ekert. Quantum cryptography based on bell’s theorem. *Physical Review Letters*, 67:661–663–661–663, 8 1991.
- [157] Nicolas Gisin, Grégoire Ribordy, Wolfgang Tittel, and Hugo Zbinden. Quantum cryptography. *Reviews of Modern Physics*, 74(1):145–195, 2002.
- [158] Stefano Pirandola et al. Advances in quantum cryptography. *Adv. Opt. Photonics*, 12(4):1012–1236, 2020.
- [159] Eleni Diamanti, Stefano Pironio, and Damien Querlioz. Detection of trojan horse attacks on quantum-key-distribution systems. *Physical Review A*, 73(2):022317, 2006.
- [160] Ilja Gerhardt, Qiang Liu, Antia Lamas-Linares, Johannes Skaar, Christian Kurtsiefer, and Vadim Makarov. Full-field implementation of a perfect eavesdropper on a quantum cryptography system. *Nature Communications*, 2(1):1–6, 2011.
- [161] Yi Zhao, Chi-Hang Fred Fung, Bing Qi, Christine Chen, and Hoi-Kwong Lo. Quantum hacking: Experimental demonstration of time-shift attack against practical quantum-key-distribution systems. *Physical Review A*, 78(4):042333, 2008.

- [162] Vadim Makarov. Controlling passively quenched single photon detectors by bright light. *New Journal of Physics*, 7(1):1–14, 2005.
- [163] Vadim Makarov, Andrey Anisimov, and Johannes Skaar. Effects of detector efficiency mismatch on security of quantum cryptosystems. *Physical Review A*, 77(1):012357, 2008.
- [164] Gilles Brassard, Norbert Lütkenhaus, Tal Mor, and Barry C. Sanders. Limitations on practical quantum cryptography. *Physical Review Letters*, 85:1330–1333, 8 2000.
- [165] Bruno Huttner, Nobuyuki Imoto, Nicolas Gisin, and Tsafirir Mor. Quantum cryptography with coherent states. *Physical Review A*, 51(3):1863, 1995.
- [166] Norbert Lütkenhaus and Mika Jahma. Quantum key distribution with realistic states: photon-number statistics in the photon-number splitting attack. *New Journal of Physics*, 4(1):44, 2002.
- [167] Teng-Yun Chen, Hao Liang, Yang Liu, Wen-Qi Cai, Lei Ju, Wei-Yue Liu, Jian Wang, Hao Yin, Kai Chen, Zeng-Bing Chen, et al. Field test of a practical secure communication network with decoy-state quantum cryptography. *Optics express*, 17(8):6540–6549, 2009.
- [168] Yi Zhao, Bing Qi, Xiongfeng Ma, Hoi-Kwong Lo, and Li Qian. Experimental quantum key distribution with decoy states. *Physical review letters*, 96(7):070502, 2006.
- [169] Yi Zhao, Bing Qi, Xiongfeng Ma, Hoi-Kwong Lo, and Li Qian. Experimental decoy state quantum key distribution over 15km. *arXiv preprint quant-ph/0503192*, 2008.
- [170] A Poppe, A Fedrizzi, R Ursin, HR Böhm, T Lorünser, O Maurhardt, M Peev, M Suda, Ch Kurtsiefer, H Weinfurter, et al. Practical quantum key distribution with polarization entangled photons. *Optics Express*, 12(16):3865–3871, 2004.
- [171] Danna Rosenberg, Jim W. Harrington, Patrick R. Rice, Philip A. Hiskett, Charles G. Peterson, Richard J. Hughes, Adriana E. Lita, Sae Woo Nam, and Jane E. Nordholt. Long-distance decoy-state quantum key distribution in optical fiber. *Phys. Rev. Lett.*, 98:010503, Jan 2007.
- [172] Marcos Curty, Xiongfeng Ma, Bing Qi, and Tobias Moroder. Passive decoy-state quantum key distribution with practical light sources. *Physical Review A - Atomic, Molecular, and Optical Physics*, 81, 2 2010.
- [173] Xiang-Bin Wang. Beating the photon-number-splitting attack in practical quantum cryptography. *Physical review letters*, 94(23):230503, 2005.
- [174] Won-Young Hwang. Quantum key distribution with high loss: Toward global secure communication, Aug 2003.
- [175] Sheng Kai Liao, Wen Qi Cai, Johannes Handsteiner, Bo Liu, Juan Yin, Liang Zhang, Dominik Rauch, Matthias Fink, Ji Gang Ren, Wei Yue Liu, Yang Li, Qi Shen, Yuan Cao, Feng Zhi Li, Jian Feng Wang, Yong Mei Huang, Lei Deng, Tao Xi, Lu Ma, Tai Hu, Li Li, Nai Le Liu, Franz Koidl, Peiyuan Wang, Yu Ao Chen, Xiang Bin Wang, Michael Steindorfer, Georg Kirchner, Chao Yang Lu, Rong Shu, Rupert Ursin,

- Thomas Scheidl, Cheng Zhi Peng, Jian Yu Wang, Anton Zeilinger, and Jian Wei Pan. Satellite-relayed intercontinental quantum network. *Physical Review Letters*, 120, 1 2018.
- [176] Xiongfeng Ma, Bing Qi, Yi Zhao, and Hoi-Kwong Lo. Practical decoy state for quantum key distribution. *Physical Review A*, 72(1):012326, 2005.
- [177] Stefania Castelletto. Silicon carbide single-photon sources: challenges and prospects. *Materials for Quantum Technology*, 1(2):023001, 2021.
- [178] Somaschi N., Giesz V., De Santis L., Loredano J. C., Almeida M.P., Hornecker G., Portalupi S. L., Grange T., Antón C., Demory J., Gómez C., Sagnes I., Lanzillotti-Kimura N.D., Lemaître A., Auffeves A., White A.G., Lanco L., and Senellart P. Near-optimal single-photon sources in the solid state. *Nat Photon*, 10(5):340–345, May 2016.
- [179] Elke Neu, David Steinmetz, Janine Riedrich-Möller, Stefan Gsell, Martin Fischer, Matthias Schreck, and Christoph Becher. Single photon emission from silicon-vacancy colour centres in chemical vapour deposition nano-diamonds on iridium. *New Journal of Physics*, 13(2):025012, 2011.
- [180] Chunlang Wang, Christian Kurtsiefer, Harald Weinfurter, and Bernd Burchard. Single photon emission from silicon centres in diamond produced by ion implantation. *Journal of Physics B: Atomic, Molecular and Optical Physics*, 39(1):37, 2005.
- [181] Matthew E Trusheim, Benjamin Pingault, Noel H Wan, Mustafa Gündoğan, Lorenzo De Santis, Kevin Chen, Mete Atatüre, and Dirk Englund. Quantum optics with tin-vacancy emitters in diamond. In *CLEO: QELS_Fundamental Science*, pages FM4A–1. Optica Publishing Group, 2019.
- [182] A Kiraz, M Ehrl, Th Hellerer, ÖE Müstecaplıoğlu, C Bräuchle, and A Zumbusch. Indistinguishable photons from a single molecule. *Physical review letters*, 94(22):223602, 2005.
- [183] C. Toninelli, I. Gerhardt, A. S. Clark, A. Reserbat-Plantey, S. Götzinger, Z. Ristanovic, M. Colautti, P. Lombardi, K. D. Major, I. Deperasińska, W. H. Pernice, F. H. L. Koppens, B. Kozankiewicz, A. Gourdon, V. Sandoghdar, and M. Orrit. Single organic molecules for photonic quantum technologies. *Nature Materials*, 20:1615–1628.
- [184] C. Toninelli, M. Huppert, A. Renn, S. Götzinger, and V. Sandoghdar. Coupling single molecules to microcavities. In *2011 Conference on Lasers and Electro-Optics Europe and 12th European Quantum Electronics Conference (CLEO EUROPE/EQEC)*, pages 1–1, 2011.
- [185] A. A. L. Nicolet, P. Bordat, C. Hofmann, M. A. Kol’chenko, B. Kozankiewicz, R. Brown, and M. Orrit. Single dibenzoterrylene molecules in an anthracene crystal: Main insertion sites. *Chemphyschem*, 8:1929–1936, 2007.
- [186] Jean-Baptiste Trebbia, Philippe Tamarat, and Brahim Lounis. Indistinguishable near-infrared single photons from an individual organic molecule. *Physical Review A*, 82(6):063803, 2010.

- [187] Pietro Lombardi, Maja Colautti, Rocco Duquennoy, Ghulam Murtaza, Prosenjit Majumder, and Costanza Toninelli. Indistinguishable photons from a single molecule under pulsed excitation. 255:06002, 2021.
- [188] Pietro Lombardi, Ramin Emadi, Rocco Duquennoy, Ghulam Murtaza, Maja Colautti, and Costanza Toninelli. Organic dye molecules as single photon sources for optical quantum technologies. pages Tu2B–3, 2021.
- [189] Hitoshi Kasai, Hari Singh Nalwa, Hidetoshi Oikawa, Shuji Okada, Hiro Matsuda, Nobutsugu Minami, Atsushi Kakuta, Katsumichi Ono, Akio Mukoh, and Hachiro Nakanishi. A Novel Preparation Method of Organic Microcrystals. *Japanese Journal of Applied Physics*, 31(Part 2, No. 8A):L1132–L1134, 1992.
- [190] R. B. Patel, A. J. Bennett, K. Cooper, P. Atkinson, C. A. Nicoll, D. A. Ritchie, and A. J. Shields. Postselective two-photon interference from a continuous nonclassical stream of photons emitted by a quantum dot. *Phys. Rev. Lett.*, 100:207405, May 2008.
- [191] Konstantin E Dorfman and Shaul Mukamel. Indistinguishability and correlations of photons generated by quantum emitters undergoing spectral diffusion. *Scientific Reports*, 4(1):1–6, 2014.
- [192] Dmitry N Makarov. Fluctuations in the detection of the hom effect. *Scientific Reports*, 10(1):20124, 2020.
- [193] H. Ollivier, S. E. Thomas, S. C. Wein, I. Maillette de Buy Wenniger, N. Coste, J. C. Loredó, N. Somaschi, A. Harouri, A. Lemaitre, I. Sagnes, L. Lanco, C. Simon, C. Anton, O. Krebs, and P. Senellart. Hong-ou-mandel interference with imperfect single photon sources, 2020.
- [194] H. Ollivier, S. E. Thomas, S. C. Wein, I. Maillette de Buy Wenniger, N. Coste, J. C. Loredó, N. Somaschi, A. Harouri, A. Lemaitre, I. Sagnes, L. Lanco, C. Simon, C. Anton, O. Krebs, and P. Senellart. Hong-ou-mandel interference with imperfect single photon sources. *Phys. Rev. Lett.*, 126:063602, Feb 2021.
- [195] John Preskill. Plug-in quantum software. *Nature*, 402(6760):357–358, 1999.
- [196] Wehner Stephanie, Elkouss David, and Hanson Ronald. Quantum internet: A vision for the road ahead. *Science*, 362(6412):eaam9288, October 2018.
- [197] Jiu-Peng Chen et al. Sending-or-not-sending with independent lasers: Secure twin-field quantum key distribution over 509 km. *Phys. Rev. Lett.*, 124(7):070501, 2020.
- [198] Alberto Boaron, Gianluca Boso, Davide Rusca, Cédric Vulliez, Claire Autebert, Misael Caloz, Matthieu Perrenoud, Gaëtan Gras, Félix Bussièrès, Ming-Jun Li, Daniel Nolan, Anthony Martin, and Hugo Zbinden. Secure quantum key distribution over 421 km of optical fiber. *Physical Review Letters*, 121:190502, 11 2018.
- [199] Yan Lin Tang, Hua Lei Yin, Qi Zhao, Hui Liu, Xiang Xiang Sun, Ming Qi Huang, Wei Jun Zhang, Si Jing Chen, Lu Zhang, Li Xing You, Zhen Wang, Yang Liu, Chao Yang Lu, Xiao Jiang, Xiongfeng Ma, Qiang Zhang, Teng Yun Chen, and Jian Wei Pan. Measurement-device-independent quantum key distribution over untrustful metropolitan network. *Physical Review X*, 6, 2016.

- [200] Nurul T Islam, Charles Ci, Wen Lim, Clinton Cahall, Jungsang Kim, and Daniel J Gauthier. P h y s i c s provably secure and high-rate quantum key distribution with time-bin qudits. 2017.
- [201] Davide Bacco, Beatrice Da Lio, Daniele Cozzolino, Francesco Da Ros, Xueshi Guo, Yunhong Ding, Yusuke Sasaki, Kazuhiko Aikawa, Shigehito Miki, Hirotaka Terai, Taro Yamashita, Jonas S Neergaard-Nielsen, Michael Galili, Karsten Rottwitt, Ulrik L Andersen, Toshio Morioka, and Leif K Oxenløwe. Boosting the secret key rate in a shared quantum and classical fibre communication system.
- [202] Bi-Xiao Wang et al. Long-distance transmission of quantum key distribution coexisting with classical optical communication over a weakly-coupled few-mode fiber. *Opt. Express*, 28(9):12558–12565, 2020.
- [203] Yan-Lin Tang, Hua-Lei Yin, Xiongfeng Ma, Chi-Hang Fred Fung, Yang Liu, Hai-Lin Yong, Teng-Yun Chen, Cheng-Zhi Peng, Zeng-Bing Chen, and Jian-Wei Pan. Source attack of decoy-state quantum key distribution using phase information. *Physical Review A*, 88:022308, 8 2013.
- [204] Poompong Chaiwongkhot, Sara Hosseini, Arash Ahmadi, Brendon L. Higgins, Dan Dalacu, Philip J. Poole, Robin L. Williams, Michael E. Reimer, and Thomas Jennewein. Enhancing secure key rates of satellite qkd using a quantum dot single-photon source. *arXiv:2009.11818*, 2020.
- [205] Matthias Leifgen, Tim Schröder, Friedemann Gädeke, Robert Riemann, Valentin Métyllon, Elke Neu, Christian Hepp, Carsten Arend, Christoph Becher, Kristian Lauritsen, and Oliver Benson. Evaluation of nitrogen- and silicon-vacancy defect centres as single photon sources in quantum key distribution. *New Journal of Physics*, 16(2):023021, feb 2014.
- [206] Mathieu Bozzio, Michal Vyvlečka, Michael Cosacchi, Cornelius Nawrath, Tim Seidelmann, Juan C. Loredó, Simone L. Portalupi, Vollrath M. Axt, Peter Michler, and Philip Walther. Enhancing quantum cryptography with quantum dot single-photon sources. *npj Quantum Information*, 8:104, 9 2022.
- [207] Helen Zhi Jie Zeng, Minh Anh Phan Ngyuen, Xiaoyu Ai, Adam Bennet, Alexander Solnsteve, Arne Laucht, Ali Al-Juboori, Milos Toth, Rich Mildren, Robert Malaney, et al. Integrated room temperature single photon source for quantum key distribution. *arXiv preprint arXiv:2201.11882*, 2022.
- [208] Daniel Llewellyn, Yunhong Ding, Imad I. Faruque, Stefano Paesani, Davide Bacco, Raffaele Santagati, Yan-Jun Qian, Yan Li, Yun-Feng Xiao, Marcus Huber, Mehul Malik, Gary F. Sinclair, Xiaoqi Zhou, Karsten Rottwitt, Jeremy L. O’Brien, John G. Rarity, Qihuang Gong, Leif K. Oxenlowe, Jianwei Wang, and Mark G. Thompson. Chip-to-chip quantum teleportation and multi-photon entanglement in silicon. *Nature Physics*, 16(2):148–153, Feb 2020.
- [209] E. Knill, R. Laflamme, and G. J. Milburn. A scheme for efficient quantum computation with linear optics. *Nature*, 409(6816):46–52, January 2001.

- [210] K.G. Lee, X.-W. Chen, H. Eghlidi, P. Kukura, R. Lettow, A. Renn, V. Sandoghdar, and S. Götzinger. A planar dielectric antenna for directional single-photon emission and near-unity collection efficiency. *Nat. Photon.*, 5(3):166–169, 2011.
- [211] Xiao-Liu Chu, Stephan Götzinger, and Vahid Sandoghdar. A single molecule as a high-fidelity photon gun for producing intensity-squeezed light. *Nat Photon*, 11(1):58–62, January 2017.
- [212] Pietro Lombardi, Marco Trapuzzano, Maja Colautti, Giancarlo Margheri, Ivo Pietro Degiovanni, Marco Lopez, Stefan Kock, and Costanza Toninelli. A molecule-based single-photon source applied in quantum radiometry. *Advanced Quantum Technologies*, 3(2):1900083, 2020.
- [213] Kazuya Takemoto, Yoshihiro Nambu, Toshiyuki Miyazawa, Yoshiki Sakuma, Tsuyoshi Yamamoto, Shinichi Yorozu, and Yasuhiko Arakawa. Quantum key distribution over 120 km using ultrahigh purity single-photon source and superconducting single-photon detectors. *Scientific Reports*, 5(1):14383, Sep 2015.
- [214] M. Colautti, D. Bacco, Rocco Duquennoy, R. Emadi, P. Majumder, P. Lombardi, G. Murtaza, M. Hilke, F. S. Cataliotti, A. Zavatta, and C. Toninelli. Hong-Ou-Mandel interference from distinct molecules on the same chip. 12446:1244611, 2023.
- [215] M Colautti, G Murtaza, M Hilke, P Lombardi, FS Cataliotti, A Zavatta, D Bacco, and C Toninelli. Organic molecules for quantum communication. pages SpW2J–1, 2022.
- [216] Simona Checcucci, Pietro Lombardi, Sahrish Rizvi, Fabrizio Sgrignuoli, Nico Gruhler, Frederik BC Dieleman, Francesco S Cataliotti, Wolfram HP Pernice, Mario Agio, and Costanza Toninelli. Beaming light from a quantum emitter with a planar optical antenna. *Light: Science & Applications*, 6(4):e16245, 4 2016.
- [217] C. Toninelli, K. Early, J. Breimi, A. Renn, S. Götzinger, and V. Sandoghdar. Near-infrared single-photons from aligned molecules in ultrathin crystalline films at room temperature. *Opt. Express*, 18(7):6577–6582, March 2010.
- [218] Daniele Cozzolino, Davide Bacco, Beatrice Da Lio, Kasper Ingerslev, Yunhong Ding, Kjeld Dalgaard, Poul Kristensen, Michael Galili, Karsten Rottwitt, Siddharth Ramachandran, and Leif Katsuo Oxenløwe. Orbital angular momentum states enabling fiber-based high-dimensional quantum communication. *Phys. Rev. Applied*, 11:064058, Jun 2019.
- [219] J. Bernard, L. Fleury, H. Talon, and M. Orrit. Photon bunching in the fluorescence from single molecules: A probe for intersystem crossing. *the Journal of Chemical Physics*, 98(2):850–859, 1993.
- [220] Aurelien A. L. Nicolet, Clemens Hofmann, Mikhail A. Kol’chenko, Boleslaw Kozankiewicz, and Michel Orrit. Single dibenzoterrylene molecules in an anthracene crystal: Spectroscopy and photophysics. *ChemPhysChem*, 8(8):1215–1220, 2007.
- [221] Kyle D. Major. Coupling single molecules to cryogenic optical fibre microcavities, 2 2016.

- [222] Ross C Schofield, Kyle D Major, Samuele Grandi, Sebastien Boissier, E A Hinds, and Alex S Clark. Efficient excitation of dye molecules for single photon generation. *Journal of Physics Communications*, 2:115027, 2018.
- [223] B. C. Buchler, T. Kalkbrenner, C. Hettich, and V. Sandoghdar. Measuring the quantum efficiency of the optical emission of single radiating dipoles using a scanning mirror. *Physical Review Letters*, 95:063003, 8 2005.
- [224] Beatrice Da Lio, Carlos Faurby, Xiaoyan Zhou, Ming Lai Chan, Ravitej Uppu, Henri Thyrrerstrup, Sven Scholz, Andreas D. Wieck, Arne Ludwig, Peter Lodahl, and Leonardo Midolo. A pure and indistinguishable single-photon source at telecommunication wavelength. *arXiv:2201.02465v1*, 2022.
- [225] Sebastian Zaske, Andreas Lenhard, Christian A. Keßler, Jan Kettler, Christian Hepp, Carsten Arend, Roland Albrecht, Wolfgang-Michael Schulz, Michael Jetter, Peter Michler, and Christoph Becher. Visible-to-telecom quantum frequency conversion of light from a single quantum emitter. *Phys. Rev. Lett.*, 109:147404, Oct 2012.
- [226] A. Duplinskiy, V. Ustimchik, A. Kanapin, V. Kurochkin, and Y. Kurochkin. Low loss qkd optical scheme for fast polarization encoding. *Optics Express*, 25:28886, 11 2017.
- [227] A. Gardelein, G. Anzolin, G. Molina-Terriza, J. P. Torres, M. Jofre, M. W. Mitchell, and V. Pruneri. 100 mhz amplitude and polarization modulated optical source for free-space quantum key distribution at 850 nm. *Journal of Lightwave Technology*, Vol. 28, Issue 17, pp. 2572-2578, 28:2572–2578, 9 2010.
- [228] I Lucio-Martinez, P Chan, X Mo, S Hosier, and W Tittel. Proof-of-concept of real-world quantum key distribution with quantum frames. *New Journal of Physics*, 11:095001, 9 2009.
- [229] Beatrice Da Lio, Carlos Faurby, Xiaoyan Zhou, Ming Lai Chan, Ravitej Uppu, Henri Thyrrerstrup, Sven Scholz, Andreas D Wieck, Arne Ludwig, Peter Lodahl, et al. A pure and indistinguishable single-photon source at telecommunication wavelength. *Advanced Quantum Technologies*, 5(5):2200006, 2022.
- [230] Mujtaba Zahidy, Mikkel T Mikkelsen, Ronny Müller, Beatrice Da Lio, Martin Krehbiel, Ying Wang, Michael Galili, Søren Forchhammer, Peter Lodahl, Leif K Oxenløwe, et al. Quantum key distribution using deterministic single-photon sources over a field-installed fibre link. *arXiv preprint arXiv:2301.09399*, 2023.